Sapienza University of Rome

Department of Physics
PhD in Accelerator Physics

Thesis For The Degree Of Doctor Of Philosophy

High-Brightness Beams for Advancing Light Sources

Thesis Advisor
Dr. Massimo Ferrario

Thesis Supervisor
Dr. Anna Giribono
Dr. Simone Di Mitri

Candidate
Giovanni Campri

Academic Year 2024-2025 (XXXVIII cycle)

Abstract

This thesis investigates the generation and preservation of high-brightness electron beams for advanced radiation sources, with applications ranging from compact inverse Compton facilities to large-scale free-electron lasers (FEL) and plasma-based accelerators. The work aims to identify and mitigate the main physical mechanisms that limit beam quality during acceleration and compression, combining analytical modeling, numerical simulations, and machine design studies.

The first part focuses on the BoCXS inverse Compton source, a proposal for a compact dual-interaction-point facility driven by a high-gradient C-band linac. Start-to-end simulations demonstrate the production of stable, low-emittance, and low-energy-spread beams, and introduce optics strategies to preserve brightness through the switchyard and into the interaction region, ensuring tunable X-ray emission in the 0.1–1 MeV range.

The second part addresses the microbunching instability in the context of FEL facilities, such as FERMI and EuPRAXIA@SPARC_LAB. Using a semi-analytical approach based on the Huang–Kim formalism, we study instability growth under different machine configurations and compression schemes, aiming at maximizing the beam quality required for FEL operation. In the end, we also present a theoretical outline of a laser heater, designed to ensure full compatibility with all EuPRAXIA@SPARC_LAB operation modes.

The results highlight the importance of a model-driven approach to accelerator design, while the methods and tools developed here provide a framework for optimizing brightness preservation across future light sources.

Contents

List of Figures

List of Tables

Chapter 1

Introduction

Accelerator-based light sources play a pivotal role in modern photon science, offering tunable, high-brilliance radiation across wavelengths from the infrared down to the hard X-ray regime. At their heart lies the principles of electrodynamics: a charged particle, wether subjected to a force (classical electrodynamics) or interacting with a field (quantum electrodynamics), radiates energy in the form of electromagnetic radiation. Such principle is exploited through a precise manipulation of relativistic electron beams in large-scale synchrotron facilities and Free-Electron Lasers (FELs) via undulators and wigglers, and in compact layouts via inverse Compton scattering (ICS) schemes. These magnetic and optical structures convert electron kinetic energy into coherent or partially coherent photon pulses, with performance quantified by the photon beam brilliance (or spectral brightness) [1], which encapsulates photon flux, phase-space density, and temporal structure:

$$\mathscr{B} = \frac{d^4 N_{ph}}{dA\, dt\, d\Omega\, d\lambda/\lambda} \tag{1.1}$$

where N_{ph} is the number of photons per unit of area A, per unit of solid angle Ω, per unit of time t and per unit of relative bandwidth. In practice, brilliance is reported in SI units of photons/s/mm^2/mrad^2/0.1%BW. Applications—from atomic-scale imaging to time-resolved spectroscopy—demand both high transverse coherence and narrow bandwidth, placing stringent requirements on the phase-space properties of the driving electron beam: emittance, energy spread, peak current, and temporal profile. In accelerator physics terms, the beam brightness of a charged particle beam (such as an electron beam) refers to the density of particles in six-dimensional phase space and can be expressed in terms of normalized emittances as [2, 3]

$$B_{6D} = \frac{2q}{\pi^2 \varepsilon_{nx} \varepsilon_{ny} \sigma_t \sigma_\delta}\,, \tag{1.2}$$

where q is the bunch charge, σ_t is the rms bunch duration, σ_δ is the relative energy spread and ε_n are the normalized emittances. On the electron side, preserving low emittance through injection, acceleration, and transport is critical—any growth due to collective effects (e.g. space-charge), or collective instabilities (e.g., microbunching) directly reduces photon brilliance. High brightness underpins photon science innovations, indeed, the brilliance of the X-ray beam one can generate is ultimately limited by the brightness of the electrons driving the source, motivating advanced accelerator designs and beam dynamics optimizations.

The impact of improved beam brightness over the past decades is illustrated by the astounding gains in X-ray source performance. Since the 1970s, synchrotron radiation facilities (the first generation of accelerator-based light sources) have boosted the brightness of X-ray beams by more than 22 orders of magnitude [4]. This dramatic improvement opened entirely new frontiers in research, enabling techniques like X-ray crystallography, spectroscopy and imaging with resolutions and sensitivities that were previously unachievable. These facilities feature storage rings with specialized magnet insertion devices (undulators and wigglers) to produce intense, highly collimated X-ray beams. They achieved source brilliance on the order of 10^{18-21} photons/(s mm^2 mrad^2 0.1%BW), enabling experiments from structural biology to materials science. The emphasis at third-generation sources was to minimize electron beam emittance and maximize stored current, however, even these large storage-ring sources have fundamental limits in achievable brightness–constrained by equilibrium emittance and energy spread in a ring, and by practical limits on ring size and magnetic field strength [5].

The advent of linac-driven X-ray FELs, often termed a “fourth-generation” (together with diffraction limited storage rings) light source [6], marked a paradigm shift. Based on Self-Amplified Spontaneous Emission (SASE), in an X-ray FEL, a high-brightness relativistic electron bunch is sent through a periodic magnetic undulator; the collective interaction of the electrons with the radiation they emit leads to microbunching and an exponential gain of coherent radiation intensity. The result is laser-like X-ray pulses with peak brilliance 10–12 orders of magnitude higher than those of the most advanced third-generation synchrotrons. For example, the Linac Coherent Light Source (LCLS) at SLAC demonstrated the first hard X-ray FEL lasing in 2009, producing Angstrom-wavelength X-ray pulses with peak brilliance of $\sim 10^{32}$ photons/(s mm^2 mrad^2 0.1%BW) [7]. Such FEL bursts are also extremely short (on the order of tens of femtoseconds or less), allowing researchers to capture ultrafast dynamics. Indeed their applications were immediately recognized [8], spanning from time-resolved pump-probe dynamics to structural biology and serial femtosecond crystallography [9–11]. The unprecedented brilliance of FEL beams stems directly from the extreme quality of the electron beams, hardly attainable in synchrotron facilities, and mostly made possible by the advent of the photocathode RF electron gun [12–14]. Following LCLS, several major FEL facilities have come online worldwide, including SACLA in Japan [15], the European XFEL in Germany [16], SwissFEL in Switzerland [17], and others, each pushing further the envelope of beam brightness and X-ray wavelength reach. Accelerator physicists continuously refine injector designs, compression schemes, and transport optics to push the brightness higher, as even small improvements can translate into significant increases in X-ray brilliance at the user endstations [18].

More in detail, the efficiency of the FEL emission is governed by the FEL parameter ρ_{fel} also known as Pierce parameter, which is dependent on the undulator parameters and on the electron beam brightness and energy [19]. The FEL parameter typically of the order of 10^{-3}–10^{-4}, defines the exponential growth of the emission, as it is inversely proportional to the gain length, and identifies the saturation power of the FEL process $P_{sat} \approx \rho_{\text{fel}} P_e$, whith P_e the electron beam power [20]. It also quantifies the FEL rms intrinsic relative bandwidth $\rho_{\text{fel}} \approx \Delta\lambda/\lambda$, setting the FEL parameter as an upper limit on the rms uncorrelated relative energy spread of the electron beam $\sigma_\delta < \rho_{\text{fel}}$ to avoid degradation of FEL brilliance. A limit on the geometric beam emittance to ensure spatial coherence is $\varepsilon_{x,y} \leq \lambda/(4\pi)$, where $\lambda/(4\pi)$ is the minimum phase space area for a diffraction limited photon beam [21]. Typical FEL linacs must deliver 0.2–1 nC bunch charge with peak currents in the kiloampere range and normalized emittances on the order of ~ 1 mm mrad, 0.05–0.1 % relative energy spread and 1–50 GeV final electron energy–parameters only achievable with state-of-the-art photoinjectors and accelerator technology [22, 23].

In parallel with, and complementary to large-scale FEL facilities, there has been growing interest in more compact accelerator-based X-ray sources, particularly those relying on ICS. These sources use the collision of a high-brightness electron beam with a high-power laser pulse to produce X-ray photons via relativistic Compton scattering [24, 25]. While much smaller in scale and brilliance than storage rings or FELs, ICS sources can still deliver highly useful X-ray beams. The X-rays from an ICS source are typically pulsed, quasi-monochromatic, tunable in energy, highly directional and possess high brilliance compared to conventional X-ray tubes [26], which are instead characterized by a broad photon spectral distribution and by a rather divergent emission. Due to the relativistic Doppler effect, the accessible photon energy reaches up to the MeV range (γ-ray regime), providing the possibility to probe the dynamics in nuclei [27, 28]. The Munich Compact Light Source (MuCLS), which is a commercial miniature storage-ring-based Compton source, provides a quasi-monochromatic X-ray beam with a brilliance of order 10^9 photons/(s mm^2 mrad^2 0.1%BW) at 25 keV [29], while some single-pass Compton source facilities as KEK-ATF have produced high-brilliance, photon pulse up to the γ-ray range [30]. In recent years, many dedicated user facilities based on this concept have been proposed and developed, e.g. the STAR facility in Italy [31], ThomX in France [32] and T-REX in the U.S. [33]. The appeal of inverse Compton sources lies in their compactness and cost-effectiveness: despite the lower absolute brilliance, these compact sources offer access to techniques like phase-contrast imaging, K-edge subtraction and small-angle scattering in ordinary lab or hospital settings that previously required a large facility [34–36]. Notably, achieving good performance from an ICS demands a tightly focused, high-power laser pulse, and a high-quality electron beam, as the total flux of radiated photons is linked to the beam emittance $\Phi \propto 1/\varepsilon$ while the spectral bandwidth of the radiation is proportional to the beam energy spread $\Delta\lambda/\lambda \propto \sigma_\delta$, implying that, the X-ray yield and spectral quality are strongly affected by the electron beam brightness.

Across all these accelerator-driven X-ray sources, from linac-based FELs, down to compact Compton setups, the brilliance of the X-ray source is a direct extension of the beam brightness of the accelerated electrons. The brightness upper limit of a linac-driven light source is fixed by the electron injector, and the rest of the accelerator can only seek to maintain that initial brightness. Once the electrons are accelerated to relativistic energy, the normalized emittance cannot be reduced–it can only stay constant (in absence of collective effects) or grow due to imperfections and nonlinear effects. The invention of the high-field RF photocathode gun was pivotal in this regard, where the beam brightness obtained scales with the accelerating field at the cathode and the beam charge density during emission. These in turn depend on the gun technology and the drive-laser parameters, which are tailored both transversely and longitudinally to optimize the initial beam distribution [37, 38]. The dominant brightness limitation in the injector are space-charge forces at low beam energy, which can significantly increase the emittance if not carefully managed. Several beam dynamics techniques are employed to mitigate space-charge-induced emittance growth in photoinjectors, implementing the key concept of emittance compensation [39, 40]. After the injector, the beam is accelerated in a linear accelerator to high energy (typically GeV-scale for FELs) and simultaneously longitudinally compressed to attain the high peak current (of hundreds of amperes or up to ∼kiloampere range) needed for strong FEL gain. Magnetic bunch compressors (e.g. chicane or dogleg sections) are used to shorten the bunch by imparting a path-length difference as a function of particle energy. This drastic compression, however, poses serious challenges as collective electromagnetic effects during compression can deteriorate the beam quality and hence reduce brightness. In particular, coherent synchrotron radiation (CSR) emitted when the bunch passes through compressor dipole magnets can induce energy perturbations and transverse kicks that increase the emittance and energy spread of the beam. Additionally, the compression process can trigger microbunching instability, whereby small initial density or energy modulations in the beam (e.g. from shot noise or cathode non-uniformity) are amplified through the combined action of longitudinal space-charge forces and CSR as the beam density increases, and manifest as fine-scale density and energy fluctuations along the bunch, which can increase the slice energy spread and undermine FEL performance [41–43]. To preserve beam brightness through compression, several mitigation strategies are employed. One crucial tool is the laser heater, an optical manipulation device that has become a standard component of modern high-brightness linacs [44]. The laser heater uses an infrared laser co-propagating with the electron bunch in a short undulator to introduce a small, controlled energy spread (few keV) into the beam prior to compression, harnessing longitudinal Landau damping to mitigate microbunching growth. The use of harmonic linearizer RF cavities is another standard practice: before entering a bunch compressor, the beam's longitudinal phase space (which initially has nonlinear curvature due to RF acceleration) is linearized by a higher-harmonic RF cavity to ensure the bunch compresses uniformly, minimizing effects that would exacerbate CSR and microbunching [45]. Finally, also advanced lattice and optical designs to suppress CSR effects have been proposed [46–49].

1.1 Motivations and scope

In this thesis, we build on these foundations to develop and evaluate strategies for maximizing electron beam brightness in both FEL and Compton X-ray source contexts. We do this by addressing two main topics: the beam dynamics design and feasibility of a Compton source with emphasis on brightness preservation and realistic tolerances; and the microbunching instability physics in FEL linacs, treated via semi-analytical models.

More in detail, my thesis work first focused on the optics design of the Bologna Compton X-ray Source, recently proposed as a compact light source for multidisciplinary applications [50]. Here, we present an update on the project, discussing its new features, such as the full-C-band accelerating structure and the new switchyard system which enables the use of multiple beamline simultaneously. We focus on the electron beam dynamics optimization that drove the design choices and we show the start to end simulation to complete the feasibility study of the machine. The main innovation here lies in demonstrating the preservation and maximization of six-dimensional beam brightness within a very compact, relatively low-energy beamline, despite the presence of an optically complex bunch selection module, which enables bunch-by-bunch routing of the electrons to different beamlines. This work involved a multifaceted challenge: namely the optimization and characterization of the RF photoinjector (where the space charge forces are the dominant effects on the beam quality), the minimization of quadrupole chromatic aberrations and CSR effects in the dogleg through the implementation of an harmonic linearizer RF cavity, and the careful optical tuning of the beam transport throughout the innovative beamline switchyard up to the interaction point with the laser photons. In the end, analytical calculations are used to estimate the radiation parameters of the Compton source.

The last part of the thesis work focused on the study of microbunching instability in the context of linac-based FELs. Two FEL facilities are here considered specifically: FERMI @Elettra Sincrotrone Trieste [51], an externally seeded FEL, and EuPRAXIA@SPARC_LAB [52], a plasma-driven SASE FEL currently in development at INFN-LNF. More in detail, we investigate the microbunching instability making use of a semi-analytical model to obtain an estimate of its impact on the electron beam quality. This model is the latest implementation of the Huang-Kim formalism for microbunching instability, featuring the novel introduction of intrabeam scattering effects [53]. Applying the model we develop optimal strategies of beam compression schemes in the context of high-current operations for FERMI, where the our experimental studies substantiate the agreement with theory and simulations, thereby enabling an informed extension of the same framework to EuPRAXIA@SPARC_LAB. For the latter, we performed an analysis of its specific machine configurations and working points to assess the susceptibility to microbunching-driven beam quality degradation. In the end, we discuss the theoretical outline of a laser heater for EuPRAXIA@SPARC_LAB, designed to provide the operational flexibility required to remain compatible with all the foreseen machine configurations.

Chapter 2

Electron beam dynamics in a linear accelerator

In this chapter, we give a brief review of the electron beam dynamics in linear accelerators, focusing on the topics relevant to this thesis work. Starting from the preliminary concepts to introduce the theoretical framework, we then discuss the beam dynamics following its evolution from the RF gun through the main components that make up a beamline.

2.1 Preliminary concepts

In the context of accelerators, whether circular or linear, the description of beam dynamics is based on definitions and approximations that simplify its analysis. This section presents the theoretical framework that underpins both the single-particle dynamics and the collective description of electron beams in a single-pass linac.

2.1.1 Single particle dynamics

To describe the state of a particle in the context of beam physics we first define a vector in the 6D phase space (x, p_x, y, p_y, z, p_z), where the x, y and z coordinates describe the horizontal, vertical and longitudinal position with respect to the reference particle respectively, while $p_{x,y,z}$ are the transverse and longitudinal momenta. This formalism allows to treat the transverse dynamics separately from the longitudinal one, while maintaining a complete description of the system. It is often convenient to introduce the pseudo-canonical coordinate (also called trace space), expressed as a function of the longitudinal trajectory coordinate s and relative to the reference particle momentum p_0, as $(x, x', y, y', z, \delta)$, where

$$\begin{cases} x' = \frac{dx}{ds} = \frac{p_x}{p_z} \\ y' = \frac{dx}{ds} = \frac{p_y}{p_z} \\ \delta = \frac{p_z - p_0}{p_0} \ . \end{cases} \tag{2.1}$$

Particles are rapidly accelerated to relativistic energy and move along the line undergoing horizontal and vertical oscillatory motion, guided by magnetic elements to keep the beam size under control. At these energies $p_z \gg p_{x,y}$ which implies that $x' \approx \theta_x$ and $y' \approx \theta_y$, as long as the amplitude of the oscillatory motion is much smaller than the respective wavelength. This assumption, known as the paraxial approximation, allows for the linearization of the equations of motion and the description of transverse dynamics analogously to geometric optics; hence the term "beam optics" is recurring in this context. In this way, the evolution of the 6D coordinates along the beamline can be expressed by a linear transfer matrix $R_{6\times6}$ which incorporates the effect of various beamline components such as drifts, quadrupoles, bending magnets, and RF cavities on the particle phase space coordinates. This general matrix framework is a fundamental tool in accelerator physics, allowing one to design and analyze the transport and manipulation of electron beams through complex accelerator systems. If the forces involved are linear and non-dissipative, the single particle motion is that of a linear oscillator with time-dependent frequency and amplitude. The orbits in phase space, thus, describe ellipses with area proportional to the action:

$$J = \frac{1}{2\pi} \int p_x dx \,, \tag{2.2}$$

which, in condition of adiabaticity, is an invariant of motion [54].

2.1.2 Emittance

In the ideal case, when considering the dynamics of an ensemble of particles, one can define the regime of the motion as laminar if the transverse velocity of all particles is uniquely determined by the displacement from the z axis of beam propagation and the dependence from this is linear [55]. This implies that the orbits of the various particles never intersect, and the phase space volume covered by the particles distribution is null.

In the regime of non-laminar beam, particles exhibit a random distribution of velocity, and focusing elements can influence only the average motion of particles. In this case, particles distribution occupies a finite volume in phase space, which is reasonable to describe with an ellipse if the system is linear. The Liouville theorem states that, if the system is Hamiltonian, the phase space density f is invariant [2]. The time evolution of f is given by:

$$\frac{df}{dt} = \frac{\partial f}{\partial t} + \sum_i \left(\dot{q}_i \frac{\partial f}{\partial q_i} + \dot{p}_i \frac{\partial f}{\partial p_i} \right) , \tag{2.3}$$

where q_i and p_i are the particles' coordinates and their conjugate momenta. If the forces are derivable from an Hamiltonian H

$$\dot{q}_i = \frac{\partial H}{\partial p_i} , \qquad \dot{p}_i = -\frac{\partial H}{\partial q_i} , \tag{2.4}$$

with a time-independent Hamiltonian, we obtain

$$\frac{df}{dt} = \frac{\partial f}{\partial t} + \sum_i \left(\frac{\partial H}{\partial p_i} \frac{\partial H}{\partial q_i} \frac{df}{dH} - \frac{\partial H}{\partial q_i} \frac{\partial H}{\partial p_i} \frac{df}{dH} \right) = \frac{\partial f}{\partial t} = 0 , \tag{2.5}$$

where the last equality holds if no particles are lost or created. If the aforementioned conditions are satisfied, the six-dimensional (x, p_x, y, p_y, z, p_z) phase space beam distribution may evolve by changing its shape, but its volume remains a conserved quantity. Moreover, this holds also for each of the three 2D projection of the 6D phase space, provided there are no coupling between the three orthogonal motions. The phase space area occupied by the particles distribution can be used as a measure of beam quality by introducing the concept of emittance. The general equation of an ellipse can be written as

$$Ax^2 + Bxy + Cy^2 = 1 , \tag{2.6}$$

and its area is given by

$$Area = \frac{2\pi}{\sqrt{4AC - B^2}} . \tag{2.7}$$

Then the emittance ellipse can be constructed as

$$\gamma_x x^2 + 2\alpha_x x x' + \beta_x x'^2 = \varepsilon_x , \tag{2.8}$$

where ε_x is the horizontal geometric emittance, usually expressed in mm mrad or μm (the same definition holds for the vertical plane (y, y')). By imposing the equality

$Area = \pi\varepsilon$ we have the relation

$$\gamma_x \beta_x - \alpha_x^2 = 1\,, \tag{2.9}$$

where $\gamma_x(s)$, $\beta_x(s)$ and $\alpha_x(s)$ are called Twiss parameters and are functions of the longitudinal coordinate s. From the geometrical relationship displayed in Fig. 2.1 one obtains

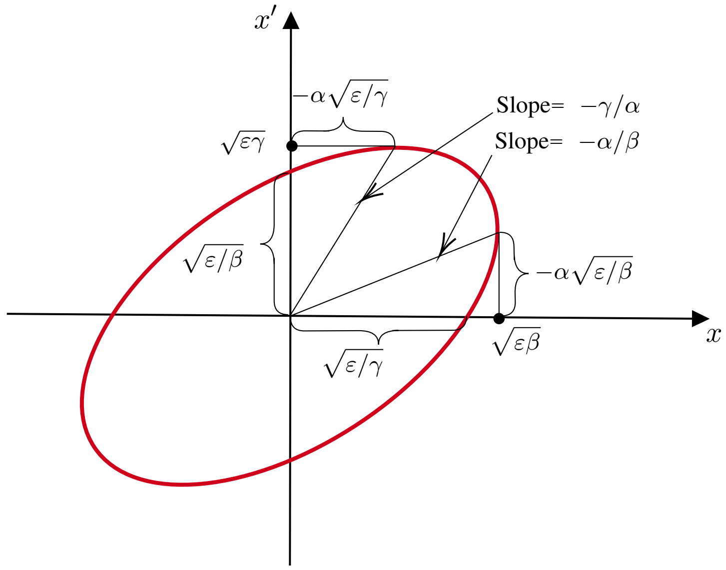

Figure 2.1: Elliptical boundary enclosing the particle distribution in phase space, displaying the relations between Twiss parameters and the ellipse geometry. Here, the subscripts x and y are omitted for the sake of brevity.

$$\alpha_x = -\frac{\beta_x'}{2}, \qquad \gamma_x = \frac{1+\alpha_x^2}{\beta_x}. \tag{2.10}$$

In reality, the condition of a perfectly laminar regime cannot be satisfied, and the system is never perfectly linear and non-dispersive, mainly because of non-linear Coulombian forces within the beam, aberration effects of the optical elements and the initial electron emission process at the cathode, resulting in a phase space particle distribution which can often differ from a regular ellipse. It is therefore useful to introduce a statistical definition of emittance, the so-called root mean square (rms) emittance, which represents the area of the equivalent-ellipse associated to the particle distribution, such that:

$$\begin{cases} \sigma_x = \sqrt{\varepsilon_{x_{rms}}\beta_x} \\ \sigma_{x'} = \sqrt{\varepsilon_{x_{rms}}\gamma_x} \\ \sigma_{xx'} = -\alpha_x\varepsilon_{x_{rms}} \end{cases} \tag{2.11}$$

where (removing the phase space centroid offset)

$$\begin{cases} \sigma_x^2 = \langle x^2 \rangle = \int_{-\infty}^{+\infty}\int_{-\infty}^{+\infty} x^2 f(x,x')dxdx' \\ \\ \sigma_{x'}^2 = \langle x'^2 \rangle = \int_{-\infty}^{+\infty}\int_{-\infty}^{+\infty} x'^2 f(x,x')dxdx' \\ \\ \sigma_{xx'} = \langle xx' \rangle = \int_{-\infty}^{+\infty}\int_{-\infty}^{+\infty} xx' f(x,x')dxdx' \end{cases} \tag{2.12}$$

are the second moments of the x and x' distributions and their respective correlation term. Substituting into Eq. 2.9 one finally obtains

$$\varepsilon_{x_{rms}} = \sqrt{\sigma_x^2\sigma_{x'}^2 - \sigma_{xx'}^2}\,, \tag{2.13}$$

which can be also expressed as the square root of the determinant of the beam matrix

$$\varepsilon_{x_{rms}} = \sqrt{\det\begin{pmatrix} \sigma_x^2 & \sigma_{xx'} \\ \sigma_{xx'} & \sigma_{x'}^2 \end{pmatrix}} \tag{2.14}$$

As a result of such statistical definition, the rms emittance does not represent a proper

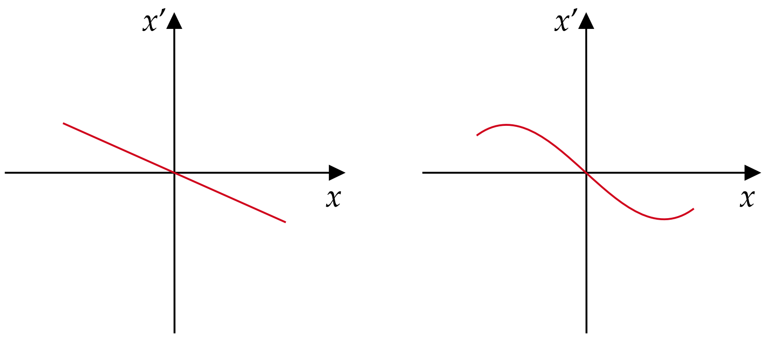

Figure 2.2: Idealized phase space particle distribution (left) is deformed and stretched (right) by means of nonlinear forces acting upon the beam.

Liouvillian quantity. As shown in Fig. 2.2, depicting an idealized particle distribution in phase space with $\varepsilon_{x_{rms}} = 0$, even if the net phase space surface occupied by a beam remains constant, non-linear field components can stretch and distort the shape of the phase space particle distribution. If we consider a generic correlation $x' = Ax^n$, by substituting in Eq. 2.13 one can easily see that $\varepsilon_{x_{rms}} \neq 0$ for $n \neq 1$. Hence, the rms emittance is not conserved if the system is nonlinear. This may happen even in the case of purely linear optics like quadrupoles: if the beam presents an energy spread σ_δ, different particles with different energy, although at the same transverse coordinate, will feel a different focusing force, thus evolving differently in the phase space (chromatic aberration). This will result in a beam quality degradation, which can be measured by its emittance increment as [56]

$$\Delta\varepsilon_{x_{rms}} = \varepsilon_{x_{rms}} \left(\sqrt{1 + K^2 \beta_x^2 \sigma_\delta^2} - 1 \right) , \tag{2.15}$$

where K is the integrated magnetic strength of the quadrupole. Moreover, when the beam is accelerated, neither the geometric emittance nor the rms emittance is conserved due to the definition of the pseudo-canonical coordinates. To recover the relativistic invariance one needs to use the proper canonically conjugate coordinates which define the so called normalized emittance as

$$\varepsilon_{nx_{rms}}^2 = \frac{1}{m^2 c^2} \left(\langle x^2 \rangle \langle p_x^2 \rangle - \langle x p_x \rangle^2 \right) , \tag{2.16}$$

where m is the rest mass of the particle, c is the speed of light and $p_x = m\beta c\gamma x'$ with $\beta = v_z/c$ and γ being the Lorentz factor. Considering the definition of the relative energy spread

$$\sigma_\delta = \frac{\langle \beta^2 \gamma^2 \rangle - \langle \beta\gamma \rangle^2}{\langle \beta\gamma \rangle^2} , \tag{2.17}$$

and assuming $\beta \approx 1$ and (x, x') independent of γ, one finds

$$\varepsilon_{nx_{rms}}^2 = \langle \gamma^2 \rangle (\sigma_\delta^2 \sigma_x^2 \sigma_{x'}^2 + \varepsilon_{x_{rms}}^2) . \tag{2.18}$$

In all of the cases of interest discussed here, $\sigma_\delta \ll 1$ and the first term in the round brackets is negligible, thus, we can approximate relation between geometric and normalized emittance, for both transverse planes, as

$$\varepsilon_{n_{rms}} = \langle\gamma\rangle\varepsilon_{rms} \,. \tag{2.19}$$

The normalized emittance results to be the more convenient and practical quantity to use as an indicator of the beam quality, as it is independent of the beam energy, although, in reality, the actual operational measurement is performed on the geometric emittance. From this point on, we drop the *rms* in the notation when talking about the emittance for the sake of brevity, since we will always refer to the rms emittance, unless stated otherwise.

2.1.3 Envelope equation

It is possible to describe the evolution of the beam envelope along its trajectory, during transport and acceleration, by deriving a differential equation using the moments of the beam distribution [57]. We start by computing the derivatives of σ_x [58]

$$\frac{d\sigma_x}{ds} = \frac{d}{ds}\sqrt{\langle x^2\rangle} = \frac{\sigma_{xx'}}{\sigma_x} \,, \tag{2.20}$$

$$\frac{d^2\sigma_x}{ds^2} = \frac{d}{ds}\frac{\sigma_{xx'}}{\sigma_x} = \frac{\sigma_{xx'}^2 + \langle xx''\rangle}{\sigma_x} - \frac{\sigma_{xx'}^2}{\sigma_x^3} \,. \tag{2.21}$$

Rearranging the latter equation and recalling the rms emittance definition we obtain the envelope equation

$$\sigma_x'' - \frac{\langle xx''\rangle}{\sigma_x} = \frac{\varepsilon_x^2}{\sigma_x^3} \,, \tag{2.22}$$

where the RHS term acts as a defocusing pressure-like term. Indeed, the emittance term is physically interpreted as an outward pressure on the beam envelope caused by the rms spread in trajectory angle, hence the term *emittance pressure* is often used. The term $\langle xx''\rangle$ physically represents the effects of transversal forces acting upon the beam, which under paraxial approximation ($p_x = px'$) can be written as:

$$\frac{dp_x}{dt} = \beta c\frac{d(px')}{ds} = F_x \,, \tag{2.23}$$

therefore the transverse acceleration is:

$$x'' = -\frac{p'}{p}x' + \frac{F_x}{\beta cp} \,. \tag{2.24}$$

We obtain that

$$\langle xx'' \rangle = -\frac{p'}{p}\sigma_{xx'} + \frac{\langle xF_x \rangle}{\beta cp}\,, \tag{2.25}$$

substituting in the envelope equation and recalling Eq. 2.20, we find

$$\sigma_x'' + \frac{p'}{p}\sigma_x' - \frac{\langle xF_x \rangle}{\sigma_x \beta cp} = \frac{\varepsilon_{nx}^2}{\gamma^2 \sigma_x^3}\,. \tag{2.26}$$

The acceleration of the beam acts here as an oscillating damping term proportional to p'/p, called *adiabatic damping.*

In the context of linear beam dynamics, the main external forces acting upon the beam are the forces necessary for the beam transport and focusing, typically exerted by elements such as solenoids and quadrupoles, but also Radio Frequency (RF) structures, acting on the beam with a ponderomotive focusing force [39]. In this case, the moment of the force is given by

$$\langle xF_x \rangle = \mp k \langle x^2 \rangle\,, \tag{2.27}$$

and by defining the wavenunmber as

$$k_{ext}^2 = \frac{k}{\gamma mc^2}\,, \tag{2.28}$$

we obtain for $\beta \approx 1$:

$$\frac{\langle xF_x \rangle}{\sigma_x cp} = \mp k_{ext}^2 \sigma_x\,. \tag{2.29}$$

The other highly relevant contributor to the transverse force acting on the beam is the one produced by the beam itself due to the internal Coulomb interactions. We can identify two regimes of such interactions in a multiparticle system depending on the scale in which they occur: the collisional regime is dominated by binary collision between close ranged particles, while in the space charge (SC) regime the self-field generated by the particles' distribution varies appreciably only over distances larger than the average separation of the single particles. In general, we can use smooth functions to describe the charge and field distributions, and we can treat the space charge force as an externally applied force, as long as the transverse beam size is large compared to the Debye length, defined as [2]

$$\lambda_D = \sqrt{\frac{\epsilon_0 \gamma^2 k_B T_b}{e^2 n}} \tag{2.30}$$

where ϵ_0 is the vacuum permittivity, k_B is the Boltzmann constant, T_b is the kinetic temperature (in the transverse direction), e is the unitary electric charge and n is the electron density. The linear component of the space charge acts as a defocusing force on the beam, while the non-linear components also cause rms emittance growth by distorting the phase space distribution. If correlations along the bunch are present, also linear components can induce an emittance growth, although reversible, as shown next. Let us consider a bunched beam characterized by a uniform charge distribution with a cylindrical symmetry and length L, carrying a current I and moving with a velocity $v_z = \beta c$, the linear component of the transverse space charge field is given by [59]

$$E_x = \frac{Ix}{8\pi\epsilon_0\sigma_x^2\beta c} g(\zeta, \gamma)\,, \tag{2.31}$$

where the field form factor $g(\zeta, \gamma)$ is described by the function

$$g(\zeta, \gamma) = \frac{1-\zeta}{2\sqrt{A^2 + (1-\zeta)^2}} + \frac{\zeta}{2\sqrt{A^2 + \zeta^2}}\,, \tag{2.32}$$

with $\zeta = z/L$ and $A = 2\sigma_x/(\gamma L)$. The moving charge distribution is also subjected to his own azimuthal magnetic field, thus the total transverse force is given by:

$$F_x = e(E_x - \beta c B_\theta) = e(1-\beta^2)E_x = \frac{eE_x}{\gamma^2}\,. \tag{2.33}$$

The momentum force term of the envelope equation can then be expressed as (for $\beta \approx 1$)

$$\frac{\langle xF_x \rangle}{\sigma_x cp} = \frac{eI\langle x^2 \rangle}{8\pi\epsilon_0\gamma^3 mc^3\sigma_x^3} = \frac{k_{sc}}{\gamma^3\sigma_x}\,, \tag{2.34}$$

where we introduced the beam perveance

$$k_{sc} = \frac{I}{2I_A} g(\zeta, \gamma) \tag{2.35}$$

with $I_A = 4\pi\epsilon_0 mc^3/e = 17$ kA being the Alfven current for the electrons. Putting all the pieces together, we can now express the complete envelope equation:

$$\sigma_x'' + \frac{\gamma'}{\gamma}\sigma_x' + k_{ext}^2\sigma_x = \frac{\varepsilon_{nx}^2}{\gamma^2\sigma_x^3} + \frac{k_{sc}}{\gamma^3\sigma_x}\,. \tag{2.36}$$

The two terms in the RHS of 2.36 describe the defocusing effects, identifying two regimes of beam propagation: the emittance dominated and the space charge dominated. When the space charge term is larger than the emittance term, the latter can be neglected in the equation and the linear component of the space charge force produces a quasi-laminar propagation of the beam, and transport and acceleration require a careful tuning of various machine elements to keep laminarity. Conversely when the emittance term is dominant, the particles' motion is predominantly random, with a collisionless hot gas-like behavior (thermal regime). A measure of the relative importance of the space charge force with respect to the emittance pressure is given by the laminarity parameter, defined as the ratio between the two terms

$$\rho = \frac{I\sigma_x^2}{2I_A\gamma\varepsilon_{nx}^2} . \tag{2.37}$$

When $\rho > 1$ the beam is in the space charge regime and behaves as a laminar flow. As the beam is accelerated, its energy grows and the regime shifts to the thermal one. The transition energy marks this change of regime, and is simply defined as the energy that gives $\rho = 1$

$$\gamma_{tr} = \frac{I\sigma_x^2}{2I_A\varepsilon_{nx}^2} . \tag{2.38}$$

Thus, in general, the space charge regime is typical of low-energy beams, however, energy is not the only discriminating factor. Even at high energy, space charge effects may recur if the bunch is strongly compressed, increasing its peak current, or if the spot size becomes large due to optic manipulation.

2.1.4 Emittance oscillation

The space charge defocusing term represents the Coulombian repulsion forces within the bunch, and in the ideal case of a cylindrical beam with uniform distribution it is linear. However, as shown in Eq. 2.31, the field introduces a longitudinal correlation within the bunch, through the dependency on the parameter ζ. Thus, in the space charge regime different longitudinal slices along the bunch are subjected to different forces and undergo different evolutions in the phase space. As shown in Fig. 2.3, such correlation results in variations of the projected rms emittance due to the misalignment of the various phase space slices, which can be evaluated by the formula [59]

$$\varepsilon_{x_{corr}} = \sqrt{\langle\sigma_{s_x}^2\rangle\langle\sigma_{s_{x'}}^2\rangle - \langle\sigma_{s_{xx'}}^2\rangle} , \tag{2.39}$$

where the brackets $\langle\ \rangle$ indicate the average and $\sigma_s(\zeta)$ refers to the envelope of the single longitudinal slice. The total normalized rms emittance is given by the projection, i.e.

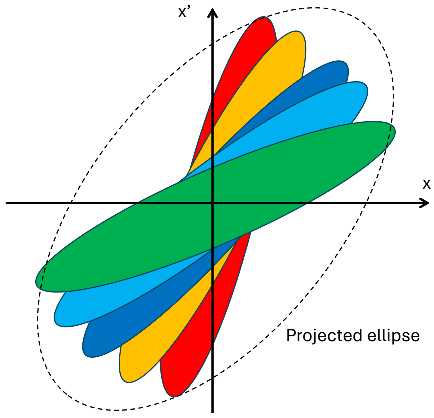

Figure 2.3: The misaligned longitudinal slices in transverse phase space cause an increment in the beam projected emittance.

superposition of the correlated and uncorrelated terms as

$$\varepsilon_{nx} = \langle\gamma\rangle\sqrt{\varepsilon_x^2 + \varepsilon_{xcorr}^2}\,. \tag{2.40}$$

It is possible to show that these emittance variations, related to correlations of transverse and longitudinal motion, are reversible. If we take as an example the case of a space charge dominated beam propagating in an external focusing channel, the envelope equation reduces to

$$\sigma_x'' + k_{ext}^2\sigma_x = \frac{k_{sc}}{\gamma^3\sigma_x}\,. \tag{2.41}$$

The solution to this equation is stationary and is given by

$$\sigma_{eq}(\zeta) = \frac{1}{k_{ext}}\sqrt{\frac{Ig(\zeta)}{2\gamma^3 I_A}}\,, \tag{2.42}$$

which is an equilibrium solution representing the matching conditions for which the external focusing force and the internal space charge force are perfectly balanced. This solution, however, is dependent on ζ, meaning that the equilibrium condition is different for each slice and usually cannot be achieved at the same time for all of the bunch slices. For a not perfectly matched slice, considering a small perturbation δ_0 with respect to its equilibrium condition, the solution is given by [39]

$$\sigma_s(\zeta) = \sigma_{eq}(\zeta) + \delta_0 \cos(\sqrt{2} k_{ext} s) \, , \tag{2.43}$$

which is an oscillating solution where the frequency is equal for all the slices (as in plasma oscillations). The corresponding projected emittance will be given by

$$\varepsilon_{corr} \sim |\sin(\sqrt{2} k_{ext} s)| \, , \tag{2.44}$$

showing the reversible nature of the correlated emittance growth, which periodically returns to zero. Indeed, the cause of the emittance growth, i.e. the coupling between transverse and longitudinal motion, also allows its reversibility. Figure 2.4 depicts the oscillatory behavior of mismatched slices and how the projected emittance reaches a minimum every half envelope oscillation period, indicating the realignment of the slices in phase space.

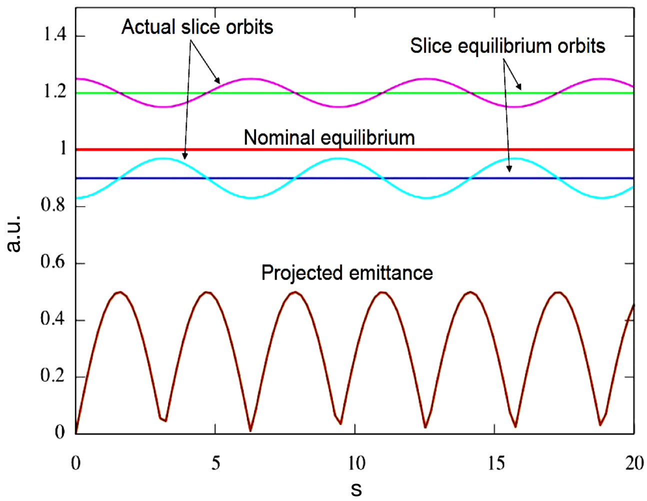

Figure 2.4: Slices and projected emittance oscillation of a space charge dominated beam along an external focusing channel [60].

Another relevant scenario is represented by the accelerating beam along a linac. In such case, the envelope equation includes the damping term and is given by

$$\sigma_x'' + \frac{\gamma'}{\gamma}\sigma_x' + k_{ext}^2 \sigma_x = \frac{\varepsilon_{nx}^2}{\gamma^2 \sigma_x^3} + \frac{k_{sc}}{\gamma^3 \sigma_x} \, , \tag{2.45}$$

which, for $\rho > 1$ yields the solution [61]

$$\sigma_{sc} = \sqrt{\frac{k_{sc}}{\gamma\left(\hat{k}^2 + \left(\frac{\gamma'}{2}\right)^2\right)}}\,, \tag{2.46}$$

where $\hat{k}^2 = k_{ext}^2\gamma^2$. This solution is not stationary, as $\sigma_x \propto 1/\sqrt{\gamma}$, thus the matched beam decreases its envelope as it accelerates. As a result, the correlated emittance oscillation is damped, as its amplitude is also proportional to $1/\sqrt{\gamma}$. For $\rho < 1$ we have [62]

$$\sigma_{\varepsilon} = \sqrt{\frac{\varepsilon_n}{\sqrt{\hat{k}^2 + \left(\frac{\gamma'}{2}\right)^2}}}\,. \tag{2.47}$$

In this case, the matched beam keeps its dimension constant along the accelerating process, and no correlated emittance oscillations are expected, since the interaction correlating the longitudinal and transverse motion is negligible. Therefore, around the energy of transition γ_{tr} the change in regime causes a behavioral shift and the equilibrium envelope stops shrinking, as schematically depicted in Fig.2.5.

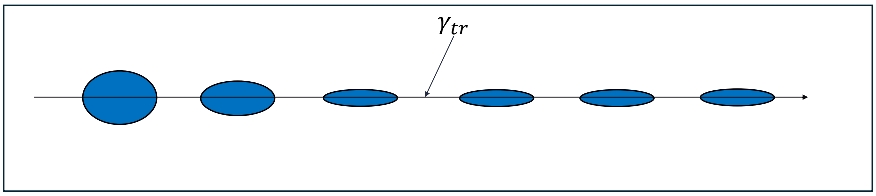

Figure 2.5: As the beam energy increases the equilibrium envelope shrinks and the the emittance oscillations are damped, up to γ_{tr}, where the beam changes regime and the envelope remains stationary.

2.2 Beam dynamics in a photoinjector

A more complete definition to express the electron beam quality is represented by the beam brightness which is given by [2, 3]

$$B_{6D} = \frac{2q}{\pi^2\varepsilon_{nx}\varepsilon_{ny}\sigma_t\sigma_\delta}\,, \tag{2.48}$$

measuring the overall charge density in the 6D phase space volume. Indeed, peak current control, low transverse emittance and low energy spread are qualities crucial for meeting the rigorous demands of various applications like free-electron lasers, Compton sources and high-energy linear colliders, making the beam brightness a true figure of merit. Before the 1990s, most high-current beams originated from thermionic or field-emission guns. In a thermionic gun, electrons are emitted off a heated cathode and are then accelerated; brightness was limited by large thermal emittances, energy spread at emission and by space charge blow-up at the gun exit. The real game changer for the electron beam quality in terms of brigthness was the invention of the photocathode gun in the late 80's [12–14]. By illuminating a material (e.g. copper, cesium telluride) with an ultrafast laser pulse timed to the RF crest, one extracts a beam with extremely low thermal (intrinsic) emittance [63]:

$$\varepsilon_{int} = \sigma_r \sqrt{\frac{\hbar\omega - \phi_{eff}}{3mc^2}}\,, \tag{2.49}$$

where σ_r is the laser spot size and $\hbar\omega - \phi_{eff}$ is the excess photon energy, being $\hbar$ the reduced Planck constant, ω the frequency of the photon and ϕ_{eff} the energy required for an electron to escape. Operating the gun RF cavity at high gradients (> 100 MV/m) shortens the drift distance over which space charge forces act, allowing to maintain a high beam current while preserving low emittance. Further advances in laser and RF cavity technology have made this type of injectors extremely reliable and stable, as they became the main standard for high brightness beam physics [64–66].

2.2.1 RF gun

A typical normal-conductive RF photoinjector gun uses a multi-cell copper standing wave cavity (most often 1.5–2.5 cells) resonant in the TM_{011} π-mode at frequencies typically around few GHz. The first half-cell contains the photocathode, where a laser-illuminated surface emits electrons directly into the high-gradient field. Downstream of the cathode cell are one or two full cells of identical length ($\approx \lambda/2$), which continue accelerating the beam to a few MeV over a physical length of few tens of cm. Coupling is provided through an on-axis or side-coupler waveguide port that feeds power into the first cell. Figure 2.6 depicts field lines in a 2.5-cell photocathode gun, showing the field inversion from one cell to the next, established by the resonant π-mode. This cavity mode is often used for accelerators since the change of polarity between cells allows the electron bunch to remain synchronous with the accelerating field. Often the first

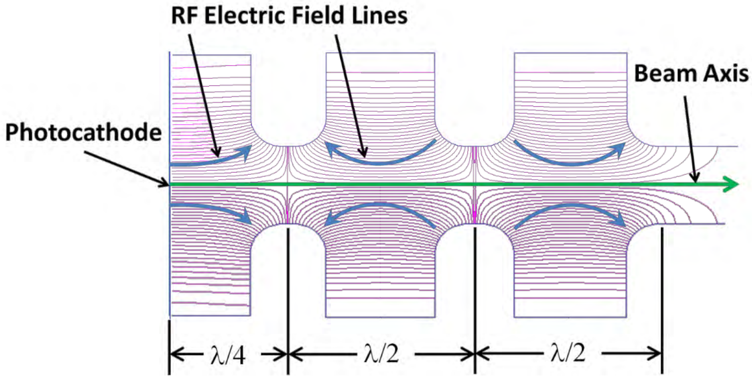

Figure 2.6: Sketch of a 2.5-cell RF gun. Image from *T, Rao and D, Dowell, An engineering guide to photoinjectors* [3].

half-cell is not exactly a 0.5 of the length, but rather a 0.6, as this design has showed to be preferable in terms of performance [67–69]. The non-zero field components of such RF gun are given by [70]:

$$E_z = E_0 J_0(j_{01} r) \cos(k_z s) \exp[i(\omega t + \phi_0)] \,, \tag{2.50}$$

$$E_r = \frac{-k_z}{j_{01}} E_0 J_0'(j_{01} r) \sin(k_z s) \exp[i(\omega t + \phi_0)] \,, \tag{2.51}$$

$$B_\theta = \frac{-ik_z}{j_{01} c} E_0 J_0'(j_{01} r) \cos(k_z s) \exp[i(\omega t + \phi_0)] \,, \tag{2.52}$$

where J_0 and j_{01} are the 0-order Bessel function and its first zero, ϕ_0 is the injection phase of the field, k_z is the longitudinal wave number and ω is the field frequency. These field components have huge effects on the electron beam, beyond simple acceleration. Here we summarize some of the most relevant ones, both for transverse and longitudinal beam dynamics.

The radial force component exerted by the RF field is given by

$$F_r = e(E_r - \beta c B_\theta) \,, \tag{2.53}$$

which becomes relevant at the irises. When the beam passes through an iris, going from a cell to the next, the subsequent anti-symmetric field components tends to cancel each other out, however this is not the case for the exit iris. Here, considering small values for the beam radius and $\beta \approx 1$, we can approximate the force as [3]

$$F_r = -eE_0 \frac{k_z r}{2} \cos(\omega t + \phi_0 - k_z s) \,, \tag{2.54}$$

The variation of momentum at the gun exit is

$$\Delta p_r = \int \frac{F_r}{c} ds = -\frac{eE_0}{2c} r \sin\phi_e \tag{2.55}$$

where ϕ_e is the field phase at the exit of the cavity. The angular kick is then given by

$$r' = \frac{\Delta p_r}{p} = -\frac{eE_0}{2mc^2\gamma} r \sin\phi_e \,, \tag{2.56}$$

which gives the focal length of the gun's RF lens

$$f_{RF} = -\frac{2mc^2\gamma}{eE_0 \sin\phi_e} \,. \tag{2.57}$$

Thus, the beam exiting the RF cavity is subjected to a defocusing force which is typically compensated by a solenoid placed around the gun exit. However different longitudinal slices arriving at slightly different exit phases will cause a spread in the angles which can be evaluated as

$$\sigma_{x'} = \frac{eE_0}{2mc^2\gamma} \cos\phi_e \sigma_x \sigma_\phi \,. \tag{2.58}$$

The beam emittance growth due to the RF fields can then be estimated, at the first order in ϕ, as

$$\varepsilon_{RF}^{(1)} = \frac{eE_0}{2mc^2} |\cos\phi_e| \sigma_x^2 \sigma_\phi \,, \tag{2.59}$$

while the second order describes the emittance growth due to field curvature and is given by [71]

$$\varepsilon_{RF}^{(2)} = \frac{eE_0}{2\sqrt{2}mc^2} |\sin\phi_e| \sigma_x^2 \sigma_\phi^2 \,. \tag{2.60}$$

To minimize the RF emittance it is usually preferable to exit from the gun with a phase $\phi_e = 90$ deg, although the second order emittance is maximized due to the RF curvature which is maximum on crest.

The beam energy variation given by the longitudinal component of the electric field is given by

$$mc^2 \frac{d\gamma}{ds} = -eE_z \,, \tag{2.61}$$

and by considering small beam dimensions, we can approximate it as

$$mc^2 \frac{d\gamma}{ds} = -eE_0 \cos(k_z s) \sin(k_z s + \phi) \,. \tag{2.62}$$

where $\phi = \omega t - k_z s + \phi_0$ is the relative phase of the electrons with respect to the synchronous RF phase. By using a trigonometric identity, it is possible to describe the accelerating field of the standing wave cavity as a sum of synchronous wave co-propagating with the beam plus a counter-propagating one:

$$\frac{d\gamma}{ds} = \alpha k_z [\sin\phi + \sin(\phi + 2k_z s)]\,, \tag{2.63}$$

where $\alpha = \frac{eE_0}{2mc^2 k_z}$ is a dimensionless parameter representing the strength of the accelerating field. A particle traveling at speed of light, thus synchronously with the forward wave phase, experiences a constant force from the forward wave and an oscillating force from the backward wave. Considering the initial part of acceleration (first half-cell), we can approximate the energy gain as [72]

$$\gamma(s) \approx 1 + 2\alpha k_z s \sin\phi\,. \tag{2.64}$$

The beam, generated at the cathode, slips through the field phase, while being accelerated. This phase slippage is given by

$$\phi - \phi_0 = \omega t - k_z s = k_z \int_0^s \left(\frac{\gamma}{\sqrt{\gamma^2 - 1}} - 1 \right) ds'\,. \tag{2.65}$$

The beam is rapidly accelerated to relativistic energy, becoming asymptotically synchronous to the field phase. The relationship between the injection and the exit phase can be found by combining the differential forms of Eq. 2.64 and 2.65:

$$k_z \left(\frac{\gamma}{\sqrt{\gamma^2 - 1}} - 1 \right) d\gamma = 2k_z \alpha \sin\phi \, d\phi\,, \tag{2.66}$$

which, with the initial condition $\gamma = 1$, $\phi = \phi_0$, gives

$$\cos\phi_e = \cos\phi_0 - \frac{1}{2\alpha}\,. \tag{2.67}$$

Finally, another important effect of the RF gun fields on the beam is the induced energy spread. The beam energy gained along a full cell of length l is obtained by integrating Eq. 2.63, which gives

$$\Delta E = \tilde{E} \sin\phi\,, \tag{2.68}$$

where $\tilde{E} = \frac{eE_0 l}{2}$. We now consider a normalized uniform particle distribution $\rho = \frac{1}{2\phi_m}$ for $-\phi_m < \phi < \phi_m$ and $\rho = 0$ elsewhere and we expand Eq. 2.68

$$\Delta E \approx \tilde{E}\bigg(\sin\phi + \cos\phi\Delta\phi - \frac{\sin\phi}{2}\Delta\phi^2 ... \bigg) \,. \tag{2.69}$$

The energy spread is then given by

$$\sigma_E = \bigg(\int_{-\phi_m}^{\phi_m} \rho(\Delta E - \mathbb{E}[\Delta E])^2 d\Delta\phi \bigg)^{1/2} , \tag{2.70}$$

which at the first order is

$$\sigma_E^{(1)} = \tilde{E}\cos\phi \frac{\phi_m}{\sqrt{3}} = \tilde{E}\cos\phi k_z \sigma_z \,, \tag{2.71}$$

knowing that for a uniform distribution $\phi_m = \sqrt{3}k_z\sigma_z$. The quadratic term is given by

$$\sigma_E^{(2)} = \frac{\tilde{E}}{\sqrt{5}} \sin\phi k_z^2 \sigma_z^2 \,. \tag{2.72}$$

As for the RF emittance, the RF-induced linear energy spread is minimum for on-crest operation, while the quadratic one is maximum.

2.2.2 Emittance compensation

At the exit of the RF gun, the last cavity acts as a defocusing lens, for both horizontal and vertical planes. As discussed in the previous paragraph, to minimize the RF emittance the beam has to be on-crest, thus maximizing the defocusing effects of the cavity. Moreover at this point the low energy beam (few MeV) is still in the space charge dominated regime and is subjected to large projected emittance growth due to misalignment of longitudinal slices in phase space. To counteract both of these effects, a solenoid is placed around the gun exit. The electrons entering the solenoid interact with the axially symmetric radial component of the magnetic field, present at the edges of the solenoid, which imprints on them an azimuthal velocity, proportional to the distance to the axis. The electrons then start rotating due to the longitudinal component of the magnetic field, as shown in Fig. 2.7. At the exit, the opposite radial field component cancels the azimuthal component of the velocity, leaving only the radial one, and the result is the effect of a focusing lens in both vertical and horizontal planes, differently from a

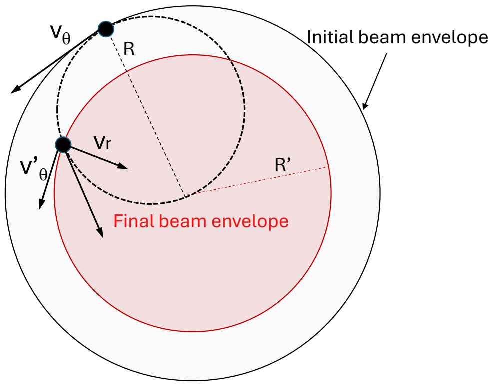

Figure 2.7: Electrons transverse motion inside a solenoid.

quadrupole. The focusing provided by the solenoid not only cancels the strong negative RF lens, but it also provides the restoring force needed to allow the realignment of the slices in phase space, in a process called emittance compensation [39]. However, the presence of a solenoid can introduce other effects that can degrade the emittance, as chromatic aberration and geometric aberration, which, together with further sources of emittance from the gun [73], will not be discussed here.

To counteract the strong RF defocusing, it is necessary to use a comparably strong focusing, with a focal length given by [74]

$$f_{sol} = \frac{1}{K\sin(KL_{sol})} \sim -f_{RF}\,, \quad \text{with } K = \frac{eB_0}{2p}\,, \tag{2.73}$$

where L_{sol} is the solenoid length. As sketched in Fig. 2.8, the solenoid effect makes all the beam slices converge, up until the point of full realignment. This defines the correct matching point to the subsequent accelerating cavity. For proper matching, however, also the condition of the beam envelope equilibrium, given by Eq. 2.46, has to be satisfied. Such condition implies the beam to be at waist, $\sigma'_{x,y} = 0$, which in theory should correspond to an emittance minimum. Chromatic effects of the solenoid, however, cause beatings between different slices oscillation frequencies, giving rise to double emittance minimum during its oscillation [75]. This phenomenon, shown in Fig. 2.9 is due to different slices with slightly different energy reaching waist at different positions. It is then possible to define the so called Ferrario working point, given by following conditions: beam at waist $\sigma'_{x,y} = 0$, beam envelop at equilibrium $\sigma_{x,y} = \sigma_{sc}$ and emittance at the local maximum. In this way, from that point the emittance decreases while the beam is accelerated, reaching the second minimum as the oscillations

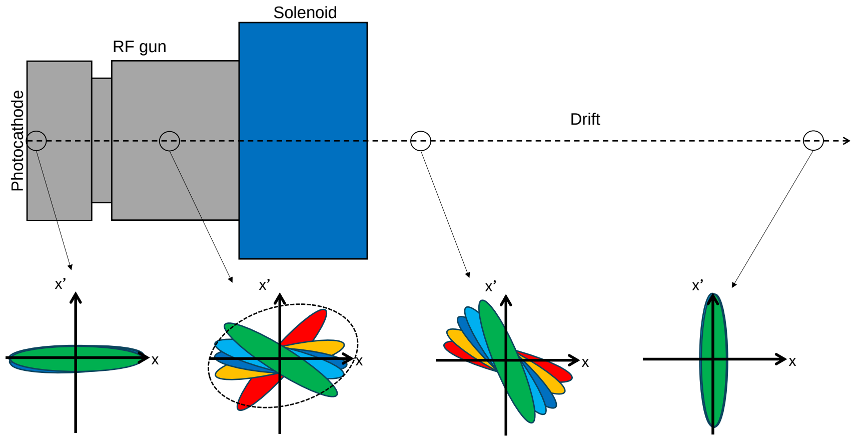

Figure 2.8: Sketch of the transverse phase space dynamics along the photoinjector. The slices are realigned by the focusing effect of the solenoid, in the process of emittance compensation. The magnetic strength of the solenoid defines the point of full realignment, corresponding to the injection to the subsequent accelerating channel.

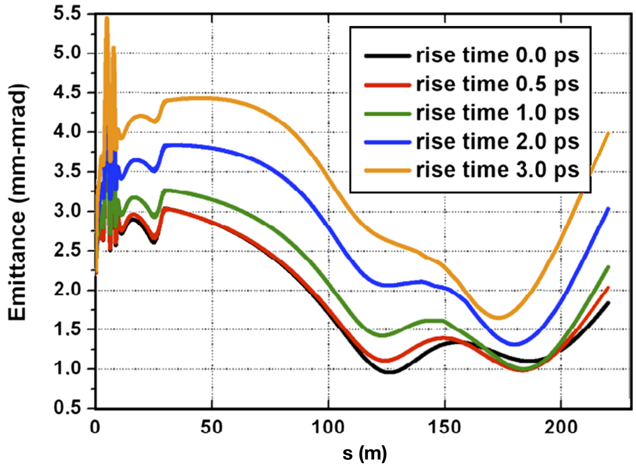

Figure 2.9: Double emittance minimum during rms emittance oscillations in the drift downstream the RF gun (PARMELA simulations) [75].

are damped, and freezing to that value in ultra-relativistic regime. An application of this technique can be seen in Section 3.2, where we discuss a photoinjector characterization.

2.2.3 Longitudinal phase space manipulation through RF accelerating cavity

Downstream the gun, electrons are usually accelerated in RF cavities operating in traveling-wave (TW) mode. A disk-loaded waveguide structure (periodic irises or discs in a waveguide) is used so that the RF phase velocity matches the electron beam's velocity. Indeed, in a plain cylindrical waveguide, an electromagnetic wave's phase velocity exceeds c, meaning an electron would slip behind the accelerating field. By periodically inserting disc irises into the waveguide, the dispersion relation of the accelerating mode is altered and the phase velocity can be reduced. The cell geometry is designed such that the fundamental TM_{01} accelerating mode has $v_{ph} \approx c$, allowing electrons to synchronize with the wave for continuous acceleration [70]. If the electrons energy is low, they slip through the electromagnetic wave phase until they accelerate enough to lock to a final phase ϕ_{fin}. The equation of motion of a particle in a TW structure is given by

$$mc\frac{d}{dt}(\gamma\beta) = e\hat{E}\sin\phi\,, \tag{2.74}$$

where $\hat{E}$ is the mean accelerating field. By integrating one obtains, assuming a $\beta_{fin} \approx 1$ [70]

$$\cos\phi_{fin} = \cos\phi_{in} + \frac{2\pi mc^2}{q\lambda_{RF}\hat{E}}\sqrt{\frac{1-\beta_{in}}{1+\beta_{in}}}\,, \tag{2.75}$$

which defines the limits of possible injection phases. Here β_{in} and ϕ_{in} are the injection velocity and phase. Early TW cavities in a photoinjector can also serve as a bunch compressor via velocity bunching [76]. This technique involves injecting the electron bunch on a phase ahead of the crest (i.e. slightly lower accelerating phase), so that the tail of the bunch sees a higher field than the head. The result is a correlated energy spread where trailing electrons gain more energy than leading ones. For a low energy beam, this translates to higher velocities for the tail, causing it to catch up with the head as they drift, thus compressing the bunch length. The variation of the bunch length can be expressed as [77]

$$\Delta\phi_{fin} = \Delta\phi_{in}\frac{\sin\phi_{in}}{\sin\phi_{fin}}\,. \tag{2.76}$$

Depending on the accelerating gradient, one can minimize the final bunch length by choosing an appropriate injection phase [78, 79], although in practice one must balance it with other considerations like emittance preservation and space charge effects.

The sinusoidal RF accelerating field of TW cavities introduces nonlinear energy–phase correlation in the beam longitudinal phase space, in the same way discussed for the RF gun. This can be detrimental for subsequent magnetic bunch length compression and in general can cause chromatic effects induced by the enlarged projected energy spread. To correct this, accelerators often employ higher-harmonic cavities as energy linearizers. These are RF cavities operating at a higher harmonic and set to a phase that introduces opposite curvature to the beam's energy-phase distribution. Let us consider the case of on-crest acceleration for simplicity: the energy gain of the beam inside the TW cavities operating at the fundamental harmonic can be expanded to the second order in z as:

$$E_0 \approx e\Delta V_0 \sin\phi + e\Delta V_0 k_z z \cos\phi - \frac{e\Delta V_0}{2} k_z^2 z^2 \sin\phi + o(z^3),$$

where ΔV_0 is the total effective voltage of the TW linac. Working on-crest ($\phi = \pi/2$), the first-order term in z should be negligible, while the second-order term can be canceled by using an additional RF cavity, operated at a higher frequency. Its energy contribution can be expressed as [80–82]:

$$E_f \approx E_0 + e\Delta V_H \sin\phi_H + e\Delta V_H k_H z \cos\phi_H - \frac{e\Delta V_H}{2} k_H^2 z^2 \sin\phi_H + o(z^3).$$

With a proper choice of the new RF phase ($\phi_H = 3\pi/2$), one can make the first-order term in z equal to zero and the second-order term positive. The new cavity is then decelerating the beam. The new RF voltage has now to satisfy the relationship:

$$\Delta V_H = \frac{k_z^2}{k_H^2} \Delta V_0 \, , \tag{2.77}$$

which allows the energy linearization and a net acceleration at the end of the whole RF structure as long as $k_H > k_z$. For the sake of efficiency one usually use the third harmonic in order to minimize the beam energy loss. Thus, by superimposing a higher-frequency accelerating voltage one can flatten the energy–time profile of the bunch. An application of this principle is discussed in Section 3.4.

2.3 Magnetic bunch length compression

Magnetic chicane compressors are essential in modern high-brightness electron linacs, especially for free-electron lasers and other applications requiring ultra-short, high-current bunches. A magnetic bunch compressor is a beamline section that shortens an electron bunch by inducing a path-length difference for particles of different energies. A common design is the symmetric four-dipole "C" chicane, as depicted in Fig. 2.10, which uses four dipole magnets arranged so that the beam's net deflection is zero. This symmetric C-shape chicane is achromatic, meaning it produces no overall transverse dispersion of the beam:

$$\eta_x \equiv \frac{\Delta x}{\delta} = 0\,, \quad \eta_x' \equiv \frac{\Delta x'}{\delta} = 0\,. \tag{2.78}$$

Such a chicane introduces a first-order longitudinal dispersion characterized by the

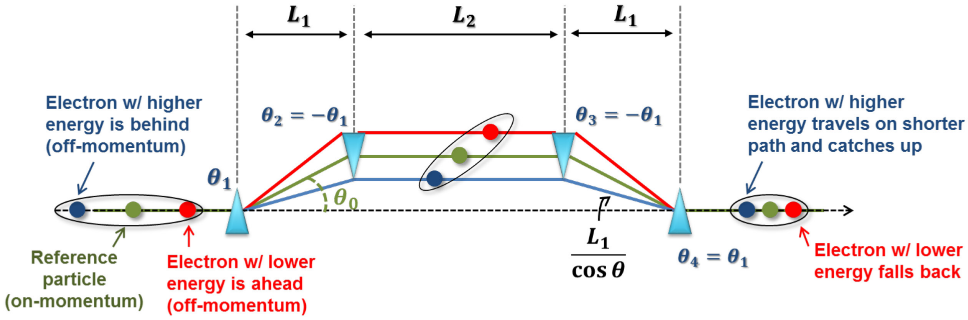

Figure 2.10: Schematic of a bunch length compression through a four-dipole symmetric magnetic chicane [80].

matrix element R_{56}, which relates a particle's path length difference (or longitudinal slippage Δz) to its relative momentum deviation as $R_{56} = \Delta z/\delta$. For ultra-relativistic beams, R_{56} is primarily determined by the chicane geometry (dipole bend angles and magnet spacing), and can be expressed as [80, 83]:

$$R_{56} \approx -2\theta^2 \left(L_1 + \frac{2}{3} l_d \right) \tag{2.79}$$

where θ is the nominal deflection angle, L_1 is the longitudinal distance between the external dipoles (see Fig. 2.10) and l_d is the magnets length. In a symmetric four-bend chicane, R_{56} is negative in the conventional orientation, indicating that higher-energy particles follow a shorter path through the chicane than lower-energy ones, thus such convention will be adopted throughout this thesis. At second order the nonlinear longitudinal particle motion is described by higher order momentum compaction T_{566} as $\Delta z = R_{56}\delta + T_{566}\delta^2$, and in a symmetric four-bend chicane usually $T_{566} \approx -1.5\, R_{56}$ [80]. To achieve compression, the beam must enter the chicane with a longitudinal energy chirp, i.e. a correlation between particle energy and position along the bunch. This is typically done by accelerating the beam off-crest, imparting a roughly linear energy-position tilt along the bunch. The linear chirp generated in the upstream cavities can be computed as

$$h \equiv \frac{1}{E}\frac{dE}{dz} \approx \frac{e\Delta V k_z \cos\phi}{E_i + e\Delta V \sin\phi}\,, \tag{2.80}$$

where E_i is the beam energy before the off-crest acceleration. A positive energy chirp is often defined such that the head of the bunch has lower energy than the tail. When the beam energy spread induced by the RF acceleration is much larger than the uncorrelated energy spread, the energy chirp can be estimated as $h \approx \sigma_\delta/\sigma_z$. In a linear approximation, one can quantify the degree of compression by a compression factor C, defined as the ratio of the initial bunch length to the final bunch length, which can be expressed as

$$C = \frac{1}{|1 + hR_{56}|}\,. \tag{2.81}$$

Maximum compression is achieved when $R_{56} = -1/h$. In this idealized full compression condition, the bunch length is minimized ($C \to \infty$ in the linear model). In practice, however, the minimum achievable length is limited by the bunch's initial uncorrelated energy spread $\sigma_{\delta u,i}$, converted to time spread by the chicane $\sigma_{z,min} = R_{56}\sigma_{\delta u,i}$, and by higher-order effects. In the case of $hR_{56} < -1$, the beam enters an over-compression regime where the head and tail swap order in energy-time phase space and the bunch starts lengthening again after the maximum compression point, as shown in Fig. 2.11. Assuming a total energy conservation (no frictional forces involved) the total energy

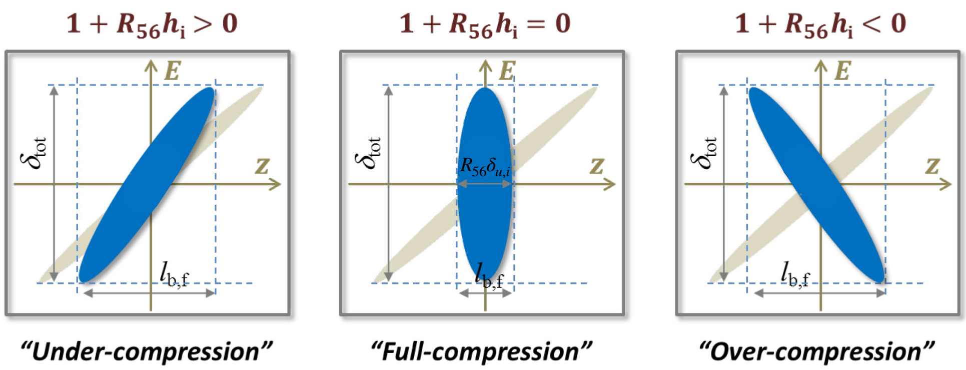

Figure 2.11: Sketch of beam longitudinal phase space before (grey shadow) and after (blue) a magnetic chicane, for the case of under-compression (left), full-compression (center) and over-compression (right). The bunch length for the full-compression case is limited by the initial uncorrelated energy spread transformed into time spread by the chicane. The total energy deviation remains constant during the process, in the absence of frictional forces (collective effects) [80].

deviation is conserved but the final uncorrelated energy spread is increased by the compression factor $\sigma_{\delta u,f} \approx C\sigma_{\delta u,i}$ (conservation of longitudinal emittance). Thus the chicane has the effect of "rotating" the longitudinal phase space, effectively translating particle's energy deviation to time deviation.

2.4 Collective effects

In the operation of high-brightness linear accelerators for X-ray light sources, collective interactions within the electron bunch play a decisive role in determining peak current, emittance preservation, and ultimately photon output. In this section, we focus on two phenomena that directly impact bunch quality during magnetic compression and transport: coherent synchrotron radiation (CSR)—the enhanced emission produced when a high density charge radiates coherently through dipoles—and the microbunching instability, wherein small initial energy or density perturbations are amplified by longitudinal dispersion and CSR feedback.

2.4.1 Coherent synchrotron radiation effects

In high-brightness beam physics, high charge beams with picosecond or sub-picosecond length are sensitive to CSR effects during bunch compression and beam transport through bending magnets. This can cause beam quality degradation through projected energy spread and emittance growth. CSR represents only the low-frequency component of the emitted synchrotron radiation (SR) but its emission is amplified with respect to the high frequency part because the electrons in the bunch occupy a length comparable to or smaller than its radiation wavelength. Under these conditions, the individual electrons' radiation fields add coherently—in phase—so that the total emitted intensity scales with the square of the number of electrons in the bunch [84]

$$P_C = NP_I = N^2 \frac{e^2 c\gamma^4}{6\pi\epsilon_0 R^2} \tag{2.82}$$

where P_C is the power of the fully coherent emission, P_I is the power of the fully incoherent one, R is the curvature radius and N is the total number of the electrons. A fully coherent emission can happen only for a bunch length l_b smaller than the characteristic SR wavelength $\lambda_{SR} \sim R/\gamma^3$, while for $\lambda_{SR} \lesssim l_b \lesssim \lambda_{SR} \cdot 10^7$ the emission is in a regime of partial coherence, where the power is energy independent [85]

$$P_{CSR} \approx \frac{0.028\, c\, e^2}{\epsilon_0 R^{2/3} \sigma_z^{4/3}} \,. \tag{2.83}$$

The beam curved path along dipoles allows radiation emitted by trailing particles in the bunch to catch up with leading particles within the bending magnet, as long as the slippage length over a circular arc $R\theta$ is $s_L \approx R\theta - 2R\sin\frac{\theta}{2} \geq l_b$. The main consequence of the tail–head CSR interaction is to induce a longitudinal momentum modulation along the bunch, with a characteristic correlation length on the order of the full bunch length, as shown in Fig. 2.12. When both leading and trailing particles

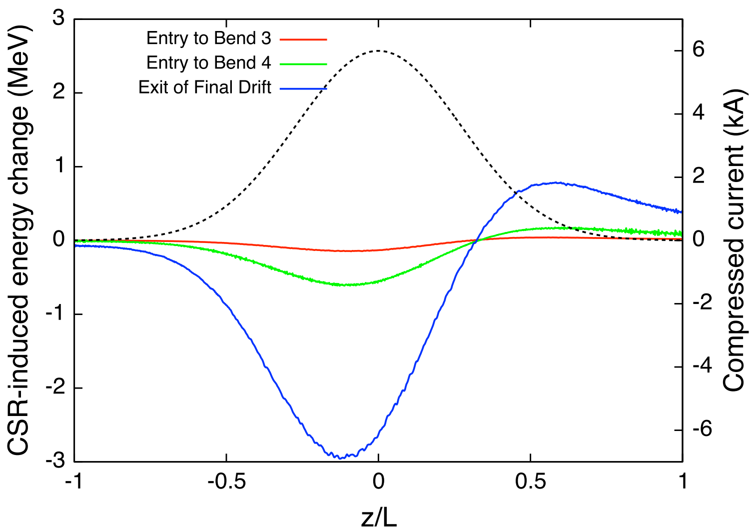

Figure 2.12: CSR-induced energy variation vs position along the bunch, for a Gaussian charge density passing through a 4-dipole magnetic chicane. The final compressed current profile is shown for reference (dashed line) [86]

are inside the magnet, this tail-head interaction can be described by a 1D steady-state model, which relies on the approximation that the ultra-relativistic electron distribution travels rigidly along the path, with a purely longitudinal CSR effect, directed ahead of the emitters, and neglecting the transverse position particles offset. Under these circumstances the rate of energy variation of an electron in a bunch with line charge density λ_z can be expressed as [84, 87, 88]

$$\frac{dE_e}{c\,dt} \approx -\frac{Ne^2}{24^{1/3}\pi\epsilon_0 R^{2/3}} \int_{z-s_L}^{z} \frac{d\lambda_z}{dz'} \frac{dz'}{(z-z')^{1/3}}\,, \tag{2.84}$$

where the dependence on $d\lambda_z/dz$ suggests that the energy loss can be enhanced by rapid variations of the current profile, e.g. current spikes and current modulations. An energy change δ_{CSR} of particles in a dispersive region causes a deviation from their design trajectory. This translates into a transverse offset and angular divergence of bunch slices, at the exit of the bending given by $\Delta x = \eta_x \, \delta_{CSR}$, $\Delta x' = \eta'_x \delta_{CSR}$. Hence, although the slice emittance is not affected, CSR effects can cause a projected emittance growth, given by

$$\varepsilon_x^2 = \varepsilon_{x,0}^2 + \varepsilon_{x,0} \mathscr{H}_x \sigma_{\delta,CSR} \, , \quad \text{with} \quad \mathscr{H}_x = \left[\eta_x^2 + (\beta_x \eta'_x + \alpha_x \eta_x)^2\right] / \beta_x \, , \tag{2.85}$$

where $\varepsilon_{x,0}$ is the initial projected emittance and $\mathscr{H}_x$ is the so-called chromatic H-function.

Various strategies can be adopted to suppress the CSR effects. For example one could use a longitudinal pulse shaping of the electron beam to flatten the energy variation along the bunch, thus minimizing the CSR-induced energy spread $\sigma_{\delta,CSR}$ [86]. Another option is to minimize the chromatic H-function in the region of the CSR kick. In a four-dipole magnetic bunch compressor, for example, most of the CSR effects are concentrated in the region of the fourth dipole, where the bunch is fully compressed and the H-function reduces to $\mathscr{H}_x \approx \eta_x'^2 \beta_x \approx \theta^2 \beta_x$, which implies that a small β_x function at the last chicane dipole can suppress the emittance growth [47]. Additionally, in most practical cases, not all spectral components of CSR are able to propagate in the chamber, and the overall radiating effects are smaller than in a free-space environment [89]. Therefore appropriate chamber geometry can have a shielding effect and suppress the CSR emission [90].

2.4.2 Microbunching instability

Microbunching instability (MBI) is a highly relevant phenomenon for high-brilliance light sources such as linac-driven free-electron lasers [42, 44, 84, 91]. Such an instability is a collective effect arising from small inhomogeneities in the beam longitudinal charge distribution, due to electron beam intrinsic shot noise or non-uniformity of the photo-injector laser pulse. Consequently, longitudinal space charge force and CSR effects in bunch compressors drive energy modulations in the longitudinal phase space. These are then transformed into amplified current modulations through non-isochronous dispersive sections ($R_{56} \neq 0$), and the phenomenon iterates itself establishing a positive feedback loop that enhances the instability. For FEL applications, the most detrimental consequence is the growth of slice energy spread on scales at or above the shortest modulation wavelength, which can severely affect gain and coherence. Indeed, microbunching gain is most pronounced for initial modulation wavelengths between 1 μm and 100 μm.

After applying bunch-compression factors of 10–100, these spatial scales map directly onto the characteristic lengths of UV and X-ray FEL operation.

Let us assume an electron beam in ultra relativistic regime, i.e. the longitudinal distribution is "frozen" in non-dispersive sections, and with transverse motion dominated by the emittance. Since MBI is often studied in the frequency domain, it is convenient to model the effects of near and far fields of the collective bunch interaction, respectively, as longitudinal space charge (LSC) and CSR impedance per unit length, in units of Ω/m. By averaging over a transverse round-disk uniform distribution of charges, whose area is πr_b^2, we can write the LSC impedance per unit length in free space as [92, 93]

$$Z_{LSC}(k) = \frac{iZ_0}{k\pi r_b^2}\left[1 - 2I_1\left(\frac{kr_b}{\gamma}\right)K_1\left(\frac{kr_b}{\gamma}\right)\right], \tag{2.86}$$

where $Z_0 = 376.73\ \Omega$ is the free space impedance, I_1, K_1 are modified Bessel functions, $k = 2\pi/\lambda$ is the modulation wave number and the effective radius $r_b = 0.8735(\sigma_x + \sigma_y)$ is introduced to match well-established 3D simulation results by space charge codes [93, 94]. Such formula remains valid as long as $kr_b/\gamma \not\gg 1$, as it tends to underestimate the effect of 3D fluctuations of the electric field [94]. In analogous way, we introduce the free-space 1D steady state impedance per unit length for the CSR in a dipole of curvature radius R [95, 96]

$$Z_{\rm CSR}(k) = (1.63 + i0.94)\frac{Z_0}{4\pi}\frac{k^{1/3}}{|R|^{2/3}}, \tag{2.87}$$

The imaginary nature of these impedances implies a redistribution of the particles' longitudinal momentum inside the bunch, without net energy loss.

To characterize the instability, we can refer to the spectrum of the 1D bunching factor, which is defined as the Fourier transform of the current modulation relative to the local smoothed average current I. If we assume the seed of the instability to be a broadband shot noise-like density modulation, where the fluctuations of number of electrons obey a Poisson statistics, the initial bunching factor is then given by [53]

$$|b_0(k)|^2 = \left|\frac{\sigma_I}{I_0}(k)\right|^2 = \left|\frac{1}{\Delta z_b}\int_{-\infty}^{+\infty}\frac{\Delta I(z)}{I_0}e^{-ikz}dz\right|^2 = \frac{1}{n_e} = \frac{ec}{I_0}\frac{k}{2\pi}, \tag{2.88}$$

where n_e is the expectation for the average number of electrons per modulation period, $\Delta z_b = c\Delta t_b$, I_0 is the initial value of the local smoothed average current, and $\Delta I(z)$ is the fluctuation around I_0. In the simplest case of a drift followed by a non-isochronous

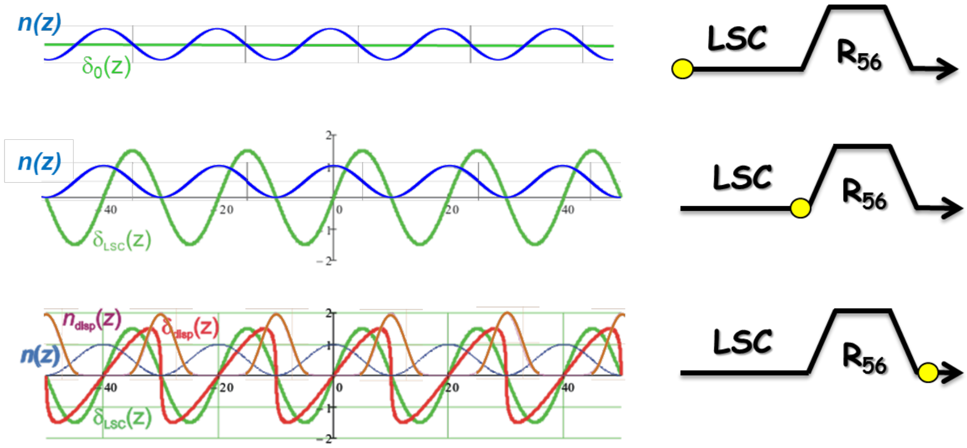

Figure 2.13: Evolution of density (n) and energy modulation (δ), driven by longitudinal space charge (LSC), along the bunch (left-hand diagrams), evaluated at different locations of a beamline made up of a straight section and non-isochronous dispersive section (right-hand side) [84].

dispersive section at constant energy, as depicted in Fig. 2.13 , the energy modulation amplitude induced by the collective effect is given by

$$\frac{\Delta\gamma}{\gamma}(k,s) = -\frac{4\pi I_0}{Z_0 I_A}\int_0^s b(k,s')\frac{Z_{\rm LSC}(k,s')}{\gamma(s')}\,ds', \tag{2.89}$$

where I_A is the Alfven current. These energy modulations are then transformed in amplified final bunching at the end of the dispersive section. We define the spectral gain of the microbunching instability as the ratio between the final bunching factor and the initial one, which in the approximation of a sinusoidal distortion of the energy distribution can be written as [97, 98]

$$\begin{aligned} G(k;s) = \left|\frac{b_f}{b_0}\right| &= \left|1 - \frac{2J_1\!\left(CkR_{56}\frac{\Delta\gamma}{\gamma}\right)}{b_0}\right| LD_\perp\, LD_\parallel \\ &\simeq \left|\frac{4\pi}{Z_0}\frac{I_0}{I_A}CkR_{56}\int_0^s \frac{Z_{\rm LSC}(k;s')}{\gamma(s')}\,\mathrm{d}s'\right| LD_\perp\, LD_\parallel \end{aligned} \tag{2.90}$$

where C is the linear compression factor, while $LD_\perp$ and $LD_\parallel$ are two damping terms. Indeed, within a beam having an uncorrelated relative energy spread σ_δ, particles belonging to the same bunch slice will travel through the dispersive section along different path lengths due to their energy difference, smearing the distribution and damping the instability, in a process called longitudinal Landau damping ($LD_{\|}$). As we will discuss in chapter 4, the use of devices such as a laser heater can be involved to artificially increase the energy spread and to enhance the damping mechanism [99, 100], as shown in Fig. 2.14. At the same time, particles belonging to the same bunch slice in a beam

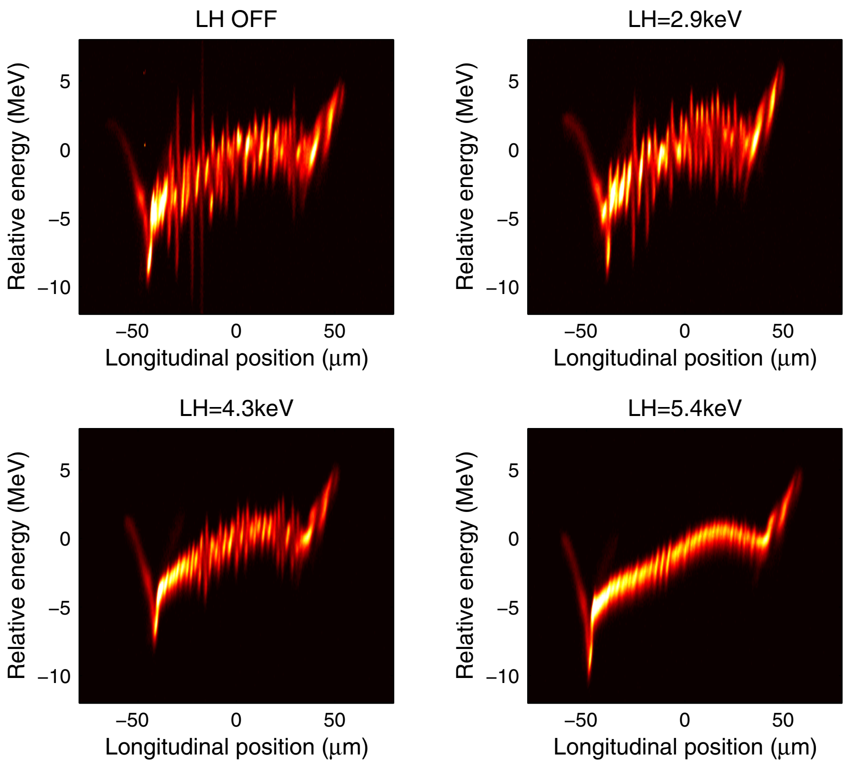

Figure 2.14: Measured electron longitudinal phase space for different laser heater-induced energy spread at LCLS [43].

with non-zero horizontal geometrical emittance ε_x moving with different betatron amplitudes, will follow different path lengths, along the dispersive section, so that (as long as $R_{51}, R_{52} \neq 0$) the MBI is suppressed at short wavelengths through transverse Landau damping ($LD_{\perp}$). To note that the latter damping mechanism affects only the modulations arisen within the dispersive section; e.g. in a bunch compressor these are the result of CSR effects and LSC cumulated along its length. The two damping term are thus given by

$$LD_{\|}(k;s) = \exp\Big\{-\tfrac{1}{2}\big[CkR_{56}\,\sigma_\delta(s)\big]^2\Big\} \tag{2.91}$$

$$LD_{\perp}(k;s) = \exp\Big\{-\tfrac{1}{2}(Ck)^2\,\mathscr{H}_x\varepsilon_x(s)\Big\} \tag{2.92}$$

where the H-function, thanks to the symplectic nature of the transport matrix $R_{6\times 6}$, can be expressed in the matrix formalism as [101]

$$\mathscr{H}_x = \frac{R_{52}^2 + \left(\beta_x R_{51} - \alpha_x R_{52}\right)^2}{\beta_x}\,, \tag{2.93}$$

In most practical cases, and in the range of wave numbers $k \leq \left(CR_{56}\sigma_\delta\right)^{-1}$ one finds that the longitudinal shift of electrons due to longitudinal dispersion is smaller than the compressed modulation wavelength ($CkR_{56}\frac{\Delta\gamma}{\gamma} < 1$), allowing the linearization $J_1(\zeta) \approx \frac{\zeta}{2}$ in Eq. 2.90. The energy modulations of Eq. 2.89 then can be integrated over all modulation frequencies to provide an equivalent instability-induced slice energy spread [53]

$$\frac{\sigma_{\gamma,\mathrm{MBI}}^2}{\gamma^2} = \frac{\sigma_z}{2\pi n_e}\int_{-\infty}^{+\infty}\frac{|\Delta\gamma(k)|^2}{\gamma^2}\,dk\,, \tag{2.94}$$

which is summed in quadrature to all the other contributions to the final energy spread.

MBI is further discussed in section 4.1 where we show the implementation and application of the analytical model for our studies.

Chapter 3

BoCXS: conceptual design upgrade and feasibility study

Inverse Compton scattering (ICS) represents a well-established approach for generating high-energy photon beams in the X-ray to gamma-ray regime [24, 25]. Early implementations were limited by the low emitted radiation intensity due to the small Thomson cross section; however, contemporary advancements in laser technology [102], which now provide photon pulses with energies on the order of joules per pulse, together with progress in the production and transport of high-brightness electron beams [103], have largely addressed these constraints. Since the realization of the first commercial light source, MuCLS [29], the number of proposed and funded inverse Compton sources has grown steadily over the past decade, following two primary design philosophies. In storage ring–based configurations—exemplified by ThomX in France [32] and MuCLS in Germany [104]—high fluxes of scattered radiation are obtained by enabling high-repetition-rate collisions between electrons and photon pulses circulating within Fabry–Perot optical cavities. Conversely, single-pass linac-driven systems such as Tsinghua X-ray in China [105], T-REX in the U.S. [33], and STAR in Italy [31], employ lower-emittance, shorter-duration electron bunches that interact at moderate repetition rates (up to 1 kHz using normal-conducting structures [106]) with intense photon pulses from high-power lasers. These ICS configurations are particularly attractive due to their compact footprint (in storage ring–based designs) and continuous tunability of photon energy (in linac-based designs), making them well suited for applications in tomography, protein crystallography and high-resolution medical imaging, with installations ranging from hospitals to universities and research centers. Additionally, increasing the X-ray energy to up to 1 MeV enables non-destructive testing in the mechanical and automotive industries, while in the field of cultural heritage science, operating within this energy range could expand the applications of conventional sources. Proposals also exist for ICS platforms based on energy-recovery linacs—such as CBETA in the U.S. [107] and KEK cERL in Japan [108]—although the superconducting technology requirements of these systems tend to restrict their practicality to larger research facilities rather than smaller laboratories or clinical environments.

The Bologna Compact X-ray Source (BoCXS) is a project which proposes the construction and operation of an inverse Compton scattering compact X-ray source in the Bologna metropolitan area, aiming to produce X-ray beams with characteristics similar, and possibly complementary, to those obtainable at large Synchrotron-based light sources, at a fraction of required space and cost, and with easier accessibility. Originally conceived as a twin-branch Compton back-scattered X-ray source featuring two alternatively operated electron-photon interaction points [50], the BoCXS Project has evolved, and we propose here a more versatile configuration in which electron bunches generated and accelerated by a high-gradient, all-C-band RF linac can be selected according to custom bunch patterns to concurrently feed two IPs in fast-cycling operation, with an envisaged output photon energies in the hundreds of keV. The selection of electron bunches—originating from the same photoinjector and main linac—is achieved via a novel switchyard line that preserves the six-dimensional beam brightness within a comparatively compact footprint. As an additional outcome of this accelerator configuration, a dedicated high-brightness electron beamline becomes available for applications such as beam diagnostics or ultrafast electron diffraction studies. This work represents a feasibility study of the machine in terms of electron beam dynamics, focusing on preserving electron beam quality from the source through the transport line up to the interaction points (IPs); thus the electron beam parameters are here the main figures of merit. Specifically, the innovative switchyard system is optimized for electron energies between 100 MeV and 170 MeV, making it compatible with any medium-energy linac-based ICS architecture. Start-to-end simulations confirm that the electron beam characteristics at the IPs are at least on par with those of other existing or planned single-pass ICS facilities operating in the same energy regime—for example, STAR-HE and T-REX. For each chosen electron energy, the photon energy range of the proposed

ICS is extended through second harmonic generation (SHG) applied to the incident infrared laser, increasing the energy by doubling the laser fundamental frequency at one of the two IPs. Furthermore, unlike storage-ring-based ICS—where electron-photon collisions are inherently head-on—this design incorporates specialized optical arrangements at the IPs that permit adjustment of the interaction angle, enabling fine-tuning of the emitted photon energy as well as selection of discrete X-ray energy bands aligned with the K-absorption edges of selected elements. Such spectral flexibility paves the way for advanced biomedical imaging techniques such as K-edge subtraction (KES) [35, 109]. We discuss here the evolution of the machine layout and the results of start-to-end simulations and optimization studies, performed making use of the tracking codes ASTRA [110] and ELEGANT [111]. More in detail, we focus on the characterization and optimization of the accelerating structure and beam transport through the new switchyard line, in order to maximize the beam brightness at the IP [112]. As discussed in this section, this study shaped the design choices for many aspects of the machine. We complement such study with the engineering details of innovative magnetic elements as well as laser-box configuration used to vary the interaction angle for precise spectral tuning of the scattered photons. Finally, and without any aim of numerical accuracy, analytical calculations are used to estimate the radiation parameters of the ICS.

3.1 BoCXS machine layout evolution

In the original BoCXS proposal [50], electron bunches accelerated up to 155 MeV in an S-band accelerating structure were alternatively guided, according to the polarity of a DC Y-Dipole, to two optical interaction points where they interacted with photon pulses produced by an Yb-YAG laser system, operating at the fundamental frequency (1032 nm) or its second harmonic (516 nm), as shown in Fig.3.1. This allowed producing ICS X-ray pulses in two different energy ranges, extending from below 100 keV up to about 800 keV, and alternatively feeding two user areas in a 3x12 m^2 footprint. The initial BoCXS concept is here heavily redesigned, as schematically shown in Figure 3.2. The following are the main novelties of the BoCXS' new machine design. The updated layout includes a fully characterized C-band photoinjector, with the inclusion of a drift space after the gun and solenoids to make room for vacuum pumping and diagnostic elements, and to facilitate the emittance compensation process. The high resonant frequencies of a designed C-band photoinjector allow the application of higher peak fields

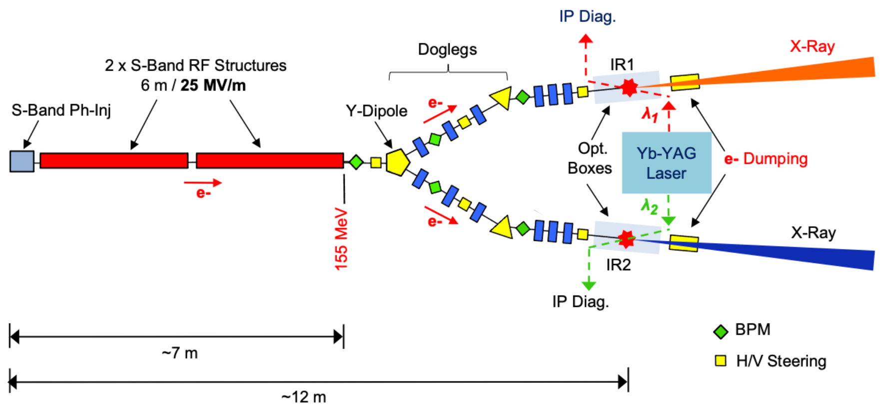

Figure 3.1: Original full S-Band draft configuration of BoCXS. Electron bunches accelerated up to 155 MeV in an S-Band Linac are transported through non-parallel doglegs up to the interaction regions IR1 and IR2 where they interact with photon pulses produced by a laser system operating on the fundamental wavelength or its 2nd harmonic [50].

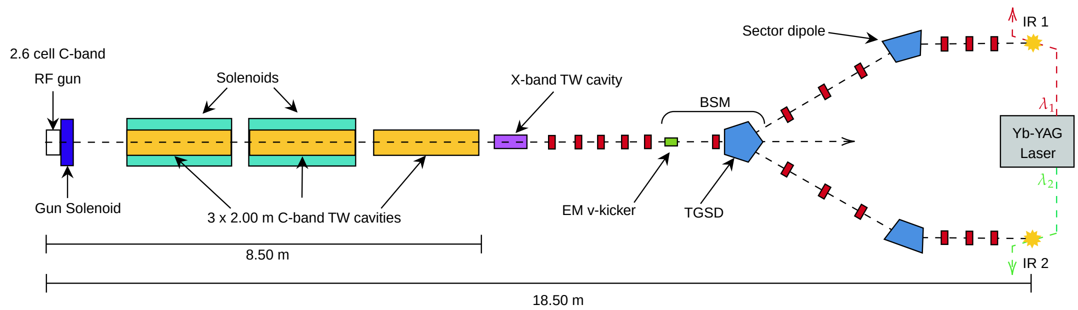

Figure 3.2: Sketch (not to scale) of the the new three-beamline BoCXS scheme, implemented with an all-C-Band linac followed an X-band linearizer and the Bunch Selection Module (BSM in the figure), providing a quasi-simultaneous multi-mode light production from the two interaction points. Two photon energy ranges can be selected according to the wavelengths ($\lambda_1 =$ 1032 nm or $\lambda_2 = 516$ nm) of the incident laser photons. The electron beam can be transmitted undeflected to a central beamline, passing through the Twin-Gap Septum Dipole (TGSD) in the BSM section, for beam diagnostics purposes as well as optional electron beam applications [112].

which are beneficial to the beam brightness, while providing compactness to the facility footprint. The C-band linac ends with an X-band cavity, to reduce the beam's correlated energy spread and preserve the beam current profile. This addition, in particular, revealed to be extremely beneficial to the beam quality. A compact five-quad matching section prepares the electron beam for transport through the Bunch Selection Module (BSM) and the doglegs, ensuring optics control at the IP while preserving the electron beam emittances. The BSM, in particular, provides options for a more flexible, quasi-simultaneous operation of two IPs and one additional direct high brightness electron beamline, at custom-selectable repetition patterns.

3.2 Preliminary photoinjector characterization

High-gradient RF photoinjectors are fundamental to the generation of high-brightness electron beams. Operating at C-band resonant frequencies allows the gun to sustain higher cathode fields—which directly enhance beam brightness [3]—while simultaneously lowering the likelihood of RF breakdown. Moreover, their inherently compact footprint makes them attractive for compact light-source applications.

This specific section of the work was conducted within the collaboration between the University of Bologna, as part of the BoCXS initiative, and the LNF, home to the EuPRAXIA@SPARC_LAB project [52].

An initial analysis considered the well known case of S-band photoinjector, comprising a 1.6-cell RF gun, a solenoid magnet for emittance compensation, a drift section after the gun and two traveling wave accelerating cavities. The RF gun peak field was set to 120 MV/m, while each TW cavity operated at 28 MV/m. We assumed a 0.5 nC bunch charge; the drive laser at the photocathode delivered an 14.5 ps (FWHM) flat-top pulse with 1.0 ps rise time and a uniform transverse profile characterized by $\sigma_r = 0.43$ mm. Following emittance compensation theory, beam dynamics simulations were performed in ASTRA to properly match the beam to the linac, thereby identifying a viable working point. We then applied scaling laws [113] to this solution, targeting C-band operation: resonant frequencies and field amplitudes were doubled, and the overall injector and bunch lengths were halved, while retaining the 0.5 nC charge per bunch. The effects of this scaling process are presented in Figure 3.3, showing how the beam dynamics is unchanged, apart from a global spatial scaling. This preliminary exercise both validated the scaling methodology and established the order of magnitude of beam parameters for the subsequent injector design.

The goal of this part of work was to conduct an optimization study based on a realistic C-band photoinjector model, configured for a single-bunch operation, aiming to achieve a set of high-quality beam parameters at the exit of the accelerating section. However, a straightforward scaling of the S-band design proves impractical: halving the total length yields an excessively short drift region after the solenoid, precluding installation of necessary vacuum pumping and diagnostic equipment. Moreover, doubling the peak fields in both gun and accelerating cavities is limited by technical

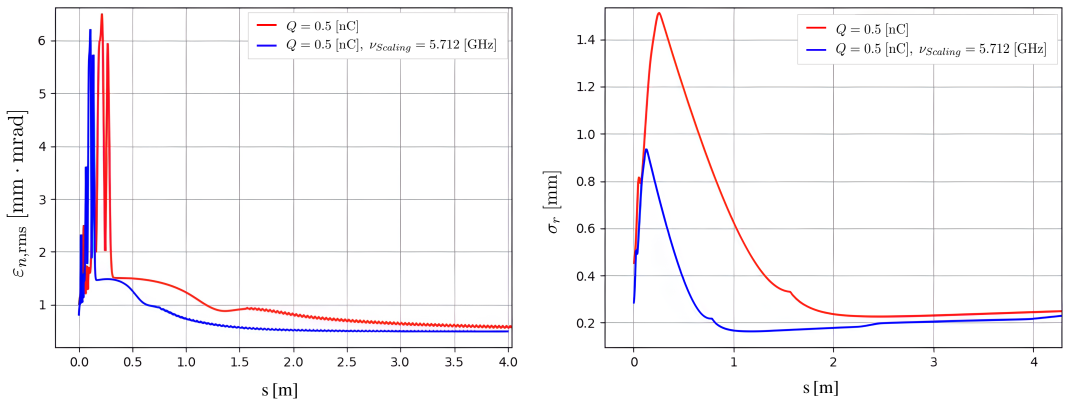

Figure 3.3: Normalized transverse emittance (left) and transverse beam size (right) evolution inside the photo-injector for an S-band (red) and a scaled C-band (blue) structure [114].

constraints—namely power dissipation in the RF structures and klystron power availability—which influence maximum achievable gradient and machine repetition rate. We therefore adopt a 0.1 kHz repetition rate, which supports peak fields of 180 MV/m in the gun and 40 MV/m in the TW cavities. To preserve analogous beam dynamics at these gradients (instead of the 240 MV/m from naive scaling), the RF gun is extended to 2.6 cells. Our final linac design is largely inspired by the one developed at the LNF, where the development of a C-band photoinjector has been proposed [115, 116] in the framework of the EuPRAXIA@SPARC_LAB. Such design, which can be seen in Fig. 3.2, employs a 2.6-cell gun followed by three C-band TW accelerating structures, each made of 114 cells at $2\pi/3$ phase advance per cell. The characterization was performed making use of the ASTRA tracking tools, which take into account space charge effects dominating at very low energies, to test both on-crest and velocity bunching operation, simulating 50k macroparticles. In order to assess the photoinjector operational performance, we undertook a simultaneous optimization of the final normalized transverse emittance and the relative energy spread at the photoinjector exit, independently of any eventual downstream beam-transport or compression elements. For the emittance minimization, we scanned the solenoid magnetic field, the drift-space length and the RF gun injection phase; conversely, energy-spread minimization was achieved by tuning the RF phase within the accelerating cavities. Equally critical are the photocathode laser parameters, which define the initial longitudinal and transverse bunch profile at emission [73]. In the absence of a dedicated bunch compressor—and under high-charge operation—longer laser pulses can mitigate non-linear components of space charge forces but amplify RF-curvature–driven energy spread, whereas shorter bunches amplify space charge forces, degrading transverse emittance at the cathode. Thus, the initial spot size and pulse duration at the cathode must be carefully balanced to achieve the desired beam quality. We began by adopting the same cathode beam distribution—namely a uniform transverse profile combined with a flat-top longitudinal shape aiming at the canonical cylindrical symmetry to minimize the nonlinear space charge contributions—while improving the laser rise time to 0.5 ps, and targeted a final beam energy of 165 MeV. The cylindrical symmetry of the extracted beam also allowed the adoption of the ASTRA 2-D space charge model in tracking. All simulations employed ASTRA autophasing capability, which automatically adjusts the injection phases of the RF cavities to maximize the energy gain of the reference particle. In the on-crest configuration, the peak fields in the first two TW cavities were fixed at 40 MV/m, while the third cavity was set to 23.65 MV/m and its phase adjusted to minimize the relative energy spread. We observed a final emittance < 0.5 mm mrad and relative energy spread $< 0.3\,\%$. Finally, simulations were conducted in the velocity-bunching regime to

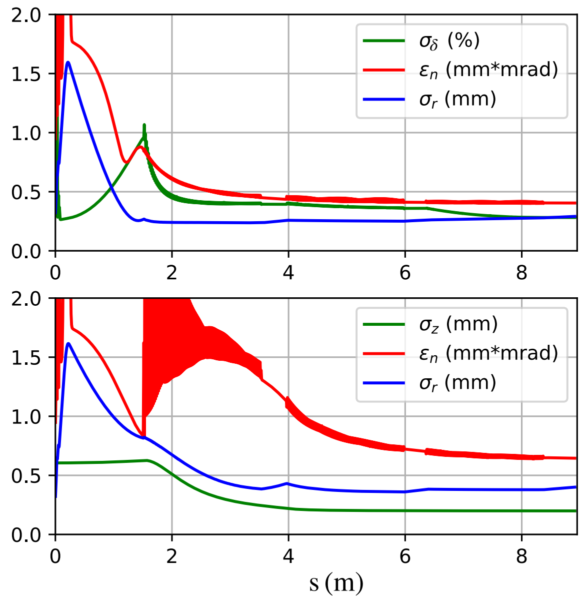

Figure 3.4: Simulation of beam evolution along the C-band photo-injector. On the top: beam envelope, emittance and energy spread evolution for the on-crest operation. On the bottom: beam envelope, emittance and bunch length evolution for the velocity bunching operation [114].

achieve higher peak current [76, 78, 114]. In this case, all three TW structures operated at 40 MV/m, the first cavity RF phase was shifted to –84 deg (with respect to the ASTRA autophase) to obtain a compression factor of 3, while the surrounding solenoid field was adjusted to maintaining spot size and emittance under control. In this regime we managed to obtain a slice peak current of 750 A, while maintaining an emittance of 0.65 mm mrad. Figure 3.4 compares the beam dynamics of both regimes for a bunch defined by the parameters in Table 3.1, which summarizes the optimized beam properties. Figure 3.5 presents the slice emittance and beam current profiles at the photoinjector

Table 3.1: Set of optimized beam parameters for the C-band photoinjector, with and w/o Bunch Compression

Parameter	**w/o BC**	**with BC**
Bunch charge [nC]	0.5	
Rep. rate [kHz]	0.1	
Laser rms spot size (Uniform)[mm]	0.3	
FWHM length pulse [ps]	8.5	
Rise time [ps]	0.5	
e-Beam final energy [MeV]	165	145
Norm. proj. emittance [mm mrad]	0.41	0.65
Bunch duration, rms σ_t [ps]	2.1	0.7
Transverse beam size, σ_r [mm]	0.3	0.4
Relative energy spread, σ_δ [%]	0.28	1.77
Slice peak current [A]	74	750

exit. The slice-by-slice analysis indicates that the emittance remains uniformly low across the full width at half maximum (FWHM) of the current distribution.

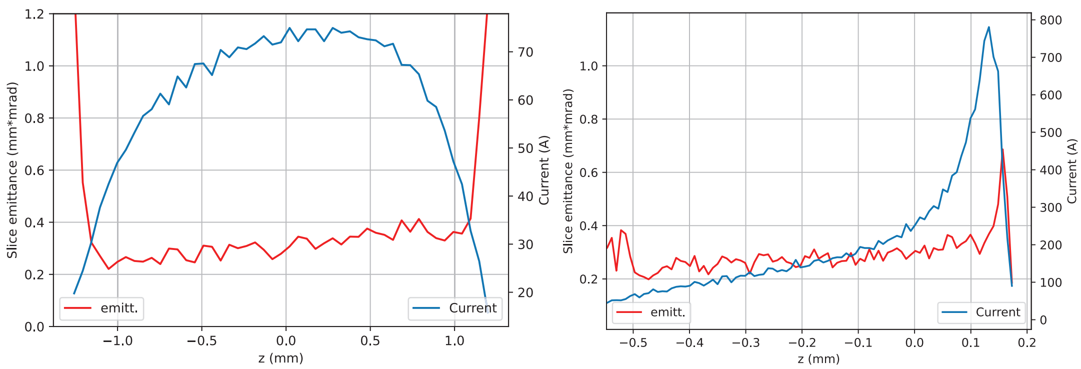

Figure 3.5: Slice analysis of the bunch at the end of the photo-injector for the on-crest operation (left) and velocity bunching (right) [114].

3.3 Photoinjector optimization for BoCXS

During the BoCXS redesign process, optimization studies prompted the inclusion of an X-band linearizing cavity immediately downstream of the C-band accelerating section.

As discussed in the following section, such cavity reduces the beam energy by a factor proportional to the energy gained in the photoinjector [117, 118]. To cope with the energy loss, the only precaution was to bring the peak field of all the C-band cavities to 40 MV/m, obtaining a beam energy of 190 MeV at the end of the C-band linac (unlike in the characterization previously discussed). The optimization yielded a gun injection phase of -5 deg (with respect to the autophasing) minimizes the emittance, while an adjustment of -5 deg (with respect to the crest) of the third TW cavity phase minimizes the energy spread. Table 3.2 lists the main photoinjector parameters resulting from our optimization study. As a part of the start-to-end study of the machine, we simulated

Table 3.2: Set of optimized parameters for the BoCXS C-band photoinjector and simulated electron beam parameters at its exit

Parameter	**Value**
Repetition rate [Hz]	100
C-band resonant frequency [GHz]	5.712
RF gun peak field gradient [MV/m]	180
TW Cavities peak field gradient [MV/m]	40
Gun solenoid peak field [T]	0.415
Solenoid 1 peak field [mT]	88.439
Solenoid 2 peak field [mT]	94.393
Gun laser rms spot size (Uniform)[mm]	0.3
Gun laser FWHM length pulse [ps]	8.5
Gun laser rise time [ps]	0.5
Bunch charge [nC]	0.5
e-Beam final energy [MeV]	190.3
Norm. proj. emittance [mm mrad]	0.42
Bunch duration, rms σ_t [ps]	2.1
Transverse beam size, σ_r [mm]	0.23
Relative energy spread, σ_δ [%]	0.28
Peak current, $\hat{I}$ [A]	74

in ASTRA 0.5 million macroparticels; Figures 3.6 shows the relative energy spread and transverse beam dynamics along the linac and the slice analysis of the bunch at the C-band linac end.

3.4 Phase space linearization

During the characterization and optimization of the beam transport line up to the interaction points, we found that chromatic aberrations in the quadrupoles led to an

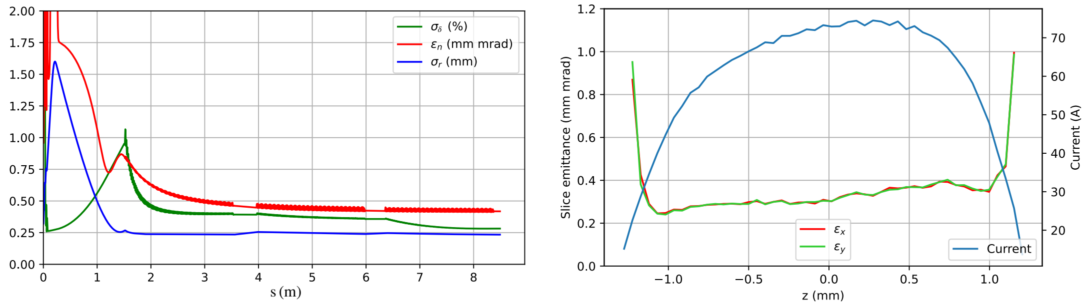

Figure 3.6: On the left: rms bunch length, normalized horizontal emittance and beam size from Gun to linac end. On the right: slice normalized emittace and peak current along the bunch at the linac exit [112].

increase in horizontal projected emittance of roughly 50 %. At the same time, the strong quadratic energy chirp imparted by the C-band linac coupling with the R_{56} and T_{566} elements of the dogleg transport matrices, produced a pronounced distortion of the current profile. Consequently, within the dipole magnets, coherent synchrotron radiation (CSR)—proportional to the derivative of the current distribution, as well as to the beam peak current—further degraded beam brightness, driving an additional $\sim 50\,\%$ growth in horizontal emittance. As a result, the horizontal emittance at the IPs was twice that at the linac exit, yielding a transverse beam size at the IP approximately 40 % above specification. These combined effects prompted the inclusion of an X-band linearizing cavity, which increased the length of the machine of about 1 m.

In this configuration, exploiting the second harmonic of the C-band resonance requires an effective voltage of approximately 46 MV. We therefore considered a 0.5 m long TW X-band cavity operating at a resonant frequency of 11.424 GHz. As detailed in Table 3.3, ELEGANT optimization yielded an injection phase of 269.72 deg and a cavity gradient of 92.4 MV/m [119, 120]. The X-band cavity then reduces the beam

Table 3.3: Set of optimized parameters for the X-band cavity

Parameter	**Value**
Repetition rate [Hz]	100
Cavity length [m]	0.5
X-band resonant frequency [GHz]	11.424
Field gradient [MV/m]	92.4
Injection phase [deg]	269.72
e-Beam final energy [MeV]	145
Final relative energy spread, σ_δ [%]	0.03

energy to 145 MeV, as shown in Fig. 3.7.

Using ELEGANT, we simulated a 0.5 million particle bunch, propagating directly the one exiting from the photoinjector, generated by ASTRA. CSR effects were included in the dogleg by employing ELEGANT's 1D CSR model, which accounts for both steady-state and transient CSR field contributions within dipole magnets [121], as well as CSR fields propagating through downstream drift sections [122]. This 1D CSR formulation—successfully benchmarked against experimental data [121, 123–125]—has been shown to remain valid over a wide range of beam and accelerator parameters, closely matching those used in this design.

Figures 3.8 and 3.9 illustrate the impact of longitudinal phase space linearization on both the beam current profile and the transverse emittance. The insertion of the X-band cavity removes the current modulations previously observed along the dogleg, thus strongly suppressing the CSR-driven increase in projected emittance within the dipoles. Furthermore, quadrupole chromatic aberrations—which depend on the beam relative energy spread—are also effectively eliminated by the linearization process, which reduces the projected energy spread by one order of magnitude. Table 3.4 summarizes the effects given by chromatic aberrations and CSR, both with and without longitudinal phase space linearization. All quantities are obtained from particle-tracking data (the peak current corresponds to the maximum longitudinal charge density).

It is worth to mention that the alternative option of a Ka-band linearizer has been recently considered in the context of the CompactLight project [126]. Coping with

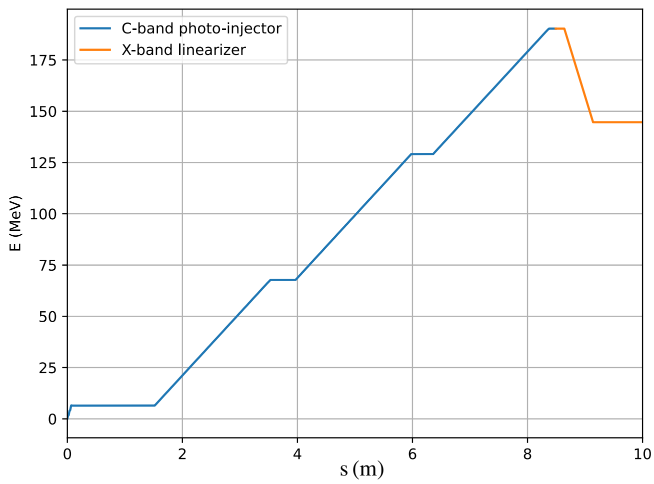

Figure 3.7: Electron beam mean energy along the accelerator [112].

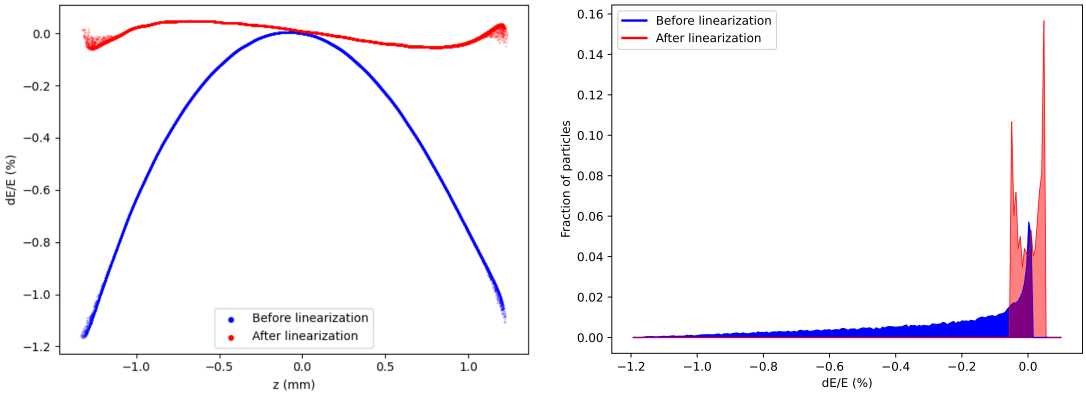

Figure 3.8: Longitudinal phase space of the electron beam at the end of the linac, before and after the X-band linearization (left), and corresponding energy distribution (right) [112].

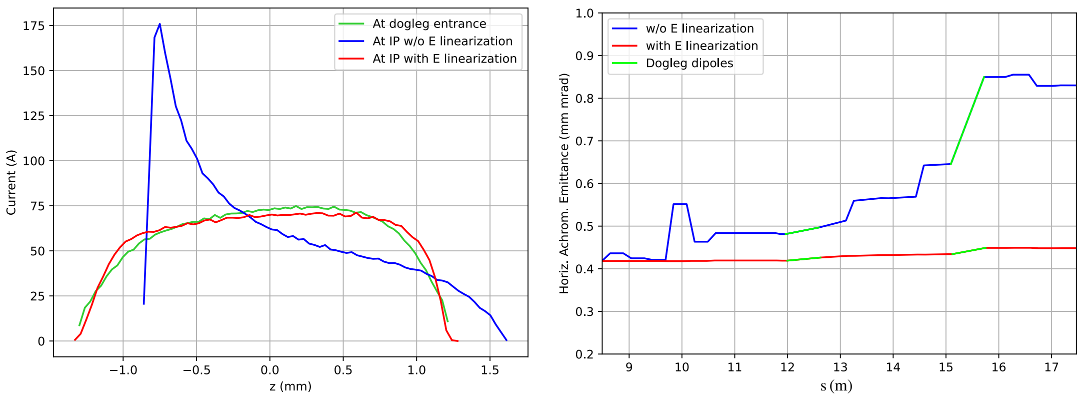

Figure 3.9: On the left: electron beam current profile at the IP, with and without X-band linearization. On the right: corresponding normalized horizontal betatron emittance (energy-normalized, subtracted of linear dispersion contribution) along the beamline. In the absence of linearization, current modulation causes large CSR-induced emittance growth in the second dipole of the dogleg. CSR and quadrupole chromatic effects are both suppressed by the linearization [112].

possible wakefields effects arising from such a small cavity, it would provide a lower energy loss during the linearization process, and it therefore represents an opportunity for a future design upgrade.

3.5 Bunch selection module

In the original BoCXS design [50], a DC Y-dipole sequentially directed the beam into one dogleg at a time. In contrast, the bunch selection module permits simultaneous operation of both ICS beamlines on a per-bunch basis, with user-defined repetition patterns. Alternatively, the BSM can be configured to let the electron beam continue

Table 3.4: Effects of chromatic aberrations and CSR on the beam quality from the linac end to the IP

	ε_x [mm mrad]	$\hat{I}$ [A]	σ_δ [%]
Linac exit	0.42	74	0.28
Without linearization			
At IP, CSR OFF	0.59	180	0.28
At IP, CSR ON	0.83	175	0.29
With linearization			
At IP, CSR OFF	0.42	71	0.03
At IP, CSR ON	0.45	71	0.03

straight along the linac axis without deflection. The BSM incorporates a fast electromagnetic kicker that imparts a vertical deflection of $\theta_k = \pm 33.1$ mrad to selected electron bunches. The induced vertical angle of the beam trajectory is then compensated by the off-axis passage of the beam through a dedicated vertically focusing quadrupole, forming a sort of vertical mini-dogleg, as schematically shown in Fig 3.10. Downstream

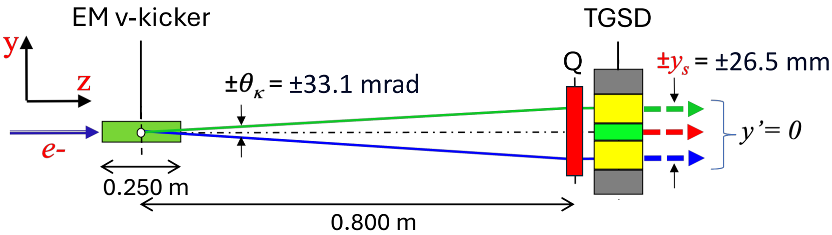

Figure 3.10: Schematic elevation view of the Bunch Selection Module. A pulsed bipolar electromagnetic kicker deviates selected electron bunches from the linac sequence into two vertically separated trajectories. The kicker deflections are compensated in the y-focusing quadrupole, and the resulting zero-slope trajectories are left-right deflected in the Twin-Gap Septum Dipole (TGSD). Undeflected electron bunches can be transmitted across the TGSD field-free region [112].

of such quadrupole, a Lambertson-type twin-gap septum dipole (TGSD) provides the horizontal deflection: its two superimposed magnetic gaps, set apart by a fixed vertical offset determined by the TGSD design, steer the upward-deflected bunches into the left dogleg and the downward-deflected ones into the right dogleg. As a result, the two beam transport lines and their respective interaction points lie on parallel horizontal planes, vertically separated by an offset of 53 mm introduced by the BSM. When the kicker is inactive, undeflected bunches traverse the field-free central region of the TGSD, continuing undisturbed along the linac axis (see Fig. 3.11).

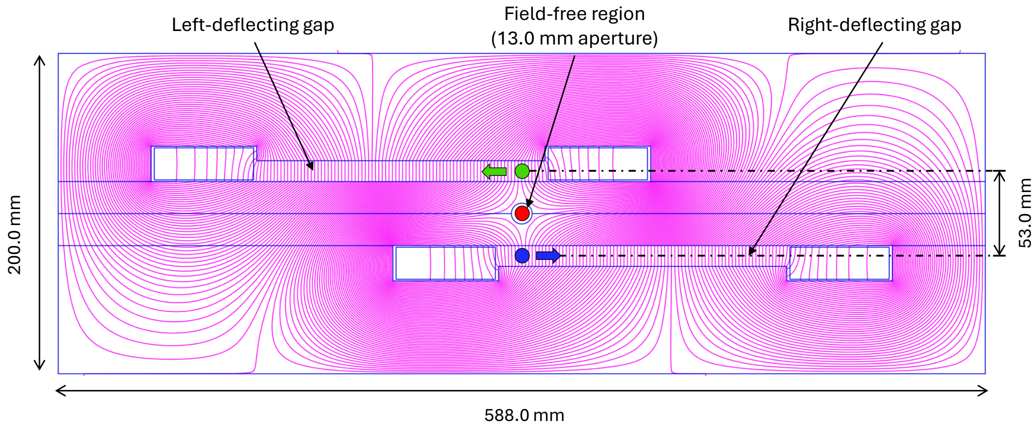

Figure 3.11: Vertical cross section of the Poisson-optimized twin-gap septum dipole. The magnetic field configuration was obtained from modeling with the POISSON/SUPERFISH code [127]. Top (bottom) gap deflects the incoming electron bunches in the left (right) direction. The field free region in the central slab allows transmitting the undeflected electron beam [112].

A scheme for a ferrite-loaded electromagnetic kicker is illustrated in Fig. 3.12. The single-sheet kicker coil generates a bipolar pulsed magnetic field B_k that provides

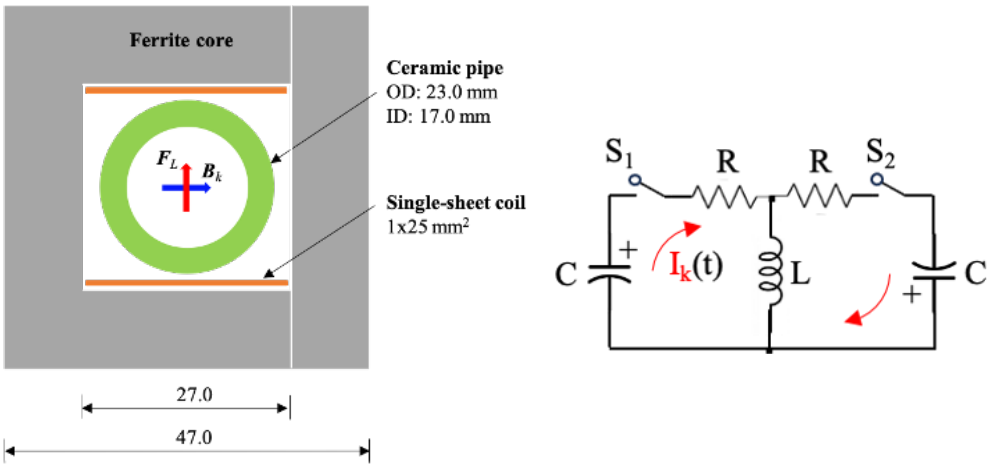

Figure 3.12: Vertical cross section of the Kicker setup (left) and its RLC driving scheme (right). [112].

opposite-sign vertical deflections $\pm\theta_k$ to incoming bunches, with $\theta_k = y_s/l$, where y_s is the vertical offset at the TGSD entrance and l is the distance between the kicker and the compensating quadrupole (see Fig. 3.10). In the RLC drive configuration shown in Fig. 3.12, two capacitor banks discharge current in opposite directions through the coil whenever switch S_1 or S_2 is closed, thus producing bipolar deflecting pulses at a

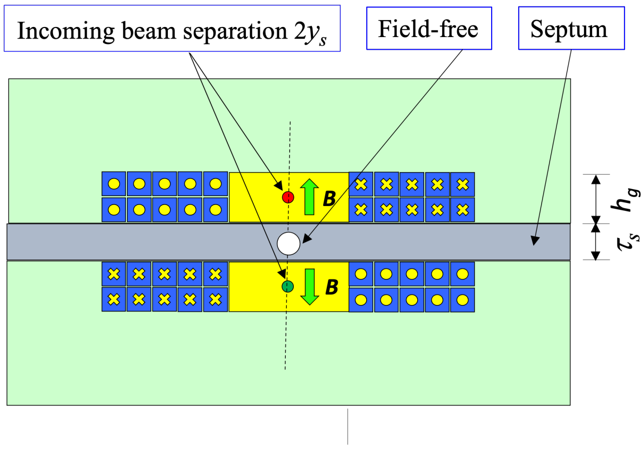

Figure 3.13: Vertical cross section of a window-frame symmetric twin-gap septum dipole providing left-right deflections via opposite B-fields in two superimposed gaps [112].

user-defined repetition rate.

In a conventional twin-gap septum dipole configuration (Fig. 3.13), two vertically superimposed gaps—filled with opposite-sign magnetic fields—separated by a septum, impart horizontal deflections to beam trajectories vertically offset by $2y_s$. In the asymmetric TGSD variant developed for the BSM scheme (Fig 3.11), the design focuses on containing the vertical displacement $2y_s$ within the geometric constraints of the gap height h_g and septum thickness τ_s, such that $2y_s = h_g + \tau_s$. Therefore, in contrast to the symmetric design, the asymmetric TGSD geometry employs reduced horizontal apertures in its deflecting gaps—sized solely to accommodate the actual left- and right-deflected beam excursions—so as to contain the magnetic flux within the septum. Assuming a 2 T figure for the magnetic induction in the septum and using the design values from Table 3.5, the optimized beam separation at the TGSD entrance is $2y_s = 53.0$ mm. A set of key BSM parameters are summarized in Table 3.5. The BSM, composed by the ferrite-loaded vertically deflecting kicker, the quadrupole and the TGSD (either acting as a sector dipole or a drift space) are designed to be a single module, with fixed optical parameters (scalable with the beam energy). Consequently, a dedicated matching section downstream of the linac was an essential requirement in the final layout.

Table 3.5: Main BSM parameters (nominal energy)

Parameter	Value
Beam energy [MeV]	145
Drift length (kicker to Q) [mm]	625.0
EM v-kicker	
Rep. rate [Hz]	100
Rise time [μs]	$\sim$5
Pulse duration [μs]	50
Deflecting field [T]	$\pm$0.064
Deflection angle [mrad]	33.1
Core length [mm]	250.0
Quadrupole	
Strength [m^{-2}]	-12.78
Core length [mm]	100.0
Aperture [mm]	70.0
TGSD	
Incoming beam offset [mm]	$\pm$26.5
Nominal deflection [deg]	$\pm$30
Arc length [mm]	628.0
B-field [T]	$\pm$0.403
Dipole height [mm]	200.0
Dipole width [mm]	588.0

3.6 Electron beam transport to the interaction point

The doglegs, divergent in the original BoCXS layout, are now parallel, to simplify the lattice design and minimize the lateral footprint of the facility. Characterization and optimization of these transport lines were performed using ELEGANT, which incorporates models for coherent synchrotron radiation [124, 125] and longitudinal space-charge forces [128]. All results presented here stem from tracking 0.5 million macroparticles, with seamless beam-dynamics continuity ensured by the use of ASTRA output distribution as input to ELEGANT. The optimization scope included every element downstream of the final C-band cavity (see Fig. 3.2): the X-band cavity, the five-quadrupole matching section, the BSM, the quadrupole triplet within each dogleg, the second sector dipole, and the focusing triplet immediately upstream of the IP. The optimized beam evolution through the transport to IP is shown in Fig. 3.14.

The matching section was optimized to suppress vertical emittance growth through the BSM while providing the correct optics for dogleg injection, where the TGSD and sector dipoles deviate the beam trajectory horizontally by ±30 deg. Indeed, acting as a vertical mini-dogleg, the BSM introduces a small vertical dispersion (< 10 cm) that, by machine design, cannot be properly eliminated, as shown in Fig. 3.14 (right). If

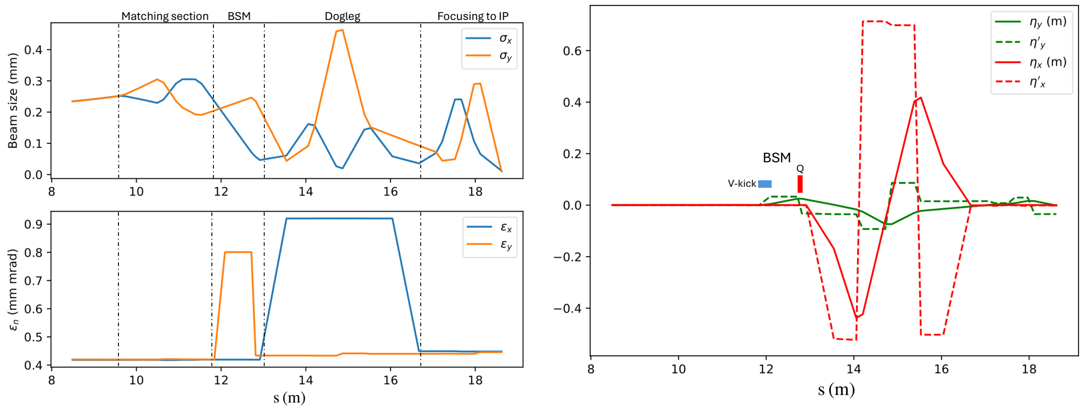

Figure 3.14: Beam evolution from the linac exit to IP. On the left: electron beam sizes and projected transverse normalized emittances (inclusive of dispersion contribution). On the right: momentum dispersion functions [112].

not handled adequately, this may potentially become a showstopper, as the projected emittance in a dispersive section is given by

$$\varepsilon = \sqrt{\varepsilon_0^2 + \varepsilon_0 \mathscr{H} \sigma_\delta^2}\,, \tag{3.1}$$

where ε_0 is the achromatic (betatron) emittance (i.e. the initial one, before the dispersion is introduced) and $\mathscr{H}$ is the *dispersion-invariant*, also known as chromatic H-function, representing the dispersion contribution to the projected emittance which is defined as

$$\mathscr{H}_u = \gamma_u \eta_u^2 + 2\alpha_u \eta_u \eta_u' + \beta_u \eta_u'^2\,, \qquad \text{with} \quad u = x, y\,, \tag{3.2}$$

where β_u, γ_u and α_u are the Twiss parameters, while η_u and η_u' are the dispersion function and its derivative respectively. The H-function is indeed an invariant, which can be modified only by the presence of a dipolar field component, in our case provided by bending magnets (either sector dipoles or the EM kicker) or by the off-axis quadrupole. One usually drives the dispersion and its derivative to zero at the dogleg exit, through systematic tuning of the quadrupoles between the two dipoles, therefore eliminating the dispersion contribution to the emittance. This is what we do for the horizontal dogleg, but for the vertical mini-dogleg, represented by the BSM, the same strategy cannot be applied. However, one can suppress the dispersion contribution to the emittance also by providing a proper combination of Twiss parameters in order to minimize Eq. 3.2 at the BSM exit, as shown in Fig. 3.15. This technique is further discussed in Appendix A.

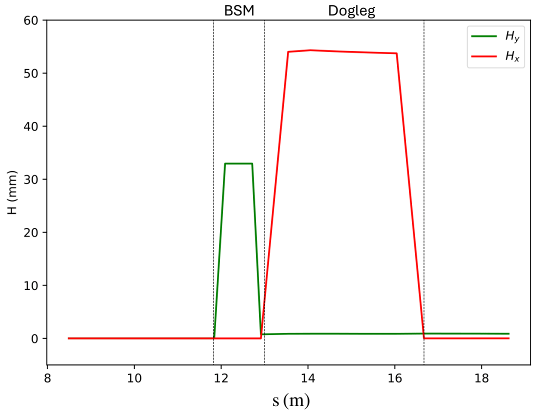

Figure 3.15: Chromatic H-functions along the beamline. The horizontal H-function is made null by zeroing the horizontal dispersion and its derivative at the dogleg exit, while the vertical one is minimized by providing the proper optical matching to the BSM.

Thus, by carefully tuning quadrupole strengths in the matching section, an optimal balance of betatron and chromatic effects is achieved, making dispersion-induced vertical emittance growth negligible, and therefore recovering both transverse emittances to near their initial values (see Fig. 3.14). A final quadrupole triplet then focuses the beam to the IP, yielding a transverse size of $\sigma_r \approx 10$ μm. Moreover, the residual vertical dispersion η_y at the interaction point is driven to zero, therefore removing any dispersive contribution to the beam size and effectively decoupling the beam's vertical position from energy deviations. This ensures that any upstream energy jitter does not translate into spatial misalignment at the IP, thereby preserving beam–laser overlap and stabilizing the interaction.

Direct transverse space-charge forces were not included in the beam dynamics optimization with ELEGANT. To account for this, we supplemented the tracking study with an analytical evaluation of the laminarity parameter [62] along the entire transport line, which is estimated here as

$$\rho = \frac{\hat{I}\sigma_{eff}^2}{2I_A\gamma\varepsilon_{eff}^2}\,, \tag{3.3}$$

where

$$\sigma_{eff} = \sqrt{\frac{\sigma_x^2+\sigma_y^2}{2}}\,, \quad \text{and} \quad \varepsilon_{eff} = \sqrt{\varepsilon_{nx}\varepsilon_{ny}} \tag{3.4}$$

are the quadratic mean of the beam envelopes and the geometric mean of normalized beam emittances respectively. A full investigation of direct space-charge effects along the transport line is deferred to future work; however, the laminarity parameter shown in Fig. 3.16 indicates that the beam dynamics is mostly dominated by the emittance pressure, hence confirming the validity of ELEGANT simulations. Figure 3.17 shows

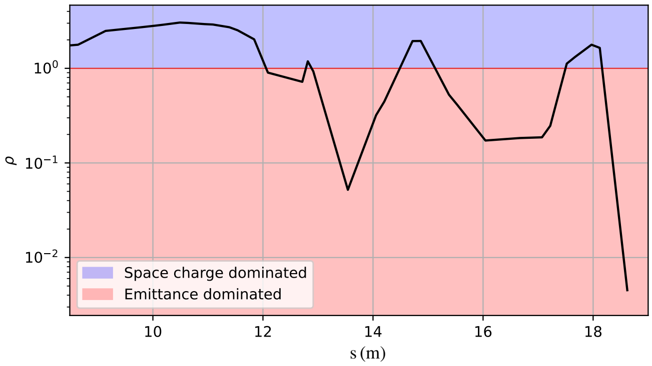

Figure 3.16: Laminarity parameter from linac end to IP [112].

slice emittance and current profile of the beam at IP, while Fig. 3.18 shows the transverse phase space contour plots. Finally Table 3.6 lists the simulated beam parameters,

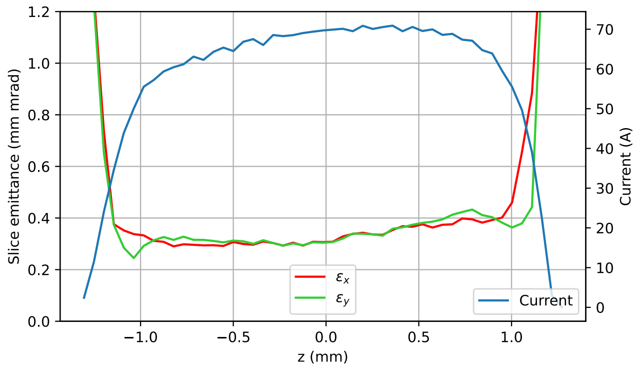

Figure 3.17: Slice normalized emittace and peak current along the bunch at the IP [112].

comparing them with those at the exit of the photoinjector.

3.7 Jitters stability study

The stability study of the machine has been carried out by introducing various sources of shot-to-shot jitters in the simulation, aiming at testing the robustness of the optimized optics configuration. The shot-to-shot jitters considered in this study involved the time

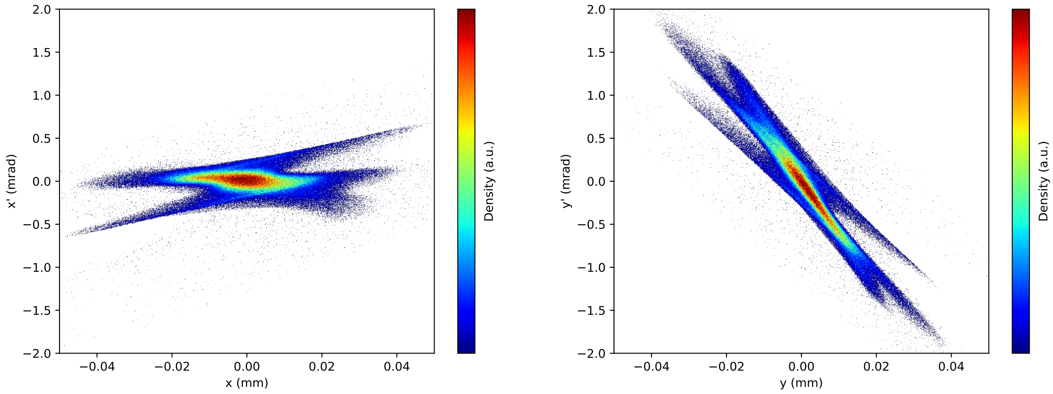

Figure 3.18: Horizontal (left) and vertical (right) phase space contour plot of the beam at IP [112].

Table 3.6: Simulated nominal electron beam parameters

Parameter	@C-band exit	@IP
Bunch charge [nC]	0.5	0.5
e-Beam final energy [MeV]	190	145
Norm. proj. emittance [mm mrad]	0.42	0.45
Bunch duration, rms σ_t [ps]	2.1	2.2
Horizontal beam size, σ_x [μm]	234	12
Vertical beam size, σ_y [μm]	234	10
Relative energy spread, σ_δ [%]	0.28	0.03
Peak current, $\hat{I}$ [A]	74	71

of arrival of the cathode laser, the total charge, the beam spot size, the BSM kicker deflecting field, and the phases and amplitude of the various RF cavities, as listed in the Table 3.7. All the values considered represent the state-of-the-art technological

Table 3.7: Jitter values (rms) used in the stability study

Subsystem	Parameter	Jitter
C-band gun and accelerating sections	RF Voltage [%]	0.02
	RF Phase [deg]	0.02
X-band cavity	RF Voltage [%]	0.02
	RF Phase [deg]	0.08
Cathode laser system	Time of arrival [fs]	30.0
	Charge [%]	2.0
	Spot size [%]	1.0
BSM EM v-kicker	Deflecting field [%]	0.02

capabilities of the machine elements [129–134]. The machine sensitivity study have been performed on a sample of 50 machine runs (due to computational limits). For the first part of the machine (up to the exit of the C-band section) we made use of GIOTTO, a software based on a Genetic Algorithm, designed to interface with ASTRA [135]. The interface between GIOTTO and ASTRA (or ASTRA's generator) inherently includes the capability to easily generate and manipulate input files. For the last part of the machine we used ELEGANT and its built-in tools for jitter studies.

The overall machine robustness to jitters is studied by evaluating the beam quality and stability at the interaction point. Table 3.8 presents the results of the study, collecting the values of the main beam parameters and their unbiased standard deviations. Figure 3.19 shows the statistical distributions of the beam final energy and relative energy spread, Fig. 3.20 depicts the slice analysis of the 50 shots, while Figs. 3.21 and 3.22 show the emittances and centroids distributions at the IP.

Table 3.8: Statistical beam parameters at the interaction point, resulting from 50 simulation runs

Parameter	**Value**
Final energy [MeV]	145.084 ± 0.023
Norm. horizontal emittance, ε_{nx} [mm mrad]	0.444 ± 0.013
Norm. vertical emittance, ε_{ny} [mm mrad]	0.438 ± 0.012
Horizontal beam size, σ_x [μm]	12.00 ± 0.26
Vertical beam size, σ_y [μm]	10.00 ± 0.33
Bunch duration, rms σ_t [ps]	2.157 ± 0.016
Relative energy spread, σ_δ [%]	0.030 ± 0.004
Peak current, $\hat{I}$ [A]	71.33 ± 0.68
Horizontal centroid jitter, rms [μm]	0.23
Vertical centroid jitter, rms [μm]	3.51
Time of arrival jitter, rms [ps]	0.030

The analysis of jitter effects confirms that the machine exhibits a high degree of robustness against active elements' jitters. All relevant beam parameters remain well within the specifications, showing only minor deviations of a few percentage points from their nominal design values. In particular, the vertical centroid stability is dominated by the jitter of the BSM kicker, resulting in an rms value one order of magnitude higher with respect to the horizontal centroid jitter. However, considering a laser spot size at the IP of 15 μm, the expected mean decrement of luminosity for the ICS is $\sim 2\,\%$, with a $2.5\,\%$ rms. These results indicate that the overall machine performance is not significantly compromised by the considered sources of jitter, thus ensuring operational

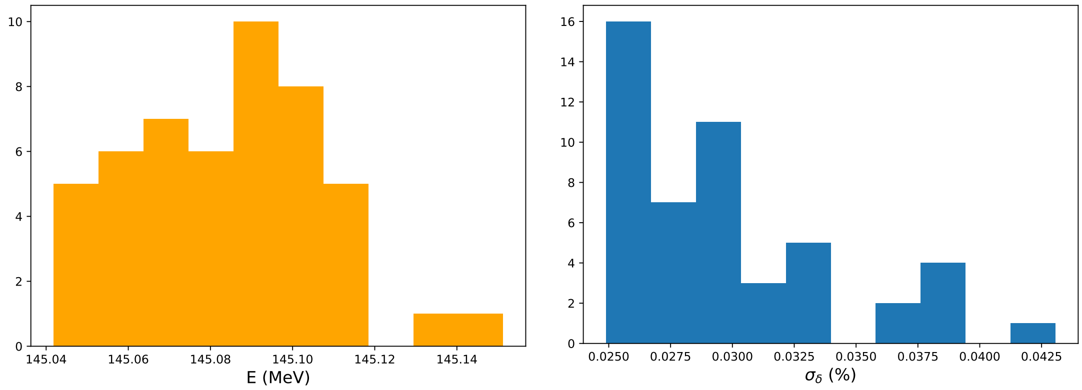

Figure 3.19: Final beam energy (left) and relative energy spread (right) distributions, resulting from 50 simulation runs.

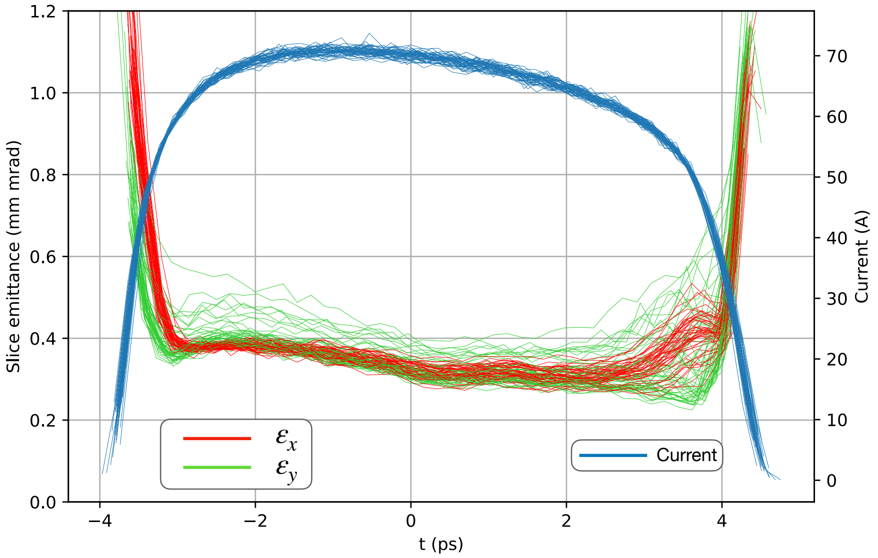

Figure 3.20: Slice analysis of the 50 shots at the interaction point.

reliability under realistic conditions.

3.8 Photon energy selection and tuning

The energy of the emitted radiation from an Inverse Compton scattering in the laboratory frame can be expressed as [104, 136, 137]:

$$E_X^{ICS} \approx \frac{2(1+\cos\varphi)}{1+(\gamma\theta)^2} E_{ph}\gamma^2 \,, \tag{3.5}$$

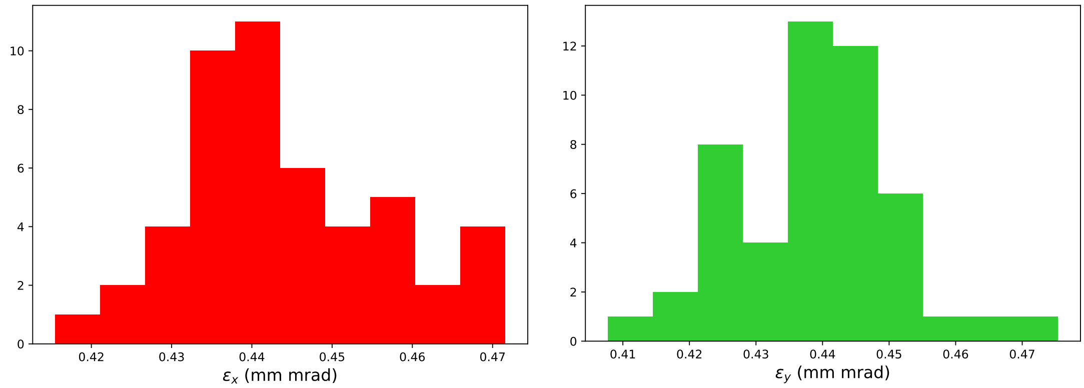

Figure 3.21: Horizontal (left) and vertical (right) normalized projected emittance distributions at IP, resulting from 50 simulation runs.

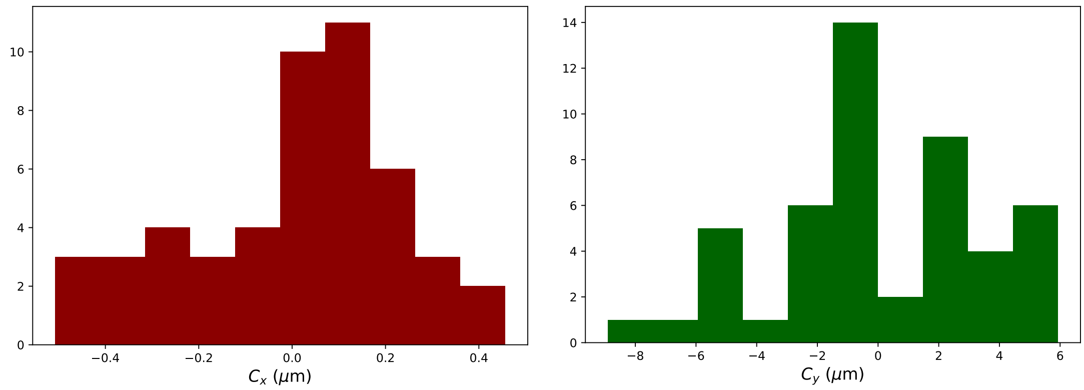

Figure 3.22: Horizontal (left) and vertical (right) centroid distributions at IP, resulting from 50 simulation runs.

where E_{ph} is the energy of the incoming photons and the contribution from the recoil of the incoming electron is neglected (a 5×10^{-3} effect in our case). Equation 3.5 captures how the emitted photon energy varies with the interaction angle φ, the laser central wavelength, and the electron beam energy, for any fixed scattering (observation) angle θ. In the following sections, we examine both discrete and continuous spectral tunability of the ICS output as functions of these key parameters.

3.8.1 Spectral tunability of back-scattered radiation

For any given electron energy, the photon energy (Eq. 3.5) can be doubled by frequency-doubling the drive laser via Second Harmonic Generation (SHG) [138]. In SHG, two photons at the fundamental frequency coherently interact within a nonlinear crystal to produce a single photon at twice the frequency. As a result, the emerging pulse contains half the initial photon count, with each photon carrying twice the energy of the input photons. In the optical layout depicted in Fig. 3.23, the infrared drive laser at $\lambda_1 = 1032$ nm is frequency-doubled to $\lambda_2 = 515$ nm using a type-I nonlinear crystal. After optical separation of the fundamental and second-harmonic components,

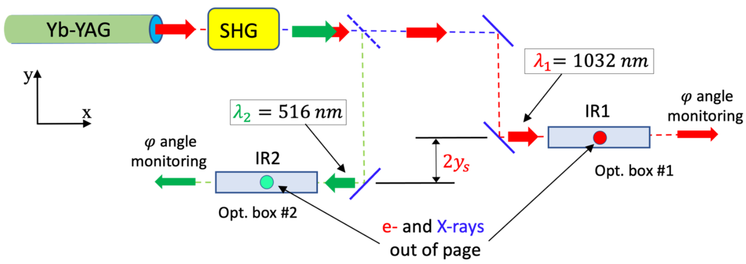

Figure 3.23: Dual-frequency operation adopting Second Harmonic Generation (SHG). The IR1 and IR2 optical boxes are vertically shifted by the $2y_s$ offset between the electron trajectories downstream the TGSD dipole. The electron and the X-ray beams travel orthogonally to the page [112].

the two pulses are routed into their dedicated IP optical boxes, which are mounted on horizontal planes with a $2y_s$ vertical offset to coincide with the corresponding electron beam trajectories.

At the nominal beam energy of 145 MeV and 100 Hz repetition rate, the on-axis ICS photon energies are 383 keV for the fundamental laser wavelength λ_1 and 767 keV for its second harmonic λ_2. Nearly continuous tuning of the photon energy can be achieved by adjusting the C-band linac RF amplitudes and phases. In fact, our simulations indicate that deactivating the final C-band cavity—either by switching it off or by delaying its RF pulse relative to the beam—and consequently adjusting the X-band cavity voltage, reduces the electron energy to ~ 100 MeV while still preserving beam brightness through the transport line. Accordingly, with the betatron functions held fixed, adiabatic damping is reduced, causing both the geometric emittances and the transverse beam sizes at the IP to increase, alongside a rise in relative energy spread. Without re-optimizing the IP optics, the beam size reaches roughly 15 μm and the energy spread grows to about 0.04 %. A 100 MeV central electron beam energy corresponds to an on-axis ICS photon energy of 182 keV for λ_1, at the nominal interaction angle of 3 deg.

Further spectral tuning is achieved by varying the interaction angle φ: at $\varphi = 35$ deg, the on-axis photon energy shifts to approximately 166 keV. Additionally, moving the observation angle to $\theta \sim 1/\gamma$ lowers the selected X-ray energy to about 80 keV, at the cost of roughly a tenfold decrease in photon intensity compared to the on-axis emission.

Conversely, increasing the electron beam energy to 166 MeV raises the upper limit of the on-axis ICS photon energy at the second-harmonic wavelength λ_2 to approximately 1 MeV. Achieving this requires an 18 % increase in the C-band accelerating gradient—from 40 MV/m to $\sim$ 47 MV/m—while lowering the repetition rate to 70 Hz maintains constant the average RF power. The resulting higher beam energy enhances magnetic rigidity, reducing sensitivity to collective effects, and thereby preserving beam brightness throughout the switchyard transport.

3.8.2 Tuning the interaction angle

The radiated flux in an ICS characterized by the Thomson cross section $\sigma_T = 0.665$ b also depends on the interaction angle φ according to [139, 140]:

$$\dot{N}_X^{ICS} = \frac{\sigma_T N_e N_l}{2\pi\Sigma_y\sqrt{\Sigma_x^2 + \Sigma_z^2\tan^2(\varphi/2)}} f\,, \tag{3.6}$$

where N_e is the electron bunch population, N_l is the number of photons in the laser pulse and f is the collision rate. The convoluted bunch dimensions are:

$$\Sigma_{x,y} = \sqrt{w_0^2/4 + \sigma_{x,y}^2}\,, \quad \Sigma_z = c\sqrt{\tau_l^2 + \sigma_t^2}\,, \tag{3.7}$$

where $w_0 = 2\sigma_l$ is the waist of the photon pulse characterized by a transverse rms dimension σ_l at the IP, τ_l and σ_t are the rms time durations of the colliding beams, and $\sigma_{x,y}$ is the electron bunch rms transverse dimension.

In contrast to storage ring-based ICS—where electron-photon collisions are essentially head-on and the interaction angle is fixed—single-pass linac-based ICS permit adjustment of the interaction angle φ over a wide range, starting from a nonzero minimum value and limited only by the optical layout of the laser–electron interaction region. Exploiting the φ-dependence of key performance metrics—such as photon energy, flux intensity, pulse duration and transverse beam size—provides operational flexibility that compensates for the lower peak flux relative to quasi-head-on geometry. In particular, this angular tunability also enables rapid, dual-color K-edge subtraction imaging by fine-tuning the scattered photon energy, an option that is precluded in a quasi-head-on only operation.

In the optical arrangement of Fig. 3.24, two sets of off-axis parabolic mirrors (OAPs) designed for KES dual-color imaging, define two discrete interaction-angle ranges as the input laser is steered by movable mirror M_1 across the main mirror M_2. The minimum

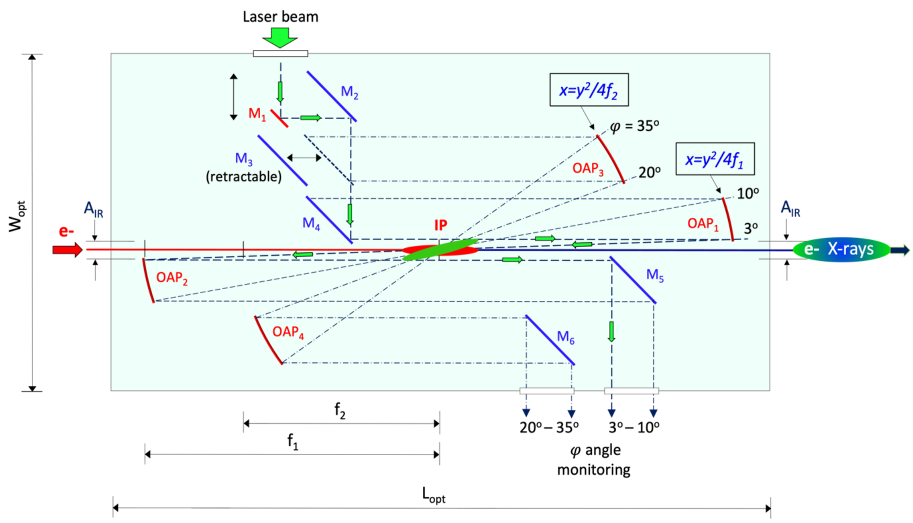

Figure 3.24: Layout of the optical box at one of the laser-electron interaction regions. Two sets of OAP mirrors select the interaction angle φ within an operational range of $\Delta\varphi_1 = 3$–10 deg and a larger set of $\Delta\varphi_2 = 20$–35 deg to produce X-ray energy shifts of the order of 2–3 keV for KES dual-energy imaging. The operational value of the interaction angle φ is defined by the position of the scanning mirror M_1 with respect to the M_2 and M_3 mirrors and monitored via angle-to-position correlation through the$M_{5,6}$ extracting mirrors. The arrows highlight the laser path corresponding to a $\varphi = 3$ deg interaction angle [112].

angle $\varphi_{min} = 3$ deg is indicated by the arrowed beam path. For the nominal, quasi-head-on mode, mirrors M_4 and OAP$_1$ select $\Delta\varphi_1 = 3$–10 deg, allowing fine-tuning within that interval. Inserting retractable mirror M_3 in conjunction with OAP$_3$ establishes a second range $\Delta\varphi_2 = 20$–35 deg, producing $\sim$2–3 keV shifts in X-ray energy for KES imaging when combined with $\Delta\varphi_1$. Rapid actuation of mirrors M_3 and M_6 facilitates data acquisition across the material K-edge. Downstream optics (OAP$_2$, OAP$_4$ and mirrors M_5, M_6) recover the transmitted laser and provide φ-to-position monitoring for both $\Delta\varphi_1$ and $\Delta\varphi_2$. The focal length f_1 of OAP$_{1,2}$ is defined by φ_{min} and a clearance $A_{IR} = \pm 10$ mm for the ingoing/outgoing electron and X-ray beams at the mirror edges, while the placement of OAP$_{3,4}$—chosen to contain the dimensions of the optical box and to avoid optical interference with the OAP$_{1,2}$—determines a secondary focal length f_2. Each OAP aperture is defined by the parabolas and is sized based on the contributions of the laser beam divergence at the IP, the laser beam waist $w_0 = 30$ μm and the quoted ranges of the interaction angle. Main optical parameters are listed in Table 3.9.

Table 3.9: Optical Box parameters

Symbol	Value	Function
$\Delta\varphi_1$ [deg]	$3-10$	Operational φ range
$\Delta\varphi_2$ [deg]	$20-35$	Additional φ range
$\mathrm{OAP}_{1,2}$ [mm]	60	$\Delta\varphi_1$ range
f_1 [mm]	375	
$\mathrm{OAP}_{3,4}$ [mm]	80	$\Delta\varphi_2$ range
f_2 [mm]	276	
M_1 [mm]	30	Scanning
M_2 [mm]	90	
M_3 [mm]	90	$\Delta\varphi_2$ selection
M_4 [mm]	85	$\Delta\varphi_1$ selection
M_5 [mm]	85	φ-monitoring
M_6 [mm]	90	
A_{IR} [mm]	± 10	Outgoing beam clearance
$\mathrm{W}_{\mathrm{opt}}/\mathrm{L}_{\mathrm{opt}}$ [mm]	420/820	Box dimensions

3.9 ICS expected performance

Analytical estimates of the back-scattered photon properties for BoCXS have been performed using formulae that, while not intended to aiming for high numerical accuracy, have been successfully benchmarked against specialized ICS simulation codes and are well established in the literature. The model—outlined in Appendix B for reference—accounts for normalized laser bandwidth, transverse emittance and energy spread of the electron beam, both beam and laser pulse durations, and electron recoil. Results from this model are presented in Table 3.10, which summarizes the expected ICS performance. The hourglass effect is negligible, as $\sigma_z/\beta_{x,y} \ll 1$, and diffraction effects remain small since the laser pulse duration is shorter than its Rayleigh length. In this evaluation, the BoCXS performance is reported for single-beamline operation; under a multimodal regime, all quoted figures scale down in direct proportion to each beamline's duty cycle. For reference and completeness, Table VI also lists the simulated electron-beam parameters, the incident laser specifications [141], and the analytically derived ICS outputs of BoCXS are compared to the corresponding metrics for facilities in the same energy range—namely STAR-II-HE and T-REX.

Figure 3.25 has been generated using the same model, showing the X-ray spectral density computed with and without longitudinal phase space linearization through the X-band cavity. Implementing linearization boosts the ICS spectral density by roughly

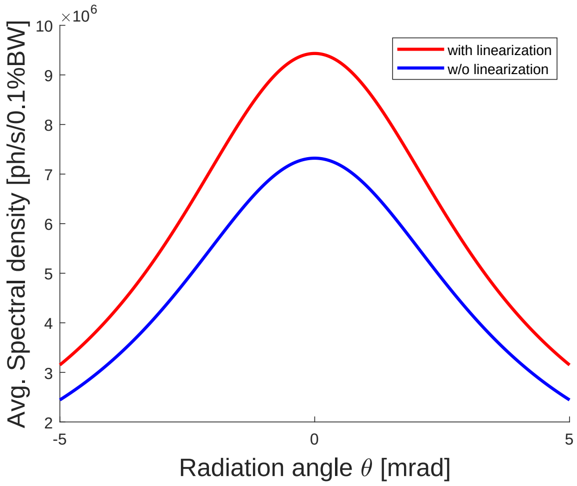

Figure 3.25: Calculated X-ray spectral density with (red) and without (blue) linearization of the longitudinal phase space, as a function of the radiation angle θ. An acceptance angle of 0.5 mrad at each θ and laser fundamental wavelength λ_1 are assumed. The corresponding photon energy varies from 127 keV at $\theta = \pm 5$ mrad to 382 keV on axis ($\theta = 0$) [112].

30 %, owing to the reduced transverse emittance and energy spread of the electron beam. Even more crucially, linearization produces a smoothed, near flat-top current profile, as shown in Fig. 3.9, which promotes uniform matching of bunch slices to the nominal Twiss parameters and yields an almost constant scattered-radiation intensity throughout the X-ray pulse.

Table 3.10: Nominal electron beam, incident laser and back-scattered Compton radiation parameters of the proposed BoCXS, STAR-HE and T-REX, driven by an external laser at the fundamental or second harmonic (SHG). All scattered radiation figures are intended to be on axis ($\theta = 0$), and within the collimation angle, unless the term *total* is specified, indicating an integration of the scattered radiation over the whole solid angle. Question marks underline assumptions for values not available in the literature

	BoCXS (Fund.)	**BoCXS (SHG)**	**STAR-HE (Fund.)**	**T-REX (SHG)**
RF-gun frequency band	C-band		S-band	S-band
Electron Beam at IP				
Bunch charge [nC]	0.5	0.5	0.5	0.5
e-Beam energy [MeV]	145	145	150	116
Norm. proj. emittance, rms [mm mrad]	0.45	0.45	1	6
Bunch duration, FWHM [ps]	7	7	10	20
Transverse beam size, rms [μm]	12	12	20	40
Relative energy spread, rms [%]	0.03	0.03	0.2	0.2
Peak current [A]	70	70	$\sim$40	$\sim$25
Hourglass effect [%]	0.7	0.7	1.0	3.6
Rep. rate [Hz]	100	100	100	10
Incident Laser at IP				
Central wavelength [μm]	1.0	0.5	1.0	0.5
Bandwidth, FWHM [%]	1	1	1?	1?
M^2-factor	1.5	1.5	1.5?	1.5?
Interaction angle [deg]	3	3	5	0
Pulse energy [J]	1.0	0.5	0.5	0.15
Intensity pulse size, rms [μm]	15	15	15?	34
Pulse duration, FWHM [ps]	7	7	10?	20
Diffraction effect	0.4	0.2	0.5	0.1
Rep. rate [Hz]	100	100	100	10
Scattered Radiation				
Collimation angle [mrad]	0.5	0.5	0.5?	0.5?
Pulse duration, FWHM [ps]	2	2	2	12
Source size, rms [μm]	7	7	6	26
Laser-electrons transverse overlap ratio	1.3	1.3	0.9	0.8
Max. photon energy [keV]	382	767	410	478
Bandwidth, FWHM [%]	3	3	6	15
Peak power, *total* [kW]	90	45	23	0.2
Peak intensity [10^6 ph/pulse]	8	2	1.5	0.1
Peak intensity, *total* [10^6 ph/pulse]	260	65	47	3
Peak brilliance [ph/s/mm^2/mrad^2/0.1% BW]	13×10^{19}	4×10^{19}	3×10^{19}	1.5×10^{15}
Average intensity [10^8 ph/s]	8	2	1.5	0.01
Average intensity, *total* [10^8 ph/s]	260	65	47	0.3
Average brilliance [ph/s/mm^2/mrad^2/0.1% BW]	7×10^{10}	2×10^{10}	1×10^{10}	1×10^{6}
Average spectral density [ph/s/0.1%BW]	9.2×10^{6}	2.6×10^{6}	1.2×10^{6}	2×10^{3}
Dimension of e-beam delivery system	$\sim$5m $\times$ 20m	$\sim$5m $\times$ 20m	$\sim$ 5m $\times$ 23m	$\sim$3m $\times$ 25m

3.10 Outlook and future developments

We described the design of a linear electron accelerator and its transport system, enabling simultaneous two-beamline operation of an inverse Compton source. The concept's feasibility was demonstrated through large-scale start-to-end electron-beam dynamics simulations, complemented by the technical details of a state-of-the-art C-band photoinjector, and a novel beam switchyard. Meticulous control of beam optics within the switchyard, balancing chromatic effects while accounting for coherent synchrotron radiation, ensured preservation of the six-dimensional beam brightness.

Thanks to a high-gradient C-band linac and an optimized mirror-based laser arrangement at the interaction points, the proposed ICS source combines a compact footprint with wide photon-energy tunability. These capabilities, together with the predicted ICS performance, make it well suited for high-resolution medical imaging, nondestructive testing in mechanical and automotive industries, and characterization of cultural-heritage artifacts [142]. In the nominal working point—145 MeV beam energy at 100 Hz repetition—the on-axis ICS photon energies are 383 keV at the fundamental laser wavelength ($\lambda_1 = 1032$ nm) and 767 keV via SHG ($\lambda_2 = 516$ nm). By continuously varying the electron energy between 100 and 166 MeV, the on-axis photon energy can be swept from approximately 160 keV up to 1 MeV. Moreover, fine adjustment of the interaction angle permits percent-level spectral scans about these central energies with high spatial coherence, thereby enabling the use of advanced techniques such as rapid K-edge subtraction [35] and phase-contrast imaging [34]. The insertion of the BSM also enables the electron beam to pass through undeflected—either alone or alternating with the X-ray generation—thereby broadening the utility of the ICS facility. A prime example is the FLASH-RT, an emerging technique for ultra-rapid treatment of radiosensitive tumors currently under development in research and clinical settings [143, 144]. The beam's pulse energy and duration align with the specifications for very-high-energy electron (VHEE) linacs central to this technique [145]. Beyond medical applications, the availability of a high-energy electron beam offers potential applications for industrial processes such as materials processing and sterilization.

Future developments will include refinements and improvements upon this work. They will involve electron beam dynamics studies, with the complete inclusion of space charge and short-range wakefield effects, fully simulated from the photocathode up to the interaction point. Also, a more in-depth machine stability study, in particular involving static errors (e.g. misalignment of cavities and magnetic elements) will assess the impact of spurious dispersive effects and transverse wakefield kicks on the beam quality. Then, a complete simulation of the ICS interaction, can fully capture all 3D effects, such as the hourglass effects which, although small, can limit the extent of the interaction region and the effective available X-ray flux. Finally, a complete characterization of the X-ray beam is necessary to accommodate the specific application considered.

Chapter 4

Microbunching instability studies in the context of free-electron laser facilities

With the BoCXS project on hold, we decided to leverage the skills and insights gained during its design and beam-dynamics studies by redirecting my research toward other accelerator platforms, while remaining within the realm of high-brightness electron beam light sources, specifically free-electron lasers (FELs). This refocusing remains fully consistent with the central thread of my dissertation, namely the optimization of six-dimensional electron-beam brightness in linear accelerators for X-ray applications. Following the INFN–LNF and University of Bologna collaboration on the BoCXS C-band photoinjector, I joined the most advanced effort currently underway at LNF: the EuPRAXIA@SPARC_LAB project [52]. This initiative seeks to build the world's first user-oriented, plasma-driven FEL facility, augmented by state-of-the-art linac technology, thereby creating new synergies between fundamental-physics research and high social impact applications.

In such a context, the brightness requirements on the electron beam are even more demanding, as these type of machines routinely employs strong bunch compression during acceleration. Self-developing microstructures in the longitudinal phase space of electron bunches subjected to strong compression have been observed in several high-brightness FEL linac drivers [42, 43]. Consistent with experimental results, computer simulations of the longitudinal space charge (LSC) force [146] and CSR in bunch compressors demonstrate that microbunching instability (MBI) can significantly amplify small initial modulations in longitudinal density and energy, thus degrading beam quality. This effect is particularly disruptive for an FEL, where it leads to a large slice energy spread. For this reason, a proper study of MBI has to be performed in the context of the design and development of EuPRAXIA@SPARC_LAB, on the basis of the final machine layout. Moreover, the possibility to use a laser heater as a MBI suppressor, requires a careful design to accommodate the various machine configurations and working points that are foreseen during the machine operation.

This work was carried out under the supervision and with the support of the FERMI research group at Elettra Sincrotrone Trieste [147], which provided its extensive expertise in this field and graciously hosted me within its research activities throughout my final PhD year. Indeed, this last phase of the project also includes studies of the MBI in the context of FERMI—the world's first seeded free-electron laser and currently the FEL facility with the highest degree of longitudinal coherence [51].

In this chapter, we investigate the microbunching instability in linac-driven free-electron lasers, making use of a semi-analytical model to estimate its impact on the electron beam quality. We discuss the application of such model to develop optimal strategies of beam compression schemes in the context of high-current operations for FERMI. Subsequently, we extend our study to the EuPRAXIA@SPARC_LAB facility, analyzing its specific machine configurations and working points to assess the susceptibility to microbunching-driven beam quality degradation. Finally, we describe the design of a laser heater for EuPRAXIA@SPARC_LAB, engineered to provide the operational flexibility required to remain compatible with all the foreseen machine configurations.

4.1 Semi-analytical model of microbunching instability

Various computational approaches are available for modeling the microbunching instability [98, 128, 148–150]. Particle-in-cell codes and Vlasov solvers deliver detailed, high-fidelity results but require substantial computational resources and careful control of numerical noise. Semi-analytical models, in contrast, need minimal computing effort and are inherently noise-free, though they rely on simplifying assumptions that limit their accuracy. Nonetheless, these models are indispensable for identifying the dominant physical processes, that may differ between different scenarios, playing a central role in predicting the final modulation spectrum and energy spread during facility design, as well as in guiding the optimization of operating or upgrade configurations. Various semi-analytical models of the microbunching instability have been developed over the past two decades, such as the integral linearized Vlasov–Maxwell formalism [151] and the matrix-multiplication technique [152]. After recently conducting a comprehensive comparison of the two aforementioned models [53], for these MBI studies, we adopted the integral linearized Vlasov–Maxwell approach—which for the sake of brevity we will name Huang-Kim (HK) model—for its balance of physical transparency and computational efficiency, and in the following, we detail our implementation.

The HK formalism is grounded on the linearization of the Vlasov-Maxwell equation for the 6D electron beam distribution passing through a four-dipole symmetric chicane [151]. The impedances effects on the formation of microbunches are modeled as an integral equation whose kernel contains the physics of collective effects

$$b(k(s); s) = b_0(k(s); s) + \int_0^s K(s', s) b(k(s'); s')\, ds'. \tag{4.1}$$

with $k = 2\pi/\lambda$ the modulation wave number. The model is valid in ultrarelativistic regime and, in our implementation, averages over betatron oscillations along the linac. The use of effective transverse beam sizes in the calculation of Coulomb interactions justifies 1.5D approximations to some extent [94, 153]. Another underlying assumption is that bunch compression remains linear. This approximation can introduce differences between the model and both simulations and the real case, since strong nonlinearities in the compression process may lead to the formation of pronounced current spikes, which in turn significantly enhance CSR and MBI effects, particularly in high-current regimes.

As shown in Fig 4.1, the beam line is split into straight sections (either a linac or a transfer line, from s_0 to s_1), interspersed with magnetic chicanes (bunch compressor, from s_1 to s_2 for the first half of the chicane, from s_2 to s_3 for the second half) with a linear compression factor C. Starting from a shot noise-like distribution (Eq. 2.88),

$$|b_0(k)| = \sqrt{\frac{ec}{I_0}\frac{k}{2\pi}}, \tag{4.2}$$

the bunching, defined at s_0 ($b(s_0)$), generates energy modulation through LSC up to s_1,

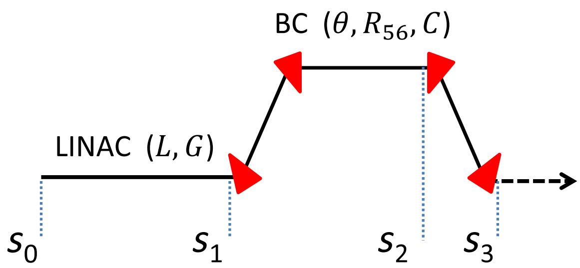

Figure 4.1: Sketch of a beamline consisting of a linac section of length L and average accelerating gradient G, followed by a four-dipole magnetic chicane (bunch compressor, BC) characterized by dipole bending angle θ, longitudinal dispersion function R_{56}, and inducing linear compression by a factor C. This type of beamline can be replicated in a series to model multistage compression [53].

recalling Eq. 2.89

$$\frac{\Delta\gamma}{\gamma}(k,s) = \frac{4\pi I_0}{Z_0 I_A}\int_{s_0}^{s_1} b(k,s')\frac{Z_{\rm LSC}(k,s')}{\gamma(s')}\,ds'\,, \tag{4.3}$$

that is then plugged into the equation to calculate the amplified bunching factor at the end of the bunch compressor s_3 (from Eq. 2.90)

$$b|_{R_{56}}(s_{0\to 3}) \simeq CkR_{56}\frac{\Delta\gamma}{\gamma}\,LD_\perp\,LD_\parallel\,. \tag{4.4}$$

The bunching due to the effects of CSR, $b|_{\rm CSR}(s_{1\to 3})$, is also calculated following strictly [151], and then linearly superimposed to the initial and copropagating bunching $b(s_0)$ (low gain term), and to the LSC-driven bunching (high gain):

$$b(s_3) = b(s_0) + b|_{R_{56}}(s_{0\to 3}) + b|_{\rm CSR}(s_{1\to 3})\,. \tag{4.5}$$

The energy modulation induced by LSC throughout the chicane (from s_1 to s_3) is also calculated, with the peak current assumed to be unperturbed in the first half of the chicane and multiplied by the compression factor in the second half, and finally all energy modulations are linearly superimposed:

$$\frac{\Delta\gamma}{\gamma}(s_3) = \left.\frac{\Delta\gamma}{\gamma}\right|_{\rm LSC}^{0\to 1} + \left.\frac{\Delta\gamma}{\gamma}\right|_{\rm LSC}^{1\to 2} + \left.\frac{\Delta\gamma}{\gamma}\right|_{\rm LSC}^{2\to 3}\,. \tag{4.6}$$

This procedure is repeated for each subsequent section of the machine that involves bunch compression: the final bunching factor given in Eq. 4.5 becomes the initial one for the next compression stage, and the energy modulations generated in the upstream sections are likewise converted into microbunching, together with those cumulated in the new section. The two damping terms of Eq. 4.4 introduce Landau damping similar in form to Eqs. 2.91 and 2.92. According to [151], transverse damping $LD_\perp$ is approximated by keeping only the contribution from the fourth dipole of the chicane, where the bunch is fully compressed, and where the dispersion $\eta_x \to 0$ so that the chromatic H-function $\mathscr{H}_x \simeq \beta_x \eta_x'^2 \simeq \beta_x \theta^2$. Longitudinal Landau damping is instead driven by the uncorrelated energy spread upstream of the chicane. In this implementation of the model, also the effect of intrabeam scattering (IBS) is evaluated stepwise along the beamline. This contribution to the energy spread, in some cases, is crucial to a reliable prediction of the MBI gain and therefore of the final slice energy spread [53, 154]. The IBS-induced relative energy spread is here computed in its energy-dependent integral form as [154, 155]

$$\sigma^2_{\delta,\mathrm{IBS}}(\gamma; s) = \frac{1}{G_a/(mc^2)} \frac{1}{\gamma^2} \int_{\gamma_0}^{\gamma} \tilde{k}(\gamma') \sqrt{\gamma'}\, d\gamma' \,, \tag{4.7}$$

where G_a is the average accelerating gradient in MeV/m and $\tilde{k}(\gamma)$ is given by

$$\tilde{k}(\gamma) \simeq \left(\frac{N_e\, r_e^2}{8\, \varepsilon_n^{3/2}\, \beta_\perp^{1/2}\, \sigma_z} \right) \ln \left(\frac{\beta c \tau\, N_e\, \varepsilon_n^{1/2}}{16\, \gamma^2\, \varepsilon_n^{3/2}\, \beta_\perp^{1/2}\, \sigma_z} \right) \Bigg|_\gamma \,, \tag{4.8}$$

with $r_e = 2.818 \times 10^{-15}$ m the classical electron radius, ε_n the transverse normalized emittance, $\beta_\perp$ the average betatron function, N_e the number of electrons in a bunch of rms duration σ_z, and τ the bunch traveling time at speed βc.

The laser heater is assumed to introduce only uncorrelated energy spread whose contribution can be specified by the user. However, an eventual transverse mismatch between the round laser beam (rms size σ_l) and the round electron beam (rms size σ_e) in the heater undulator can modify the idealized Gaussian energy distribution. Accounting for this effect, Eq. 2.91 is generalized as follows [91]:

$$LD_\parallel(k; s_3) = \exp\left[-\frac{1}{2} (CkR_{56})^2 \sigma^2_{\delta,\mathrm{int}}(s_1) \right] \xi_0(k; \sigma_e, \sigma_l), \tag{4.9}$$

with

$$\xi_0 = \int dR R e^{-\left(\frac{R^2}{2}\right)} J_0 \left[CkR_{56} \sigma_{\delta,\mathrm{LH}} \exp\left(-\left(\frac{R\sigma_e}{2\sigma_l} \right)^2 \right) \right] . \tag{4.10}$$

where J_0 is the zero-order Bessel function. Although negligible (approximately 2 orders of magnitude smaller in a symmetric four-dipole chicane), the second order longitudinal dispersion T_{566} contribution to the damping can be enabled.

In the end the figures of merit we use to measure the presence and magnitude of MBI are the spectral gain

$$G(k) = \left| \frac{b_f(k)}{b_0(k)} \right| , \tag{4.11}$$

and the beam energy spread which is given by

$$\sigma^2_{E,\mathrm{tot}}(s) \cong C^2 \left(\sigma^2_{E,0} + \sigma^2_{\mathrm{LH}} + \sigma^2_{\mathrm{IBS}}(s) \right) + \sigma^2_{\mathrm{MBI}}(s) \equiv \sigma^2_{\mathrm{int}}(s) + \sigma^2_{\mathrm{MBI}}(s) \, , \tag{4.12}$$

where $\sigma_{E,0}$ is the initial uncorrelated energy spread at the photoinjector, σ_{IBS} is the one given by IBS, σ_{MBI} is the energy spread given by the energy modulations cumulated through LSC, σ_{LH} is the energy spread induced by the laser heater and we consider an approximate preservation of the longitudinal emittance through the compression process. The total LSC-induced energy spread is in turn given by the sum in quadrature of all the energy spread contributions, computed with Eq. 2.94, of the various subsequent sections represented in Fig. 4.1.

The HK formalism was successfully benchmarked in [154] to explain the observed $\sim$ 100 keV slice energy spread at the end of the FERMI linac in a low charge regime (100 pC), while here we show in Fig. 4.2 the same exercise for the slice energy spread measured at the same facility in high charge regime (600 pC) [156], where also the Bosch-Kleman-Wu (BKW) approach [152] is shown for comparison [53]. More in detail, the $\sigma_{E,\mathrm{tot}}$ predicted by HK and BKW are compared to the slice energy spread $\sigma_{E,\mathrm{meas}}$ measured at the entrance of the FERMI FEL undulator line, at the energy of 1 GeV, for the three peak currents of 0.8, 1.1, and 1.3 kA (i.e. for compression factors of 11, 15 and 17, considering an initial current of 75 A and an initial energy spread $\sigma_{E,0} = 2.4$ keV) with and without the action of the laser heater. In this specific case the MBI was almost absent, and the use of the LH only increased the final energy spread.

4.2 FERMI FEL @Elettra Sincrotrone Trieste

In an externally seeded free-electron laser, a synchronized laser pulse is injected into a short modulator undulator that is tuned to the fundamental resonance of the electron

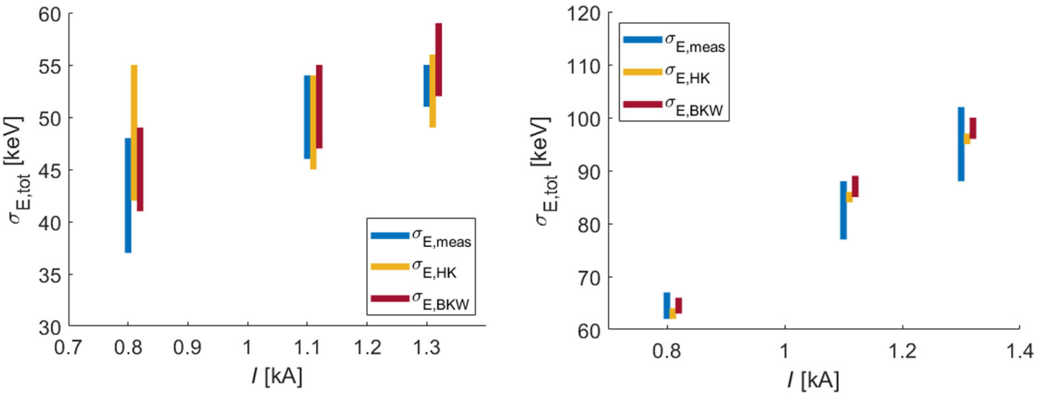

Figure 4.2: Slice energy spread at the entrance of the FERMI undulator line predicted by HK (yellow), BKW (red), and measured [156] (blue), for laser heater off (left) and inducing 5 keV rms energy spread (right). The height of the blue bars corresponds to the experimental uncertainty reported in [156], while the height of the yellow and red bars accounts for peak-to-peak variation of the prediction over three different IBS models [53] and for average betatron functions along the FERMI beamline (scanned in the range of 10–20 m).

beam. The laser field promptly imprints a periodic energy modulation on the electrons, and, as the beam subsequently traverses a magnetic chicane, this energy modulation is converted into a density (current) modulation—or microbunching—at the same spatial period. Because the microbunching is generated deterministically and immediately, the beam enters the next undulator section in the high-gain regime without the stochastic start-up associated with SASE operation. By adjusting the chicane dispersion the microbunching can be shifted to the n-th harmonic of the seed wavelength. The bunched beam is then injected into a radiator undulator tuned to that harmonic; there the coherent radiation intensity grows exponentially over a few gain lengths, producing high-brightness FEL pulses at wavelengths well below the seed, in a process known as high-gain harmonic generation (HGHG) [157, 158]. The output pulse inherits the seed narrow bandwidth and fixed phase, yielding full longitudinal coherence and a nearly transform-limited spectrum—properties that closely resemble those of conventional optical lasers. Moreover, the required undulator length is substantially reduced compared with SASE, making HGHG an efficient route to intense, short-wavelength FEL radiation.

FERMI is a user-oriented, externally seeded, single-pass free-electron laser facility housed within the Elettra synchrotron complex in Trieste [51, 159, 160]. Its principal aim is to provide fully coherent, narrow-bandwidth photon pulses—tunable in wavelength, polarization, and duration down to the femtosecond range—for advanced spectroscopic, diffraction, and pump–probe experiments [161–165]. As of now, FERMI

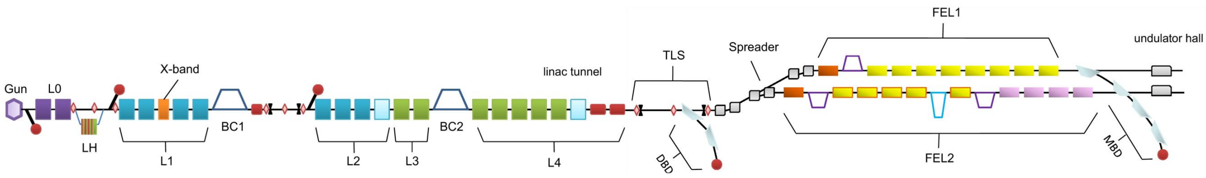

Figure 4.3: Schematic of FERMI layout, comprising of accelerating structures (Gun, L0-L4), compressors (BC1, BC2), high energy transfer line (TLS, Spreader), FEL lines and beam dumps (DBD, MBD) [123].

remains the only FEL facility worldwide that employs external seeding to deliver fully coherent, intense pulses of 10–100 fs duration with unparalleled energy and timing stability [147, 166], while also enabling multi-color FEL operation [167]. Both FEL lines of FERMI employ external UV seed lasers ($\lambda_l \approx 230$–260 nm). In FEL-1, a single-stage HGHG scheme covers wavelengths between 100 nm and 20 nm. FEL-2 adds a fresh-bunch, two-stage HGHG cascade to reach 20 nm down to 4 nm in the soft-X-ray "water window" [168, 169]. FERMI FEL-2 can also be operated in the so-called superradiance mode, allowing to generate transform-limited few-fs pulses. Moreover, the implementation of the echo-enabled harmonic generation (EEHG) scheme in the FEL-1 amplifier line has recently been achieved [170, 171], doubling the maximum photon energy of FEL-1 and enhancing the spectral quality. This external seeding architecture ensures full longitudinal and statistical coherence comparable to conventional lasers—making of FERMI the most coherent FEL in the world—and enables continuous wavelength tuning via simple adjustments of the seed-laser parameters. In the future, upgrades are foreseen as part of the FERMI 2.0 plan [160, 172], involving a substantial increase in the linac energy, an upgrade of the undulators and a conversion from the FEL-2 line HGHG operating scheme to an EEHG first stage, followed by an HGHG second stage, which will allow to reach photon energies well beyond the oxygen K-edge.

The FERMI layout is sketched in Fig. 4.3. The $\sim$ 150 m long, S-band normal conducting linac can provide a beam energy of up to $\sim$ 1.5 GeV. The layout includes a laser heater system (LH) at the exit of the photoinjector L0 (at $\sim$ 100 MeV), a small X-band linearizer and two magnetic chicanes (BC1 and BC2), allowing high current operations up to $\sim$ 1 kA. The transfer line (TLS) and the spreader, made up of two pairs of double bend achromat sections, lead to the single-pass undulator chains for the external laser-seeded FEL-1 and FEL-2.

4.2.1 Microbunching instability studies for FERMI compression schemes

During its latest operations, the FERMI accelerator made use of a one-stage compression scheme to bring electron bunches of ~ 500 pC up to ~ 700 A, proving to be a reliable configuration for the main FEL operations, both in terms of needed beam current and microbunching instability occurrence. In preparation for the FERMI 2.0 upgrade, operation with two-stage compression was studied, aiming at obtaining a final beam current ≥ 1 kA. Two configurations were tested, and both showed a strong content of MBI, making it basically impossible to operate the FEL without a substantial use of the laser heater, as shown in Fig. 4.4. This revealed the need for more in-depth studies of

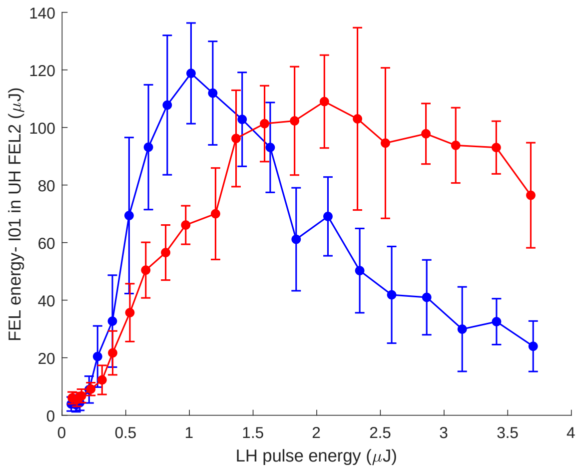

Figure 4.4: Measured FEL intensity versus laser heater attenuator scan, for the two compression scheme tested in November 2024. The configuration 1 (in red) showed a larger MBI content overall, with respect to the configuration 2 (in blue).

the MBI behavior for the various compression schemes, in order to minimize its impact on the FEL performance. The main goal was to use the semi-analytical model to explore the compression parameters space and find the configuration that could minimize MBI contributions in terms of energy and current modulations, to be later tested on the actual machine.

Another option would involve an actual change to the layout of the FERMI 2.0 machine by removing one of the two magnetic compressors and potentially relocating the remaining one to a different position along the accelerator, in order to enable the bunch compression at an optimal anergy to maximize the 6D beam brightness. Therefore, also this eventuality was studied by making use of the HK model.

An important note to make is that these studies consider the buildup of the MBI only up to the end of the linac, right before the spreader entrance. It is likely, however, that the action of the double bend achromat sections has a considerable impact on the instability, contributing both with longitudinal dispersion and CSR effects which, in particular, may become dominant when such high beam currents are involved. Hence, while the extension of the analytical model to the spreader is deferred to a future work, our aim here was to keep the MBI as low as possible at the linac's end, so as to minimize any possible amplification of the instability through the spreader.

4.2.1.1 Two-stage compression scheme

The two compression schemes tested during the FERMI operation in November 2024 involved the use of both magnetic bunch compressors BC1 and BC2, with compression factors and longitudinal dispersions expressed in Tab. 4.1. At the exit of the photoin-

Table 4.1: Two-stage compression parameters for two configuration tested at FERMI

Parameter	**Config. 1**	**Config. 2**
BC1 compression factor, C_1	~ 3.5	~ 4.2
BC2 compression factor, C_2	~ 5.0	~ 4.2
BC1 longitudinal dispersion, $R56_1$ [mm]	-41	-23
BC2 longitudinal dispersion, $R56_2$ [mm]	-23	-23

jector, the beam starts with a current of 57 A, a bunch charge of 500 pC, and an initial energy spread of ~ 2 keV, and is subsequently accelerated to 1.5 GeV and compressed to reach a final current of about 1 kA. We reproduced the two schemes implementing the HK model, which, in its current instance, is able to describe the MBI evolution along the machine, up to the end of the linac. The results, shown in Fig. 4.5 are compatible with the measurements obtained by observing the FEL intensity, i.e. both configurations present a high content of MBI, with the first one representing the worst case, as more LH energy is required to suppress the instability (see Fig. 4.4, same color scheme is used for the two configurations). Next, we had to probe the multidimensional parameter space of the machine for the two-stage compression scenario, with the goal to find a configuration that minimizes the MBI. To do so, we performed scans of the main parameters of the two bunch compressors, namely C_1, C_2, $R56_1$, and $R56_2$, aiming at a total compression factor $C_{tot} = 17.6$. More in detail, we studied specific scenarios represented by different compression ratios between BC1 and BC2: $C_1 > C_2$ ($C_1 = 6.5$, $C_2 = 2.7$), $C_1 = C_2$ ($C_{1,2} = 4.2$) and $C_1 < C_2$ ($C_1 = 2.7$, $C_2 = 6.5$). For each scenario

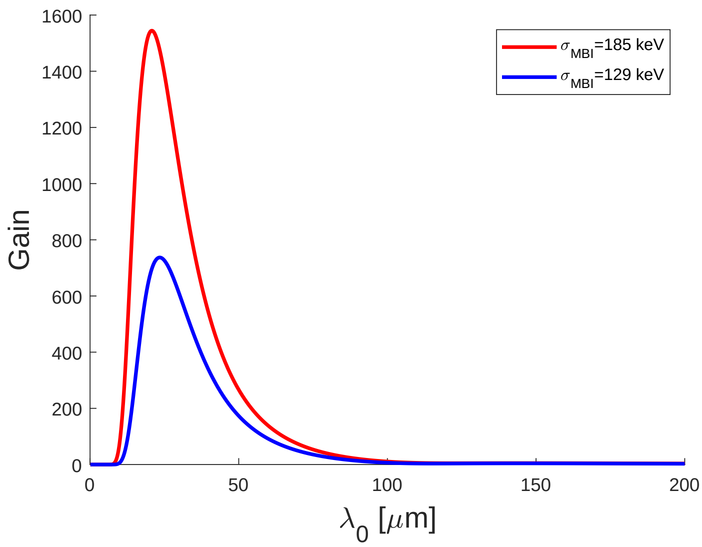

Figure 4.5: Gain functions for the config. 1 (in red) and config. 2 (in blue) and corresponding MBI-induced energy spreads (σ_{MBI})

we scanned $R56_2$ considering three different values of $R56_1$. The results are shown in Figs. 4.6 and 4.7, displaying a multivariate 4D visualization of the parameter space on a 2D plot, where the x-axis represents $R56_2$, the color encodes $R56_1$ and the line style indicates the compression ratio between BC1 and BC2. From Fig. 4.6, it is clear

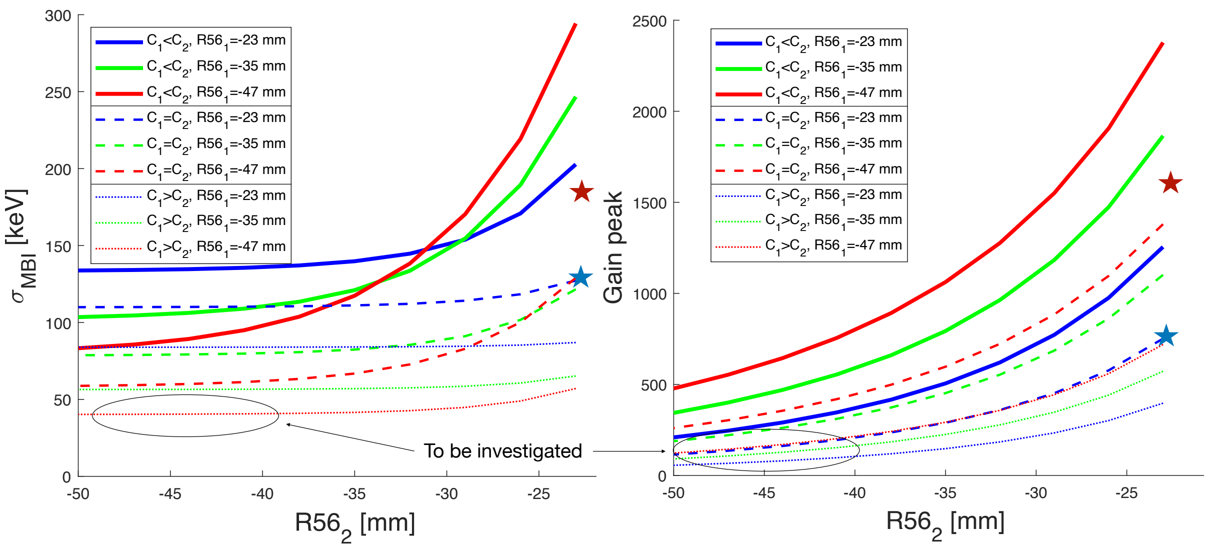

Figure 4.6: Multidimensional scan of the two-stage compression scheme, for a total bunch compression $C_{tot} = 17.6$. On the left, MBI-induced energy spread. On the right, maximum of the gain function. The red and blue stars represents the config. 1 and 2 respectively. The parameter space volume to be investigated is represented by the case $C_1 > C_2$ and $R56_{1,2} < -40$ mm.

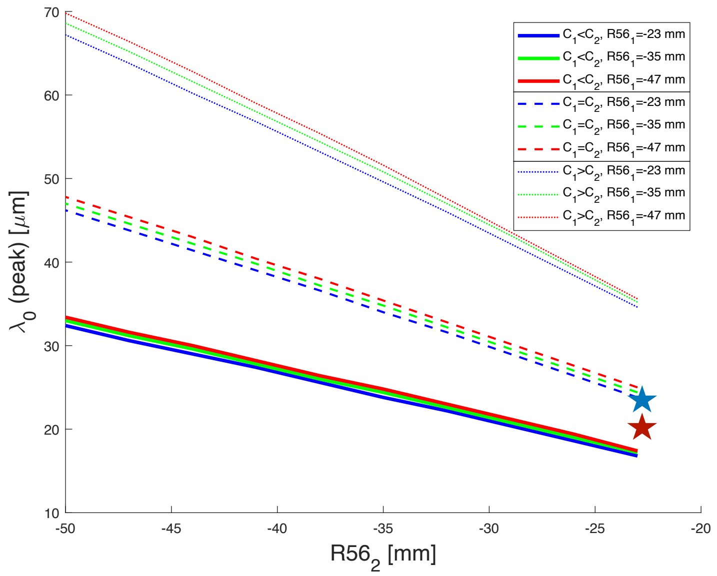

Figure 4.7: Multidimensional scan of the two-stage compression scheme, for a total bunch compression $C_{tot} = 17.6$. Wavelength (uncompressed) of gain peak. The red and blue stars represents the config. 1 and 2 respectively.

that larger compression ratio C_1/C_2 and $|R56_2|$ minimize both the gain and the energy spread. The dependence of MBI on $R56_1$ is, instead, more intricate: while the gain is generally minimized for smaller $|R56_1|$, the energy spread shows opposite behaviors above or below specific values of $|R56_2|$, and the point of behavioral inversion depends on C_1/C_2. Finally, Fig. 4.7 shows that larger C_1/C_2 and $|R56_2|$ bring the gain peak to longer wavelengths, while only a weak dependence on $R56_1$ is expected. For the FERMI operation, a promising parameter space volume was individuated, represented by the configuration $C_1 > C_2$ and $R56_2 < -40$ mm, which in a realistic scenario also requires $R56_1 < -40$ mm, to be compatible with the needed beam energy chirp at BC2. During the next FERMI run, at the end of 2025, this configuration will be deeply investigated and tested.

4.2.1.2 One-stage compression scheme

The option to operate the machine with a single bunch compressor by removing completely the other magnetic chicane opens to the possibility to upgrade the FERMI machine layout with the implementation of an additional accelerating section, which would allow for greater energy flexibility. This also entails the possibility of relocating the remaining chicane to a different position along the accelerator, with the goal of potentially improving the overall beam brightness. Indeed, performing the beam compression at higher energies should mitigate the impact of CSR in the chicane, as the beam becomes more resilient to such collective effects. The behavior of the MBI, however, is less trivial and needed to be investigated. We therefore studied the impact of the MBI in the one-stage compression scenario, by performing a scan of the BC position along the accelerator, which translates to a scan of the bunch compression energy. Using the HK model, we scanned the BC energy between 285 and 770 MeV, which roughly correspond to the current positions of BC1 and BC2, respectively. The results are shown in Figs. 4.8 and 4.9 displaying the spectral gain and MBI-induced energy spread at the linac end for two values of the chicane's R_{56}. The spectral gain

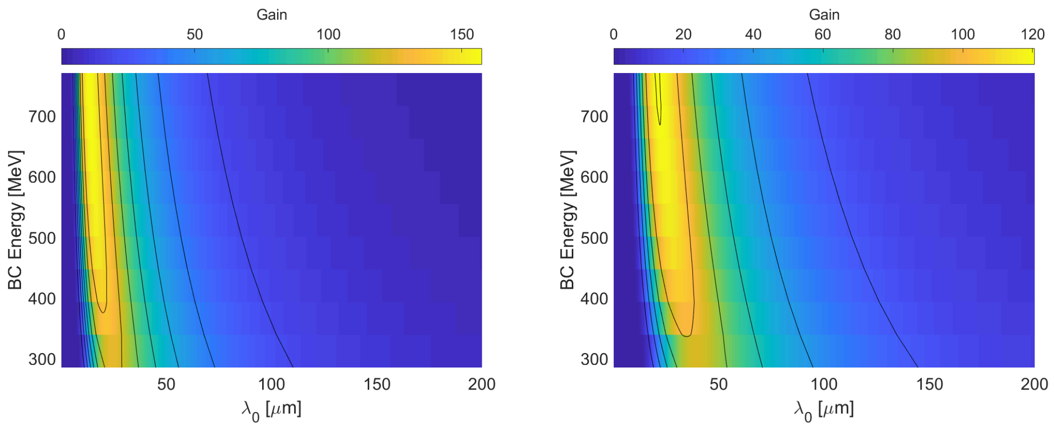

Figure 4.8: Spectral gain as a function of compression energy and uncompressed wavelength λ_0, for $R_{56} = -30$ mm (on the left) and $R_{56} = -50$ mm (on the right).

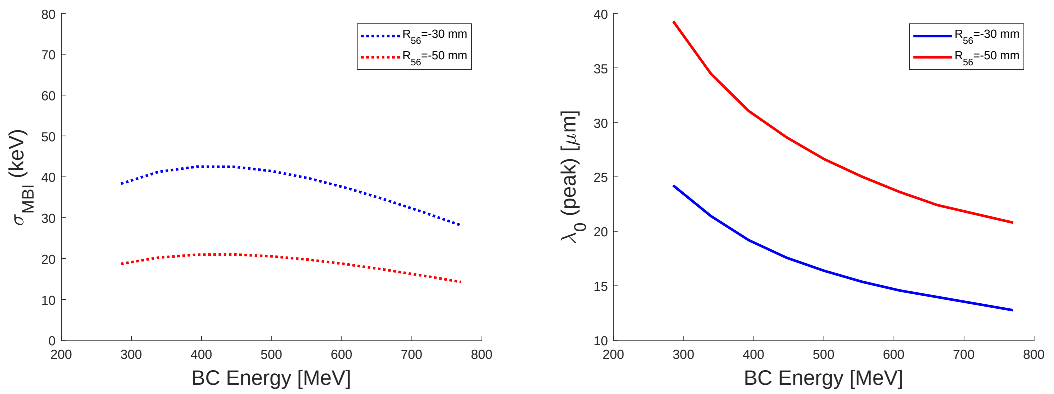

Figure 4.9: MBI-induced energy spread (left) and wavelength of the gain peak (right) vs compression energy, for two values of R_{56}.

exhibits a monotonic increase with the BC energy, as expected, given that a further downstream compression allows larger energy modulations to develop and be converted into microbunching. Such increment, is of the order of 20–30 % between the minimum and the maximum BC energy, since most of the energy modulation upstream the compression develops in the early stages of acceleration. Larger BC energies also move the gain peak to shorter wavelengths. The MBI-induced energy spread, displays a weak dependence on the BC position (Fig. 4.9, left), which becomes even weaker with higher values of $|R_{56}|$. As shown in Fig. 4.10, we also tested the sensitivity of this compression scheme to the use of the LH, for various positions of the BC, since at shorter wavelengths the longitudinal Landau damping should be more effective. However, although the gain

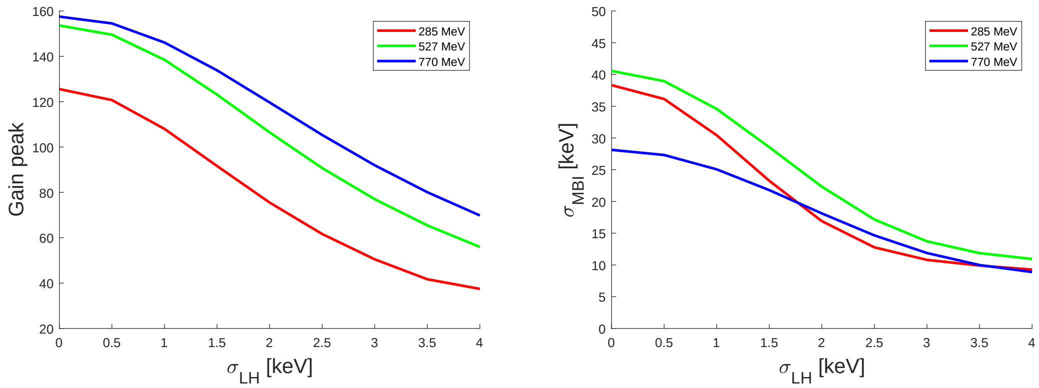

Figure 4.10: Scan of LH-induced energy spread for three values of BC energy. On the left: spectral gain. On the right: MBI-induced energy spread.

peak wavelength is shorter, at higher BC energies also the relative energy spread σ_δ is smaller, and the two effects tend to compensate each other (with a slight edge in favor of lower BC energies).

In general we observed that the overall content of MBI is not greatly affected by the position of the BC, but a larger $|R_{56}|$ helps to suppress the instability. Hence, we could not find a clear ideal scheme in terms of BC position to minimize the MBI, as we did for the two-stage compression scenario, and the eventual choice of the optimal BC location must be determined by other, more impactful, discriminating factors. For example, as previously stated, a higher BC energy could be beneficial, as it reduces the CSR-induced horizontal emittance growth; however, this may entail some complications. Moving the bunch compression further along the beamline requires a greater effort to linearize the longitudinal phase space distribution with the X-band cavity, since the bunch length would be larger (thus more sensitive to the RF field curvature) for a greater part of the acceleration. In addition, this may expose the beam to a larger transverse wakefield instability along the beamline upstream the compression. Finally, a "delayed" bunch compression may leave too little room to correct the residual linear energy chirp.

In conclusion, this remains an open possibility for the FERMI 2.0 upgrade, which have to be further investigated, possibly with an actual machine experiment. Indeed, with the current FERMI layout we can probe the two cases representing the minimum and maximum BC energy by operating the machine with either only BC1 or BC2, respectively.

4.2.2 Outlook and future developments

The results presented in this section provide a comprehensive overview of the expected behavior of the microbunching instability for the different compression strategies under consideration for the FERMI accelerator. The combination of experimental observations and semi-analytical modeling has allowed for a deeper understanding of the mechanisms driving the instability growth and their dependence on the compression parameters. For the two-stage compression case, the model reproduced well the experimental evidence collected during FEL operation, confirming the strong presence of MBI in both configurations tested. The parametric exploration of the compression settings revealed clear trends, and identified a promising region of operation to be experimentally tested during the upcoming FERMI run. Conversely, the analysis of the single-stage compression scheme showed a weaker sensitivity of the MBI to the bunch compressor position along the accelerator.

In summary, these studies establish a solid groundwork for the optimization of the FERMI 2.0 compression schemes. They emphasize the importance of a global approach that simultaneously accounts for compression efficiency, collective effects, and practical machine limitations. The next step will be the experimental validation of the most promising configurations and the extension of the model to include the downstream sections of the accelerator, where the combined action of the spreader optics and CSR may further influence the evolution of the instability.

4.3 EuPRAXIA@SPARC_LAB

Plasma-based acceleration [173–177] exploits the ability of an ionized gas to sustain extremely large electric fields—several orders of magnitude above those achievable in conventional RF structures. When a short, intense driver (either an ultra-short laser pulse or a high-current particle bunch) traverses the plasma, it displaces electrons from its path and excites a trailing plasma wave or "wake". The electric fields inside this wake can reach the GV/m level and, if a properly phased witness bunch is injected into the accelerating phase of the wave, it can gain energy very rapidly over just a few centimeters. Since the driver transfers its energy directly to the plasma wave, which in turn accelerates the electrons, plasma accelerators offer the prospect of ultra-compact, high-energy linacs—potentially reducing facility length from hundreds of meters to just a few meters—while preserving beam quality suitable for advanced light sources and high-energy physics applications.

EuPRAXIA@SPARC_LAB is the INFN–LNF implementation of the European Plasma Research Accelerator with eXcellence In Applications (EuPRAXIA) design study, whose primary objective is to demonstrate the viability of plasma-based acceleration for next-generation user facilities [178]. Hosted at the Frascati National Laboratories, the project aims to integrate a high-brightness electron beam produced by a novel X-band RF linac, together with a PW-range laser system enabling both laser- and beam-driven plasma wakefield acceleration to feed a compact free-electron laser beamline operating initially in the water-window spectral region (2–5 nm) with user-oriented endstations [52].

The unique feature of EuPRAXIA@SPARC_LAB is its status as the first user-oriented FEL facility driven, in whole or in part, by plasma acceleration. In its baseline plasma-driven configuration, a 1 GeV beam, pre-accelerated to $\sim$ 600 MeV in the X-band linac and then boosted by a plasma module, will drive a SASE FEL capable of delivering ultra-short ($\sim$ fs), high-brilliance pulses. The facility footprint is kept around $\sim$ 100 m by virtue of X-band state of the art technology and the GV/m-scale gradients provided by plasma wakefield acceleration. The final design will support two beamlines, including VUV (50–180 nm), XUV/soft-X-ray (2–10 nm) FEL branches and a betatron source from laser-plasma interaction [179].

In its current layout, EuPRAXIA@SPARC_LAB facility spans a 55 m accelerator

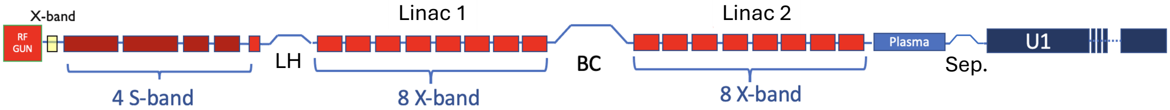

Figure 4.11: Schematic of the EuPRAXIA@SPARC_LAB accelerator layout, inclusive of the AQUA beamline.

complex that delivers a high-brightness ~ 1 GeV electron beam. The layout, as sketched in Fig. 4.11, comprises an S-band photoinjector, involving a small X-band linearizing cavity right after the gun. A first magnetic chicane hosts the laser heater (LH), but is also used as bunch length compressor, necessary to shorten the bunch before the injection into the X-band linac. The two X-band sections are interleaved by the main magnetic bunch compressor (BC), and are followed by the plasma module. After that, a small magnetic chicane is implemented in order to separate and dispose of the driver, which lost most of its energy inside the plasma to accelerate the witness. The diagnostic and matching sections then prepare the beam for either the AQUA or ARIA (not shown) undulator beamline. The AQUA undulator hall itself houses a 25 m long undulator line (for SASE), succeeded by a 12 m photon-diagnostics and transport section that guides the FEL radiation into the users' experimental hall. The ARIA beamline requires fewer undulators to operate, since the seeded VUV ARIA FEL line exploits the standard HGHG.

4.3.1 Microbunching instability studies for EuPRAXIA@SPARC_LAB configurations

The HK model was used to investigate the expected impact of the MBI on the electron beam quality for the different machine modalities of EuPRAXIA@SPARC_LAB. This work was carried out with the aim of complementing the start-to-end simulations performed by the beam dynamics group of SPARC_LAB, in the context of the Technical Design Report of EuPRAXIA@SPARC_LAB. The cases discussed here, focus on the configurations and working points currently characterized for the AQUA beamline, which include two configurations involving plasma acceleration, one with velocity bunching (COMB beam scheme) and one with two-stage magnetic compression (mask scheme), while the third one covers the full-RF scenario.

For all the configurations discussed here, the initial beam uncorrelated energy spread at the gun is assumed to be ~ 2 keV and the initial peak current ~ 60–70 A. Unless specified, all the results presented here are obtained with the laser heater switched off. It is also worth to mention that, while the spectral gain is normalized to the initial bunching factor, thus independent of its value, the σ_{MBI} scales linearly with b_0, here assumed to have a shot noise distribution with values in the range $10^{-4} - 10^{-3}$ within the bandwidth of interest (condition of ideal uniformity of the photocathode laser pulse). Therefore, the estimates of the energy spread given here have to be considered as references, since photocathode laser irregularities larger than b_0, at critical wavelengths, or a smaller initial slice energy spread may cause larger instabilities.

4.3.1.1 COMB beam configuration for plasma acceleration

In the COMB beam configuration, both driver and witness bunches are produced in the photoinjector within a single RF bucket by combining the laser-comb technique (a train of temporally spaced laser pulses illuminating the photocathode) with RF velocity bunching. In this scheme, the witness laser pulse impinges on the cathode about 5 ps before the driver one and, as the beam undergoes velocity bunching, their temporal ordering is inverted, effectively rotating its longitudinal phase space. For this scheme, various working points are foreseen, including few with high charge beam: up to 400 pC for the driver and 50 pC for the witness. An optimized working point for the high charge case, simulated by the LNF beam dynamics group [180], can be seen in Fig. 4.12. Bunch length compression occurs in the injector's early stages through velocity bunching (roughly by a factor 30 for the witness and 25 for the driver), justifying the assumption that the bunch is already fully compressed throughout acceleration in the S-band section. By assigning 50 pC to the witness and 400 pC to the driver, we intentionally model a worst-case scenario for microbunching instability. Since no dispersive elements are present before the plasma entrance, the spectral gain at that point is unity for both bunches, and no amplification of initial current modulations is expected. We furthermore evaluate the energy spread at the plasma entrance point, which may be detrimental to the beam focusing, necessary for a proper matching to the plasma. It should be noted that the semi-analytical model provides an estimate of the slice energy spread via the induced energy modulations under the condition $l_{bunch} \gg l_{slice} \gg \lambda$. However, in the witness case the bunch length (on the order of microns) becomes comparable to both the FEL cooperation length, i.e. the slice length

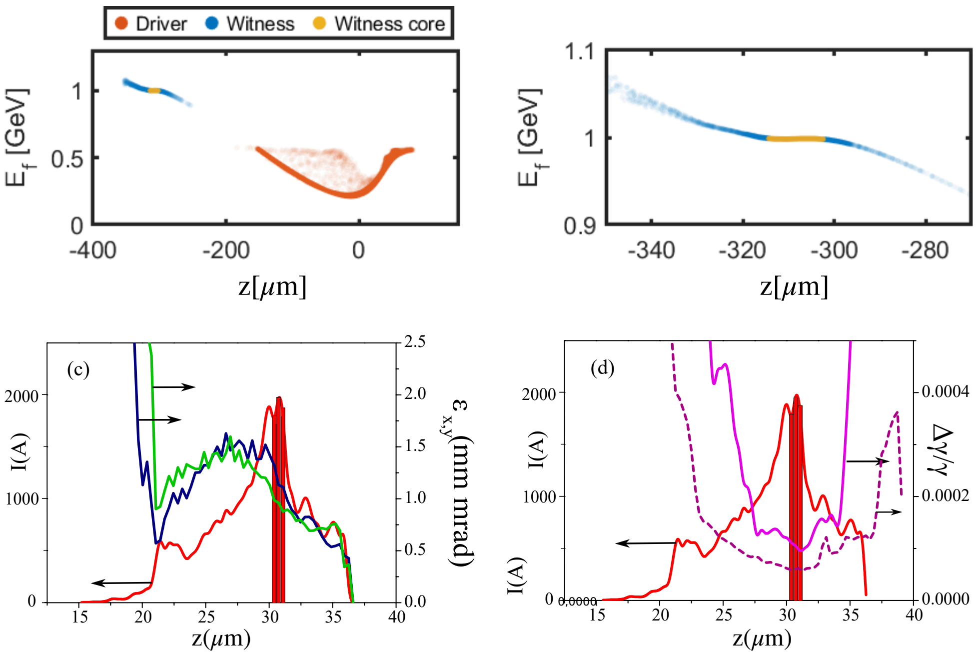

Figure 4.12: On the top: longitudinal phase space of the COMB beam configuration after the plasma module. On the bottom: slice analysis of the witness bunch at the undulator entrance, for the whole beam (solid line) and with a cut of 3 % of charge (dotted line), the best slice is indicated by red columns(the head of the bunch is on the right of the plots) [180].

(hundreds of nanometers), and the peak spectral modulation wavelength. Under these circumstances, the energy modulation may manifest as a nonlinear chirp in the witness longitudinal phase space, yet effectively behaving as a projected, uncorrelated energy spread of a single slice in the undulator. This regime approaches the validity limits of the semi-analytical model and therefore would require complementary start-to-end simulations of MBI (inclusive of IBS effects) for a more accurate assessment, which is deferred to future work. The semi-analytical model predicts that, at the plasma entrance, a relative energy spread of approximately 0.01 % for both the witness and driver bunches. Downstream, at the entrance of the undulator, the witness exhibits moderate current modulations, which originated in the separation chicane, as evidenced by the spectral gain profile in Fig. 4.13. The final relative energy spread ($\sim 0.01\,\%$) remains below the Pierce parameter ($\rho_{\rm fel} \sim 0.1\,\%$), suggesting that such amount of MBI is still manageable for SASE FEL operation. Nevertheless, attention should be payed to minimize laser–cathode profile irregularities—particularly at spatial wavelengths near 20–30 μm—as such imperfections can seed additional microbunching growth. Beside that, in this configuration, the use of the laser heater is inadvisable, as it would neces-

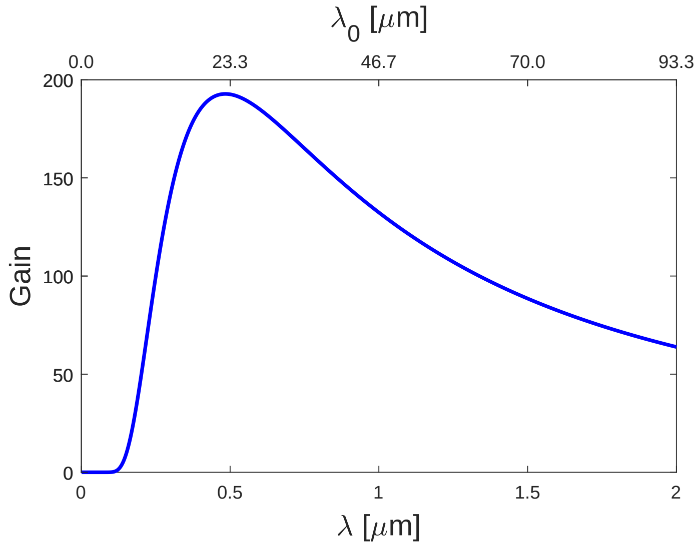

Figure 4.13: Spectral gain of the witness (50 pC) at the entrance of the undulators, for the full-velocity bunching configuration. λ_0 and λ are the initial and compressed wavelength respectively.

sitate routing the beam through the LH chicane, thereby imposing further compression after velocity bunching. Furthermore, even at the smallest achievable deflection angles of the LH chicane, the R_{56} and compression factor of the separation chicane remain too low to enable effective Landau damping. Finally, to introduce a set amount of relative increment of energy spread on a beam already compressed by a factor C, the required laser peak power scales as $P_{\mathrm{LH}} \propto C^2$, making laser-heater operation highly inefficient in this regime.

4.3.1.2 Mask configuration for plasma acceleration

The other possible scheme to exploit the plasma acceleration envisages an ordinary single laser pulse at the cathode, to generate a single electron bunch, subjected to on-crest acceleration and featuring two-stage compression, the first in the LH chicane and the second in BC. Inside the BC, this scheme involves the use of a beam scraper (mask) necessary to divide the beam in two bunches (witness and driver). As of now, this configuration is still not fully characterized, but a preliminary working point can be seen in Fig. 4.14 [180].

The same study was therefore performed for the “mask” configuration. In this case, the witness and the driver, i.e. the tail and the core of the beam, experience strongly

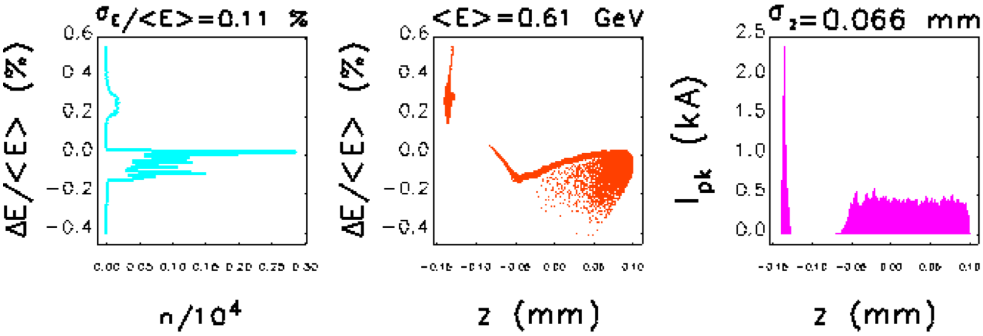

Figure 4.14: Energy distribution (left), longitudinal phase space (center) and current profile (right), of witness and driver after the cut with the mask scraper [180].

different compressions (due to the use of sextupoles to tune the second order momentum compaction T_{566} contribution in the chicanes), requiring them to be studied individually. For the driver (bunch core), we consider a charge of 230 pC and linear compression factors of ~ 2.9 and ~ 2.5 in the LH and BC chicane, respectively. This results in a large spectral gain at the plasma entrance, as shown in Fig. 4.15 (left), in the λ_0 range of 10–20 μm corresponding to a compressed wavelength $\lambda \sim 2$–3 μm. However, at this

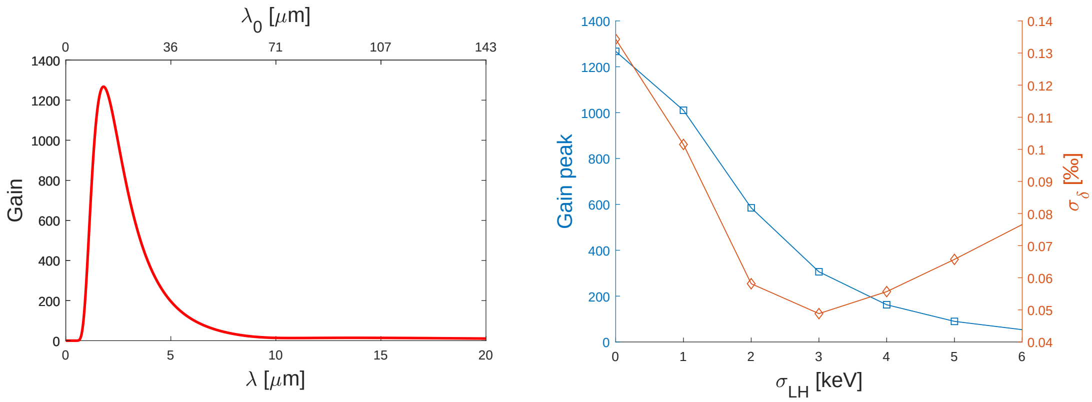

Figure 4.15: Left: spectral gain of the driver (230 pC) at the entrance of the plasma, for the mask configuration (two-stage magnetic compression). λ_0 and λ are the initial and compressed wavelength respectively. Right: peak spectral gain and respective σ_δ as a function of the energy spread induced by the LH.

wavelength, the MBI should not affect the plasma wakefield acceleration mechanism, and the corresponding energy spread is $\sim 0.01\,\%$, not representing an issue for the beam optics. Nevertheless, if necessary, the use of the laser heater can suppress the MBI just by inducing few keV of uncorrelated energy spread, as show in Fig. 4.15 (right).

We consider 30 pC for the witness, and linear compression factors of ~ 2.9 and ~ 35

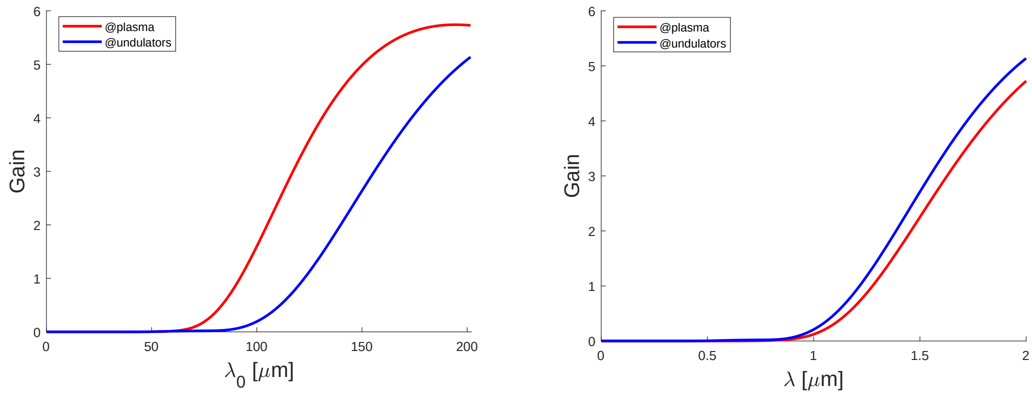

Figure 4.16: Spectral gain of the witness (30 pC) as a function of initial wavelength λ_0 (left) and compressed wavelength λ (right), at the entrance of the plasma (red) and at the undulators (blue), for the mask configuration (two-stage magnetic compression).

in the LH and BC chicane, respectively. As shown in Fig. 4.16, in this configuration we do not expect a large MBI content for the witness, yielding an energy spread of $\sim 0.03\,\% < \rho_{\text{fel}}$ both at the plasma entrance and at the undulators. Moreover for the witness case, the the intrinsic energy spread is strongly dominating ($\sigma_{\text{int}} \gg \sigma_{\text{MBI}}$), due to the strong compression, making any contribution of the LH detrimental.

4.3.1.3 Full-RF configuration

The full-RF scheme is studied to provide a secondary option to the EuPRAXIA@SPARC_LAB operation, without involving the plasma section, thus making use only of the X-band RF acceleration. An optimized working point for the high charge case, simulated by the LNF beam dynamics group [180], can be seen in Fig. 4.17.

As in the mask configuration, the beam undergoes two-stage magnetic compression—first in the LH chicane and subsequently in the BC chicane. However, with no plasma acceleration or beam-separation module required, the separation chicane remains disabled. For this study we assume a 250 pC bunch, compressed by a factor ~ 3.9 in the LH chicane and ~ 6.5 in the BC chicane. As illustrated in Fig. 4.18 (left), the resulting spectral gain peaks for initial modulation wavelengths λ_0 between 20 μm and 30 μm, corresponding to a compressed wavelength $\lambda \sim 1$ μm, and produces a final relative energy spread $\sigma_\delta < 0.01\,\%$. Although the LH could, in principle, be employed to attenuate spectral gain, in this specific case the intrinsic energy spread σ_{int} dominates, and introducing any additional LH contribution would only result in an increment of the final energy spread, as depicted in Fig. 4.18, (right).

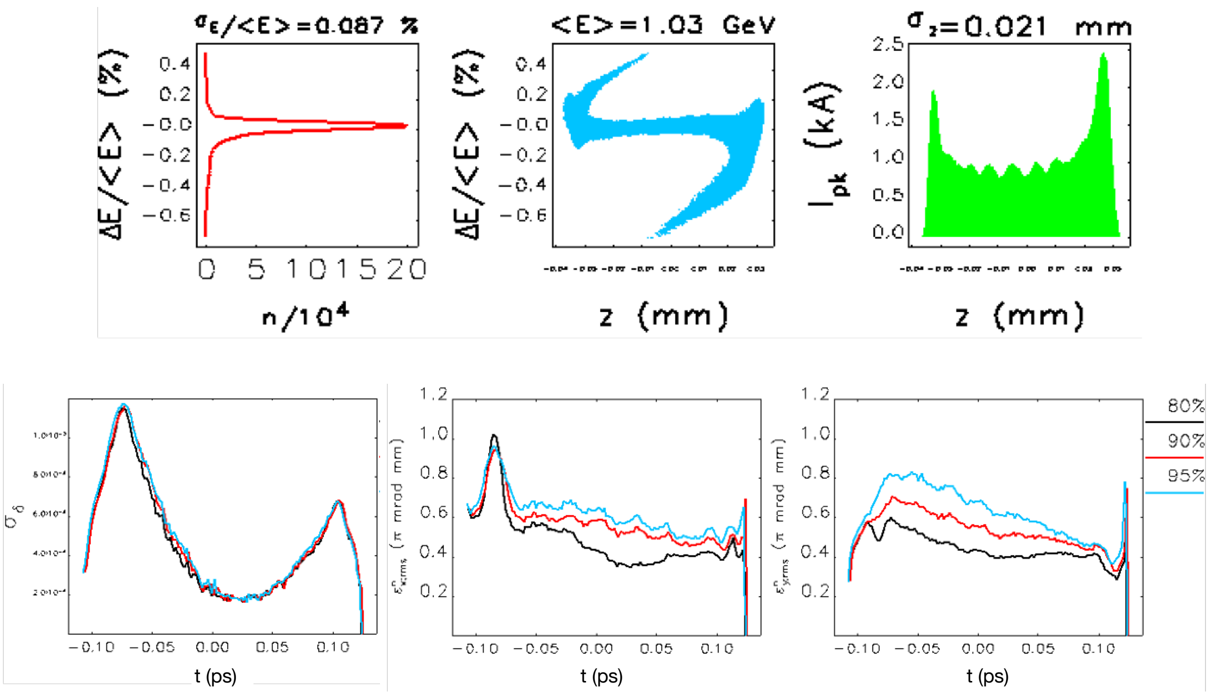

Figure 4.17: Optimized working point for the full-RF case (at undulator entrance). On the top: energy distribution (left), longitudinal phase space (center) and current profile (right). On the bottom: beam slice analysis [180].

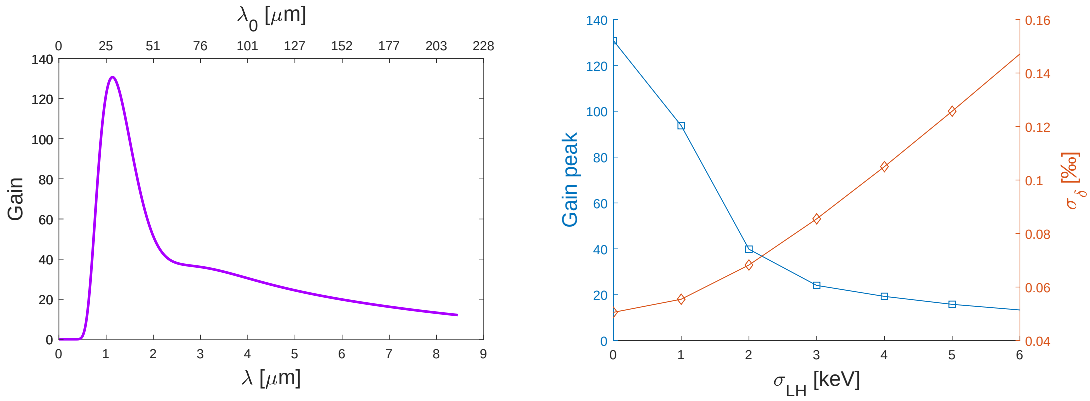

Figure 4.18: Left: spectral gain for the full-RF configuration (250 pC). λ_0 and λ are the initial and compressed wavelength respectively (two-stage magnetic compression). Right: peak spectral gain and respective σ_δ as a function of the energy spread induced by the LH.

The results for the various configurations and the corresponding machine parameters are collected in Tab.4.2.

Table 4.2: Main machine parameters and expected slice energy spread in the considered EuPRAXIA@SPARC_LAB configurations.

Parameter	COMB		Mask		Full-RF
Beam energy @LH (MeV)	100		270		250
Beam energy @BC (MeV)	330		400		670
Beam energy @Plasma (MeV)	560		600		-
Beam final energy (GeV)	1.0		1.0		1.1
LC chicane R_{56}, T_{566} (mm)	-		-60.0, 59.0		-60.5, 59.7
BC chicane R_{56}, T_{566} (mm)	-		-25.0, 24.0		-25.0, 24.0
Sep. chicane R_{56}, T_{566} (mm)	-1.0, 1.5		-1.0, 1.5		-
	witness	driver	witness	driver	-
Q (pC)	50	400	30	230	250
σ_δ @Plasma (‰)	0.1	0.1	0.3	0.1	-
σ_δ @Undulator (‰)	0.1	-	0.3	-	< 0.1

4.3.2 Laser Heater design for EuPRAXIA@SPARC_LAB

The laser heater (LH) is a device that can be used to deliberately increase the uncorrelated energy spread of the electron beam before the instability builds up, harnessing longitudinal Landau damping of the MBI. The concept was first introduced by Saldin et al. [181] and its usefulness first proven at the LCLS hard-X-ray FEL, where the use of the LH shortened the FEL gain length and boosted the photon flux [99]. Such device consists of an undulator operating as a modulator, and a laser which, interacting with the electron beam along the undulator, causes an energy modulation within the bunch, similarly to the seeding process for a seeded FEL, but on the scale of the optical wavelength. The modulator is usually placed in middle of a magnetic chicane, for an easier laser insertion, at the exit of the photoinjector, where the electron energy is usually not larger than few hundreds of MeV. The corresponding energy modulation is typically on the order of few keV to tens of keV. The coherent energy–position correlation is then smeared by the action of the second half of the chicane mainly through transverse Landau damping. The smearing becomes effective when the electrons' phase shift is larger than the laser wavelength λ_l (or $2\lambda_l$ for safer operation)

$$\sqrt{\langle \Delta z^2 \rangle} = 2\pi \sqrt{(R_{51}\sigma_x)^2 + (R_{52}\sigma_{x'})^2 + (R_{56}\sigma_\delta)^2} \geq 2\lambda_l \,, \tag{4.13}$$

where R_{ij} are the transport matrix elements, and the term $R_{52}\sigma_{x'}$ usually is the dominant one, as for a typical four-dipole C-shape chicane $R_{51} = 0$ and $R_{52} = \eta_x$, while

$\sigma_\delta < 10^{-4}$.

The design of the EuPRAXIA@SPARC_LAB laser heater system has been carefully studied with the non-trivial goal of allowing maximum flexibility and accommodate all possible machine configurations. In the following, we discuss the LH main specifications, following a theoretical approach, without any aim of high-level engineering tolerances, but rather searching for the most crucial requirements for the EuPRAXIA@SPARC_LAB layout and operations. All of the analytical expressions applied in this section are well known in the literature and have been extensively benchmarked against both experimental measurements and specialized simulation codes [99, 182].

Laser

The laser is spilled out from the Ti:Sapphire system that also drives the photocathode; this branch is extracted upstream of third-harmonic generation to preserve access to both the fundamental ($\lambda_l \approx 800$ nm) and its second harmonic ($\lambda_l \approx 400$ nm). This, in particular, ensures the spectral flexibility necessary to accommodate electron beam energies from approximately 100 MeV (velocity bunching) to 290 MeV (on-crest acceleration), while supporting adjustable chicane deflection angles. The option to freely adjust the dispersive section translates to a variability of the horizontal electron beam spot size in the undulator, which approaches the value of ~ 1 mm for the larger chicane bending angles. Therefore, an independent laser focusing system for the vertical and horizontal planes is necessary to minimize the required laser power. A pair of orthogonally mounted cylindrical lenses (or, at high fluence, cylindrical mirrors) allows independent adjustment of the vertical and horizontal waists without introducing significant aberrations. Each LH pulse is specified to deliver up to ~ 50 μJ in ~ 10 ps FWHM, providing a maximum laser peak power of ~ 5 MW. A polarization-based variable attenuator provides continuous control over the laser pulse energy, while a high-speed mechanical shutter enables complete beam extinction. The system also incorporates two imaging screen stations for precise spatial overlap of the laser and electron beams, alongside two beam-position monitors (BPMs) that deliver real-time measurements of the electron beam's transverse position and angle.

Undulator

The planar undulator comprises $N_u = 10$ magnetic periods of $\lambda_u = 45$ mm realized with permanent magnets of remanent field $B_r = 1.2$ T, covering a total length of $L_u = 0.45$ m. Its gap is motorized and remotely controlled to vary between 15 mm and 35 mm, providing continuous adjustment of the undulator parameter K. In combination with the selection of either the fundamental or second harmonic laser wavelength, this tunable gap ensures resonant interaction over the full designed electron energy range, as shown in Fig. 4.19. With the defined undulator design, in Fig. 4.20 we plot the required

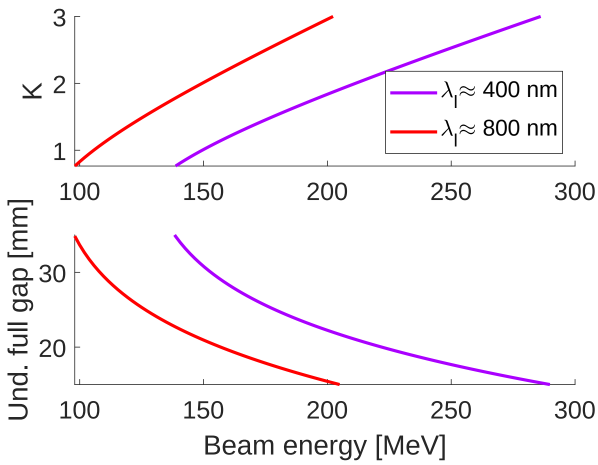

Figure 4.19: Undulator parameter (top) and corresponding full gap (bottom) in the resonant condition. The two laser wavelengths ensure the whole coverage of the electron beam energy range within the full gap range of 15–35 mm.

laser peak power which can be derived as [99]

$$P_l = P_0 \left(\frac{\gamma \cdot \sigma_{\mathrm{LH}}}{mc^2 \cdot JJ \cdot K} \right)^2 \Big/ \int_0^{L_u} \frac{dz}{\sqrt{\sigma_e(z)^2 + \sigma_L(z)^2}} \,, \tag{4.14}$$

where m is the mass of the electron, σ_e and σ_L are the rms transverse sizes of the electron and of the laser beam, respectively, $P_0 = 8.9$ GW, σ_{LH} is the LH-induced energy spread, JJ is the coupling coefficient, defined as the difference of Bessel functions of the first kind [183]

$$JJ = J_0(\xi) - J_1(\xi) \,, \quad \text{with} \quad \xi = \frac{K^2}{4 + 2K^2} \,. \tag{4.15}$$

This formulation accounts for the transverse oscillatory motion of the electrons within the undulator field. The same formula has been used to generate Fig. 4.21 depicting the

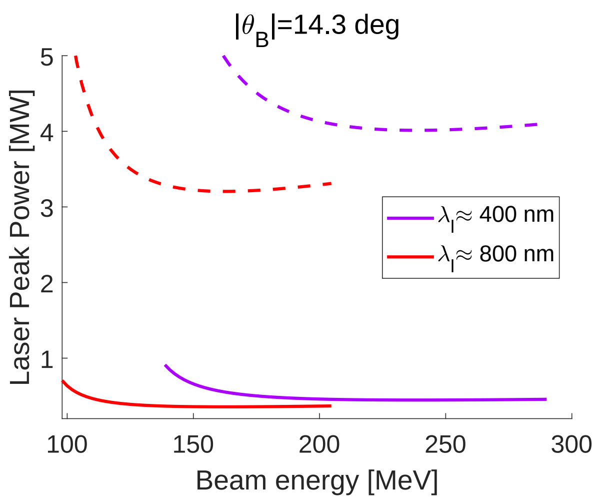

Figure 4.20: Laser peak power needed to induce $\sigma_{\mathrm{LH}_{max}} = 30$ keV (dashed lines) and $\sigma_{\mathrm{LH}} = 10$ keV (solid lines), within the allowed range of undulator full gap and laser energy, in resonant condition, for a chicane deflecting angle $|\theta_B| = 14.3\ deg$.

laser peak power behavior with respect to the LH-induced energy spread, and bending angle $|\theta_B|$, as the required laser horizontal size in the undulator grows with the local dispersion $\eta_x \propto |\theta_B|$. Finally, Fig. 4.22 shows the theoretical behavior of the induced

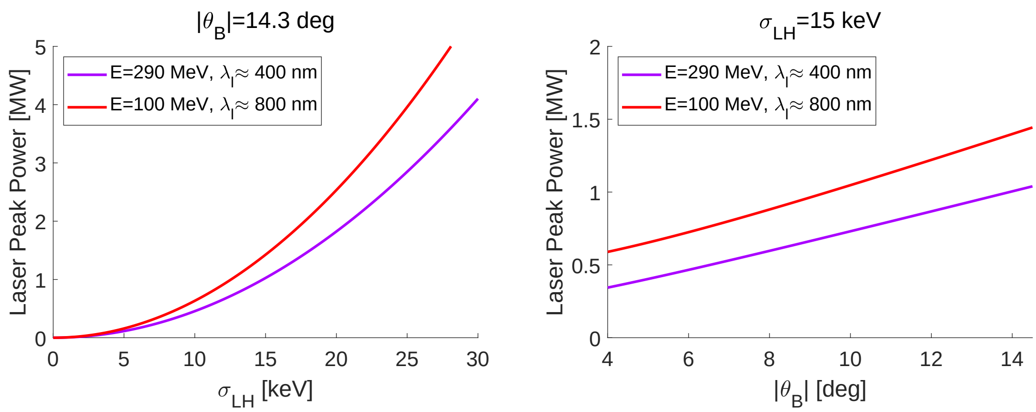

Figure 4.21: Laser peak power for both ends of the electron beam energy range: on the left, plotted vs σ_{LH}, for a chicane deflecting angle $|\theta_B| = 14.3\ deg$; on the right, plotted vs $|\theta_B|$, for $\sigma_{\mathrm{LH}} = 15$ keV.

energy spread as a function of the gap g, that is proportional to the sinc function of the detuning between the laser wavelength λ_l and the undulator resonance wavelength λ_r

$$\sigma_{\mathrm{LH}}(g) = \hat{\sigma}_{\mathrm{LH}} \cdot \mathrm{sinc}\left[\frac{\pi N_u(\lambda_r(g) - \lambda_l)}{\lambda_l}\right], \tag{4.16}$$

with $\hat{\sigma}_{\rm LH}$ being the induced energy spread for a perfectly tuned undulator ($\lambda_r = \lambda_l$), while λ_r is given by

$$\lambda_r(g) = \frac{\lambda_u}{2\gamma^2}\left(1 + \frac{K(g)^2}{2} + \gamma^2\sigma_{x'}^2 + \gamma^2\sigma_{y'}^2\right), \tag{4.17}$$

where $\sigma_{x'}$ and $\sigma_{y'}$ are the electrons rms horizontal and vertical angular divergence.

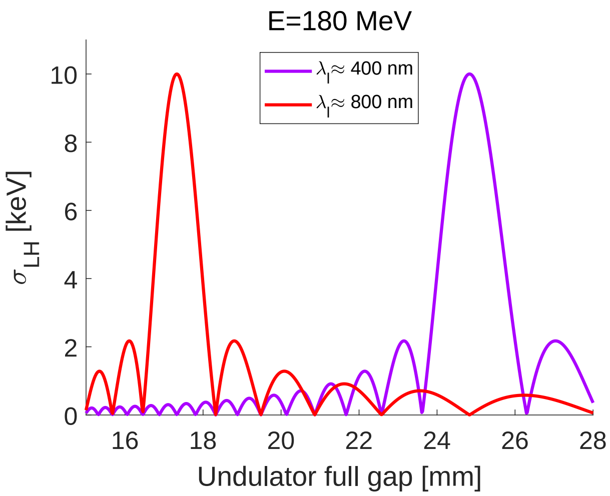

Figure 4.22: Induced slice energy spread by the LH vs undulator full gap with $\hat{\sigma}_{\rm LH} = 10$ keV, for the two possible laser wavelengths, in the case of an electron beam energy of 180 MeV.

Chicane

The LH system layout is sketched in Fig. 4.23. The LH magnetic chicane is designed to operate with variable deflection angles, adjustable between 4 and 14.5 *deg*. This is required to satisfy all the possible bunch compression schemes of EuPRAXIA@SPARC_LAB, since the LH chicane is also used as a bunch compressor. The vacuum chamber can be designed with a fixed profile hosting the whole lateral excursion range of the electron beam. It therefore provides an internal horizontal width of at least 155 mm, leaving clearance on either side of the beam, and at most 13 mm of external vertical width at the undulator location to accommodate the minimum undulator full gap of 15 mm. Since the electron trajectory shifts with the dipoles varying bending angle, the undulator and laser optics and diagnostic have to be mounted on a common transverse translation stage, that can move in a range of about 110 mm. Opting for a rectangular shape of the vacuum chamber, rather than a trapezoidal one, allows minimal-size optical windows—for the laser entrance and exit—about 110 mm wide. Moreover, this also

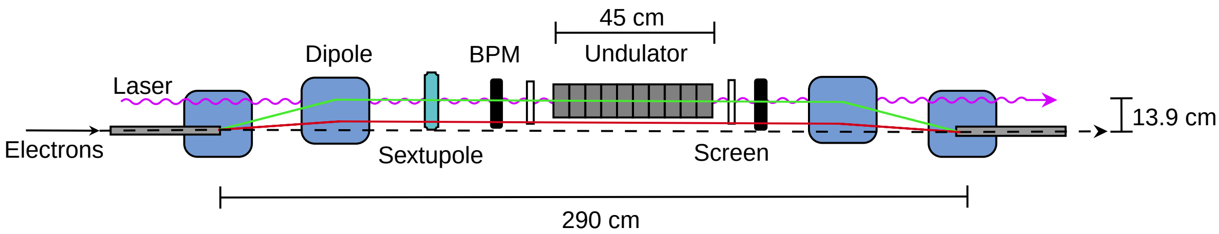

Figure 4.23: Schematic of the LH chicane of EuPRAXIA@SPARC_LAB. The dashed line represents the electron beam trajectory when the chicane is disabled. The red and green lines indicate the trajectory for the smallest and largest dipole bending angles respectively. The undulator and the laser optics have to be mounted on a common transverse translation stage to accommodate the electron beam trajectory.

minimizes the laser incident angle on the windows, thus avoiding laser total internal reflection issues. This design, however, requires a complex engineering of the sextupole present in the chicane, in order to be compatible with an horizontally enlarged chamber. An alternative design option for the laser-heater chicane is to mount the entire pipe vacuum chamber, on the translation stage, thereby allowing it to move jointly with all chicane components, thus preserving the relative alignment of every element while maintaining a compact internal aperture.

Effects on the electron beam

These LH parameters are specified to ensure an increase of the slice energy spread of the electron bunch by up to $\sigma_{\mathrm{LH}_{max}} = 30$ keV, fully covering both electrons energy and bending angle ranges. Moreover, by choosing small values for the latter, for example $|\theta_B| = 4\ deg$, one could reach up to $\sigma_{\mathrm{LH}_{max}} \sim 50$ keV. This upper bound for the energy spread provides a generous tuning margin for an effective Landau damping of the microbunching instabilities. The horizontal emittance growth caused by the particles' energy change in the undulator dispersive region, is induced by the interaction with the laser beam, and can be estimated, assuming the pessimistic case of a full chromatic filamentation of the transverse phase space, as

$$\frac{\Delta\varepsilon_x}{\varepsilon_x} = \sqrt{1 + \frac{\gamma_x \eta_x^2 \sigma_{\mathrm{LH}}^2}{\varepsilon_x E^2}} - 1\,, \tag{4.18}$$

where $\gamma_x = (1+\alpha_x^2)/\beta_x$ is the Twiss parameter defined at the undulator location and E is the electron beam energy. For the foreseen configurations, the expected emittance growth induced by the LH remains below 15 %. The main LH specifications are collected in Tab. 4.3.

Table 4.3: Laser heater main specifications

Laser	**Value**
Wavelength, λ_l [nm]	400, 800
Pulse duration, FWHM [ps]	≤ 10
Pulse energy [μJ]	≤ 50
Peak power. P_l [MW]	≤ 5
Undulator	
Permanent magnets remanent field, B_r [T]	1.2
Period length, λ_u [mm]	45
Number of periods, N_u	10
Undulator parameter, K	0.8–3.0
Undulator full gap, g [mm]	15–35
Electron beam	
e-beam energy, E [MeV]	100–290
Horizontal e-beam spot size in the undulator, σ_x [mm]	0.2–0.8
Vertical e-beam spot size in the undulator, σ_y [mm]	< 0.1
Electron beam duration, FWHM [ps]	< 5
LH-induced maximum slice energy spread, $\sigma_{\mathrm{LH}_{max}}$ [keV]	30–50
LH-induced horizontal emittance growth, $\Delta\varepsilon_x/\varepsilon_x$ [%]	< 15
LH Chicane	
LH Chicane bending angle, $\|\theta_B\|$ [deg]	4–14.5
Horizontal offset in the chicane [mm]	39–139
Vacuum chamber external vert. width [mm]	≤ 13

4.3.3 Outlook and future developments

The studies performed for EuPRAXIA@SPARC_LAB have provided a detailed understanding of the expected microbunching instability behavior across the different operating configurations of the facility. The analysis, based on the Huang–Kim semi-analytical model, showed that the MBI remains within acceptable limits for all baseline working points, including the plasma-driven COMB and mask schemes, as well as the full-RF configuration. In particular, while some degree of current and energy modulation is expected in the two-stage compression schemes, the induced energy spread consistently remains below the FEL Pierce parameter, ensuring compatibility with SASE operation in the AQUA beamline.

Particular attention was devoted to the design of the laser heater system, which departs from conventional implementations by offering wide operational flexibility. Unlike standard fixed-geometry setups, the EuPRAXIA@SPARC_LAB laser heater can accommodate large variations in both beam energy (100–290 MeV) and chicane bending angle (4–14.5 deg), while maintaining resonance conditions by virtue of its tunable undulator gap and dual-wavelength laser configuration. This adaptability makes it suitable for all the foreseen compression schemes—velocity bunching and two-stage magnetic compression—without requiring hardware reconfiguration.

Overall, these findings validate the robustness of the planned accelerator layout in terms of MBI control and beam quality preservation, establishing a solid foundation for the forthcoming commissioning phase and for future refinements of the plasma-driven FEL concept.

Future work will strengthen the present analysis through extensive numerical simulations aimed at capturing the full range of physical effects contributing to the microbunching instability, in particular coherent synchrotron radiation effects, which can become dominant in high current regimes.

A dedicated effort will also be devoted to investigating the influence of the driver beam's microbunching on the generation and stability of the plasma wakefield, as well as its possible impact on the acceleration dynamics of the witness beam. Understanding the interplay between driver's modulations and plasma wake formation will be essential to ensure stable acceleration and to preserve the high beam brightness required for FEL operation.

Chapter 5

Conclusions

The studies presented in this thesis addressed the generation and preservation of high-brightness electron beams for advanced radiation sources, spanning from compact inverse Compton facilities to FEL and plasma-driven accelerators. Despite the diversity of these systems, a common objective guided the work: understanding and controlling the physical mechanisms that limit beam brightness, in order to improve the efficiency, flexibility, and performance of next-generation light sources.

In the first part, the design and beam dynamics studies for the BoCXS inverse Compton source demonstrated the feasibility of delivering high-quality electron beams within a compact layout, while ensuring stability against realistic jitters and dispersion effects. In particular, we obtained 500 pC beams from the C-band photoinjector with normalized transverse emittance <0.5 mm mrad and relative energy spread $<0.3\,\%$ by optimizing the gun and traveling-wave cavity phases. These beam parameters are preserved along the line through fine tuning of the betatron and chromatic motions, and are further improved by the X-band harmonic linearizer, which reduces the projected energy spread by approximately one order of magnitude and enables clean transport through the doglegs while preserving the current profile. A functional element of the layout is the fast switchyard implemented via the bunch selection module, which provides per-bunch routing and thus allows quasi-simultaneous operation of multiple beamlines with a configurable duty cycle. Finally, analytical estimates of the inverse-Compton source performance indicate photon-beam figures of merit comparable to or better than those of other single-pass ICS facilities, and confirm a tunable X-ray energy range from about 100 keV up to 1 MeV. This tunability is enabled by the energy flexibility of the linac, combined to the use of second-harmonic generation of the interaction laser, and the dedicated design of the optical box. These results contribute to defining design criteria for future ICS facilities capable of tunable, high-flux X-ray generation within reduced footprints.

The second part focused on the onset and mitigation of the microbunching instability in high-current linacs. A semi-analytical model based on the Huang–Kim formalism was applied to study the evolution of the instability along realistic schemes, with particular reference to FERMI and EuPRAXIA@SPARC_LAB. This approach provided a fast and physically transparent tool to evaluate the effect of compression parameters and to identify regimes where MBI growth can be minimized without compromising beam current or FEL performance.

On FERMI, we applied the semi-analytical model to compression studies along the linac to identify configurations that minimize microbunching build-up. The analysis covered both one-stage and two-stage compression, with the goal of analytically screening the most promising scenarios for machine operations in view of the FERMI 2.0 upgrade. Within this framework, the model isolated a two-stage configuration that minimizes microbunching instability, and which represents a candidate for validation on the actual machine.

For EuPRAXIA@SPARC_LAB, the study focused on characterizing several machine configurations and working points in terms of susceptibility to microbunching instability. Three configurations were examined, evaluating the instability at the plasma entrance and at the undulator, and the results indicate that the machine can mitigate these effects within the considered parameter space. This capability is further supported by the use of a laser heater to enhance longitudinal Landau damping. In this context, we also proposed a laser heater design engineered for broad operational compatibility across a wide range of beam energies (100–290 MeV) and chicane bend angles (4–14.5 deg)—a key requirement for a facility combining multiple acceleration and compression modes.

Overall, the work highlights the importance of integrating analytical models, numerical simulations, and design optimization in the study of high-brightness beam physics. Although the physical scales and technologies differ across the considered facilities, taken together, these results yield transferable design rules and reproducible methodology, through the control of phase-space correlations, the mitigation of collective instabilities, and the preservation of brightness through compression and transport.

Appendix A

Suppression of dispersive contribution to projected emittance through optical balancing

In the BSM, the vertical dipole kicker and downstream off-axis quadrupole together form a small vertical dogleg that inherently generates non-correctable vertical dispersion. By applying a tailored matching of the beam into this section, we nevertheless suppress the resulting growth in vertical projected emittance to a negligible level. To illustrate this mechanism, we consider the simpler case of an horizontal dogleg composed by two identical rectangular dipoles, with no quadrupole elements between them, as depicted in Figure A.1.

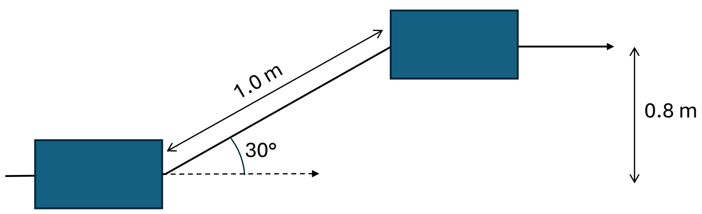

Figure A.1: Sketch of an horizontal dogleg. No quadrupoles are present to correct the dispersion [112].

The rms emittance is given by:

$$\varepsilon_x = \sqrt{\sigma_x^2 \sigma_{x'}^2 - \sigma_{xx'}^2}\,, \tag{A.1}$$

where, in a dispersive region

$$\begin{aligned}\sigma_x &= \sqrt{\varepsilon_{x0}\beta_x + \eta_x^2\sigma_\delta^2}\,,\\ \sigma_{x'} &= \sqrt{\varepsilon_{x0}\gamma_x + \eta_x'^2\sigma_\delta^2}\,,\\ \sigma_{xx'} &= -\varepsilon_{x0}\alpha_x + \eta_x\eta_x'\sigma_\delta^2\,.\end{aligned} \tag{A.2}$$

Here β_x, γ_x and α_x are the Twiss parameters, ε_{x0} is the achromatic (betatron) emittance (i.e. without dispersive contribution), while η_x and η_x' are the dispersion function and its derivative respectively. The relative increment of emittance due to the dispersion contribution is given by:

$$\frac{\Delta\varepsilon_x}{\varepsilon_{x0}} = \sqrt{1 + \frac{\mathscr{H}_x\sigma_\delta^2}{\varepsilon_{x0}}} - 1, \tag{A.3}$$

where $\mathscr{H}_x$ is the chromatic H-function, representing the dispersive contribution to the emittance, for which we recall the definition:

$$\mathscr{H}_x = \gamma_x\eta_x^2 + 2\alpha_x\eta_x\eta_x' + \beta_x\eta_x'^2. \tag{A.4}$$

As shown in Fig. A.2, the dispersion function at the exit of the second dipole is $\eta_x = -0.84$ m, and its first derivative $\eta_x' = 0$, similarly to the case of the first half of a four-dipole, C-shape chicane. Here, Eq. A.4 reduces to $\mathscr{H}_x = \gamma_x\eta_x^2$. Accordingly,

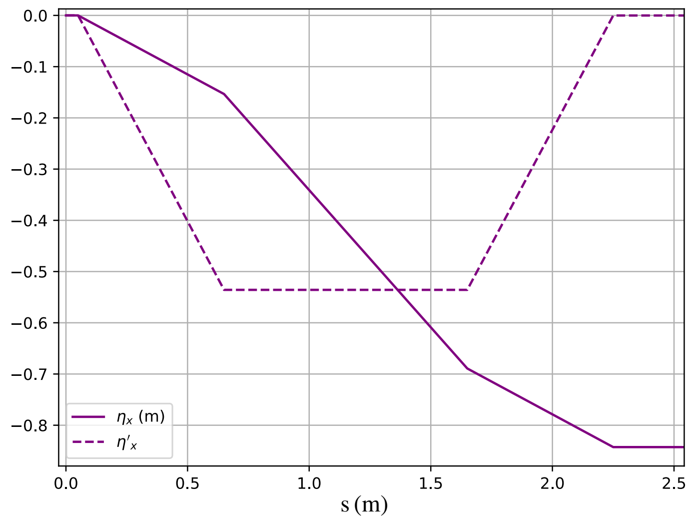

Figure A.2: Dispersion functions along the dogleg [112].

the dispersion-induced emittance growth is minimized when the beam divergence at the dogleg exit is kept small. In our configuration, the Twiss parameter γ_x remains constant throughout the dogleg, allowing an upstream matching section to set the optic parameters that minimize emittance growth at the dogleg exit.

Figure A.3, obtained from a simulation in ELEGANT, shows as an example the emittance evolution along the dogleg for two different matching conditions of a test beam with $\varepsilon_{nx} = 0.4$ mm mrad, $\sigma_\delta = 0.3 \cdot 10^{-3}$ and with an energy of 145 MeV (basically the nominal beam parameters of BoCXS). The optimized matching condition (in red) given for $\gamma_x = 6.7 \cdot 10^{-3}$ m^{-1} results in a relative increment of emittance of about 0.14, while the unoptimized one (in blue), for $\gamma_x = 22.6$ m^{-1}, gives a increment of about 30.64. A more intuitive way to capture this mechanism can be given by looking at

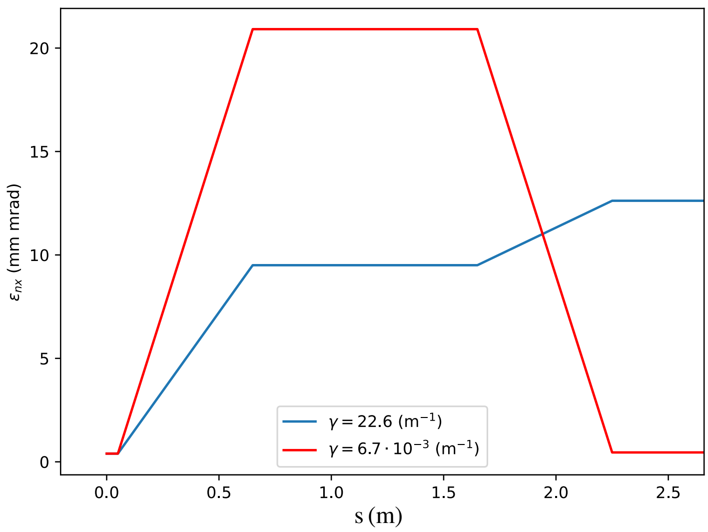

Figure A.3: Emittance evolution of a test beam through the dogleg for two different matching conditions [112].

the phase space evolution along the dogleg, for the two different matching conditions, shown in Fig. A.4. There, we can see that the net effect of this dogleg is a smearing of the particles' horizontal position distribution, implying that a smaller beam divergence will minimize the final phase space area. This clearly shows how impactful is the design of a proper matching on the final projected emittance.

In the BSM case, although slightly more complex due to the double action of the off-axis quadrupole (bending and focusing), the same principle applies. When the vertical beam trajectory is corrected by the off-axis passage through the quadrupole, the H-function can be strongly suppressed, provided the beam is properly matched. Therefore, the addition of a matching section before the BSM is an essential requirement in the

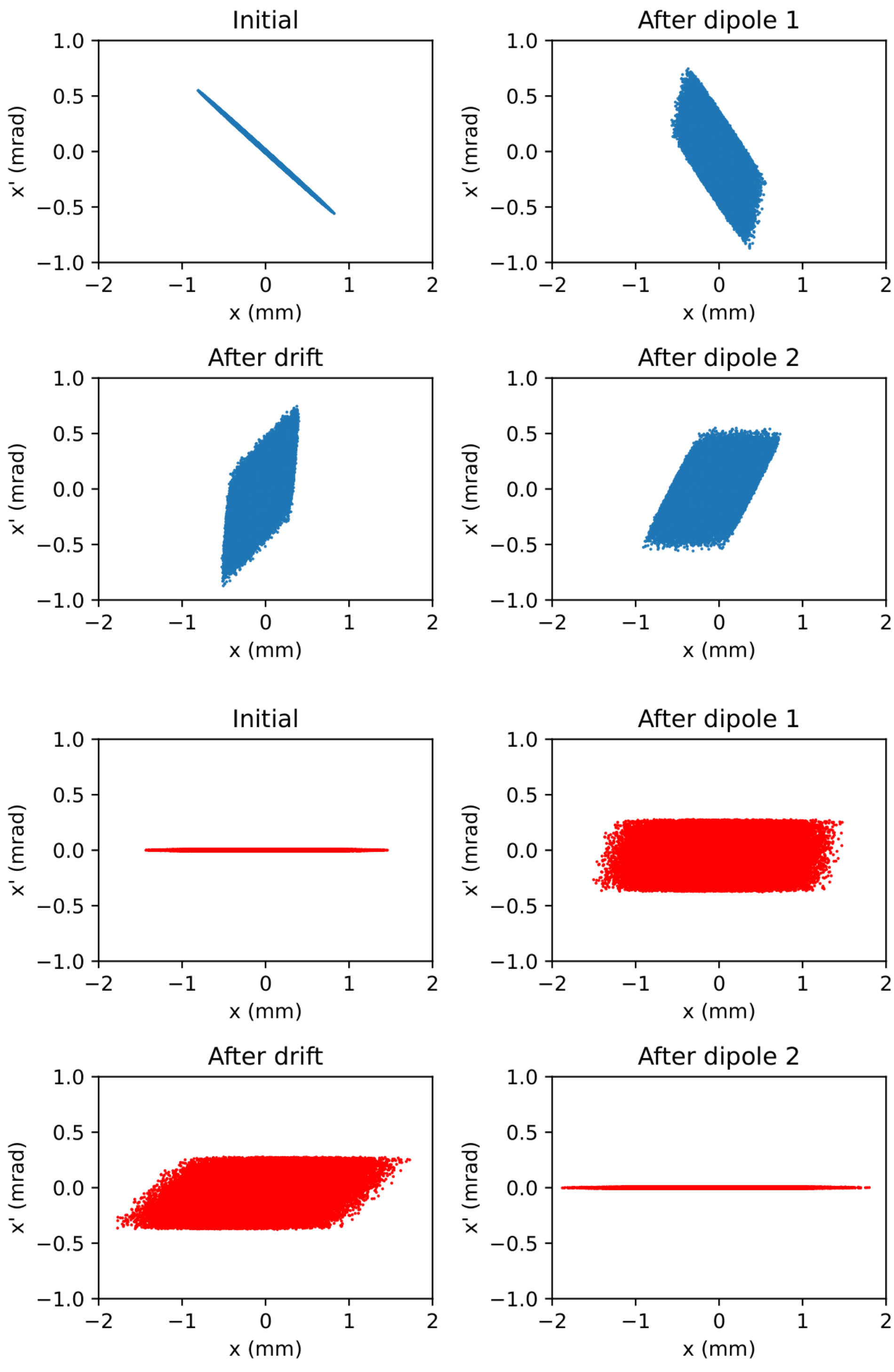

Figure A.4: Phase space evolution through the dogleg for the two different optical matching conditions: with $\gamma_x = 22.6\ \mathrm{m}^{-1}$ (in blue) and $\gamma_x = 6.7 \cdot 10^{-3}\ \mathrm{m}^{-1}$ (in red).

machine layout. Once minimized at the BSM exit, the chromatic H-function, being an invariant, remains constant along the rest of the beamline and finally, at the IP, the residual vertical dispersion is brought to zero to remove the dispersion contribution to the beam size and any energy-position correlation.

Appendix B

ICS analytical model

The time-averaged total ICS flux, in units of photons per second, is [107]:

$$\bar{I}_\gamma = \sigma_C \frac{N_e N_l f}{A_\varphi} \,. \tag{B.1}$$

The number of scattered photons per pulse is therefore $I_\gamma = \bar{I}_\gamma / f$, where N_e is the number of electrons in a bunch colliding with the number N_l of photons in the laser pulse, at the interaction frequency f, across an effective interaction area:

$$A_\varphi = 2\pi \Sigma_y \sqrt{\Sigma_x^2 + \Sigma_z^2 \tan^2(\varphi/2)} \,. \tag{B.2}$$

The convoluted electron beam and laser pulse sizes are:

$$\Sigma_u = \sqrt{\sigma_{e,u}^2 + \sigma_{l,u}^2} \,, \qquad u = x, y, z \,. \tag{B.3}$$

The total unpolarized Compton scattering cross section is related to the Thomson cross section through the recoil parameter X [107, 184]:

$$\sigma_C = \sigma_T \frac{3}{4X} \left[\left(1 - \frac{4}{X} - \frac{8}{X^2} \right) \ln(1 + X) + \frac{1}{2} + \frac{8}{X} - \frac{1}{2(1 + X^2)} \right] \,, \tag{B.4}$$

where

$$\sigma_T = \frac{8\pi}{3} r_e^2 \,, \quad X = 2\gamma^2 [1 + \cos(\varphi)] \frac{E_l}{E_e} \,,$$

and we introduced the classical electron radius r_e, the laser photon energy E_l, and the electron total energy E_e.

The average total flux within the user-defined collimation angle θ, as function of the acceptance angle $\psi = \gamma\theta < 1$, is [185]:

$$\bar{I}_{\gamma,\psi} = \bar{I}_\gamma \frac{\sigma_T}{\sigma_C} \frac{3}{2} \frac{(1 + X^{1/3}\psi^2/3)\psi^2}{[1 + (1 + X/2)\psi^2](1 + \psi^2)} \,. \tag{B.5}$$

The average power of radiation centered at the photon energy E_γ is simply $\bar{P}_{\gamma(,\psi)} = e\bar{I}_{\gamma(,\psi)}E_\gamma$.

The relative RMS bandwidth of scattered radiation within an acceptance angle $\psi = \gamma\theta < 1$ results [185]:

$$\begin{gathered}\left(\frac{\sigma_\omega}{\omega}\right)^2 \approx \left[\frac{\psi^2}{\sqrt{12}(1 + \psi^2/2)} + \frac{\bar{P}^2}{1 + \sqrt{12}\bar{P}^2}\right]^2 + \\ + \left(\frac{2 + X}{1 + X}\frac{\sigma_{E_e}}{E_e}\right)^2 + \left(\frac{1}{1 + X}\frac{\sigma_{E_l}}{E_l}\right)^2 + \left(\frac{M^2\lambda_0}{2\pi w_0}\right)^4 + \left(\frac{a_0^2/3}{1 + a_0^2/2}\right)^2 ,\end{gathered} \tag{B.6}$$

with λ_0 and $w_0 = 2\sigma_l$ the incident laser central wavelength and focal spot size at the IP, respectively, M^2 the laser beam quality factor, and a_0 the laser parameter. The ICS relative bandwidth is affected by the relative bandwidth of the laser, σ_{E_l}/E_l, the electron beam relative energy spread, σ_{E_e}/E_e, the effect of nonlinear Thomson scattering through a_0^2-terms, and the electron recoil effect through X. $\bar{P}$ is proportional to the electron beam normalized RMS transverse momenta [186]:

$$\bar{P} = \frac{\sqrt{2}\gamma}{(1 + X)} \sqrt{\left(\frac{\varepsilon_x}{\sigma_{e,x}}\right)^2 + \left(\frac{\varepsilon_y}{\sigma_{e,y}}\right)^2} , \tag{B.7}$$

and $\varepsilon_{x,y}$ is the electron beam geometric emittance. In the approximation of a Gaussian spectral distribution, the FWHM relative bandwidth is just $bw = 2.355 \times \sigma_\omega/\omega$.

The average spectral density within the collimation angle, in units of $[ph/sec/0.1\%bw]$, is then given by [185]:

$$\bar{S}_{\gamma,\psi} = \frac{d\bar{I}_{\gamma,\psi}}{d\omega/\omega} = \frac{\bar{I}_{\gamma,\psi}}{bw} \frac{10^{-3}E_\gamma}{\sqrt{2\pi}4\gamma^2 E_l} \,. \tag{B.8}$$

The average brilliance of the collimated radiation, in conventional units of

$[ph/sec/mm^2/mrad^2/0.1\%bw]$ is:

$$\bar{B}_{\gamma,\psi} \approx 10^{-15} \times \frac{\bar{I}_{\gamma,\psi}}{(2\pi)^{5/2}\epsilon_r^2 bw}\,, \tag{B.9}$$

where

$$\epsilon_r \approx \frac{\theta\Sigma_r}{2} \tag{B.10}$$

is the effective RMS transverse emittance of the scattered light in the approximation $(X << 1)$, and

$$\Sigma_r = \sqrt{\frac{2\pi\sigma_{e,x}\sigma_{e,y}\sigma_{l,x}\sigma_{l,y}}{A_\varphi}} \tag{B.11}$$

is the ICS pulse RMS effective transverse size at the IP. The corresponding RMS angular divergence is ϵ_r/Σ_r.

All corresponding *peak* quantities can be calculated from the average ones by dividing them by, respectively, the repetition rate (f) if to be expressed per pulse, and by the product of repetition rate and scattered pulse duration $(f \times \sqrt{2\pi}\Sigma_{t,\gamma})$ if to be expressed in unit of time $(1/sec)$. To do so, the effective ICS pulse RMS duration in the presence of a generic interaction angle φ is calculated as:

$$\Sigma_{t,\gamma} = \frac{2\pi\Sigma_x\Sigma_y}{A_\varphi}\sqrt{\sigma_{t,e}^2 + \sigma_{t,l}^2}\,. \tag{B.12}$$

Finally, we note that for nearly on-axis emission (so-called Compton edge), i.e. in the limit $\theta \to 0$, Eq. B.8 tends to [186]:

$$\bar{S}_{\gamma,\psi} \to \bar{S}_{\gamma,CE} \approx 1.5 \times 10^{-3}\bar{I}_\gamma\,. \tag{B.13}$$

In this case, the average brilliance in conventional units reads:

$$\bar{B}_{\gamma,CE} \approx 10^{-12} \times \frac{\bar{S}_{\gamma,CE}}{4\pi^2\varepsilon_x\varepsilon_y}\,, \tag{B.14}$$

and the peak brilliance in conventional units is given by:

$$B_{\gamma,CE} \approx 10^{-15}\frac{4r_e^2}{\pi^2}\frac{N_e N_l}{\sqrt{2\pi}\sigma_{t,e}\varepsilon_x\varepsilon_y\sigma_{l,x}\sigma_{l,y}}\,. \tag{B.15}$$

Bibliography

[1] D. M. Mills, J. R. Helliwell, Å. Kvick, T. Ohta, I. A. Robinson, and A. Authier. Report of the working group on synchrotron radiation nomenclature–brightness, spectral brightness or brilliance? *Synchrotron Radiation*, 12(3):385–385, 2005.

[2] M. Reiser. *Theory and design of charged particle beams*. John Wiley & Sons, 2008.

[3] T. Rao and D. H. Dowell. An engineering guide to photoinjectors. *arXiv preprint arXiv:1403.7539*, 2014.

[4] G. Margaritondo. Introduction to synchrotron radiation. 1988.

[5] Bright future for x-ray fels? *Nature Structural Biology*, 5(8):657–658, August 1998.

[6] M. Altarelli and A. Salam. The quest for brilliance: light sources from the third to the fourth generation. *europhysics news*, 35(2):47–50, 2004.

[7] P. Emma, R. Akre, J. Arthur, R. Bionta, C. Bostedt, J. Bozek, A. Brachmann, P. Bucksbaum, R. Coffee, F.-J. Decker, et al. First lasing and operation of an ångstrom-wavelength free-electron laser. *nature photonics*, 4(9):641–647, 2010.

[8] C. Pellegrini. Free electron lasers: development and applications. *Part. Accel.*, 33:159–170, 1990.

[9] C. Bostedt, S. Boutet, D. M. Fritz, Z. Huang, H.-J Lee, H. T. Lemke, A. Robert, W. F. Schlotter, J. J Turner, and G. J. Williams. Linac coherent light source: The first five years. *Reviews of Modern Physics*, 88(1):015007, 2016.

[10] L. C. Johansson, D. Arnlund, G. Katona, T. A. White, A. Barty, D. P. DePonte, R. L. Shoeman, C. Wickstrand, A. Sharma, G. J. Williams, et al. Structure of a

photosynthetic reaction centre determined by serial femtosecond crystallography. *Nature communications*, 4(1):2911, 2013.

[11] T. Ekeberg, M. Svenda, M. M. Seibert, C. Abergel, F. R. N. C. Maia, V. Seltzer, D. P. DePonte, A. Aquila, J. Andreasson, B. Iwan, et al. Single-shot diffraction data from the mimivirus particle using an x-ray free-electron laser. *Scientific data*, 3(1):1–7, 2016.

[12] J. S. Fraser, R. L. Sheffield, and E. R. Gray. High-brightness photoemitter development for electron accelerator injectors. *AIP Conf. Proc.*, 130:598–601, 1985.

[13] J. S. Fraser, R. L. Sheffield, and E. R. Gray. A new high-brightness electron injector for free electron lasers driven by rf linacs. *Nuclear Instruments and Methods in Physics Research Section A: Accelerators, Spectrometers, Detectors and Associated Equipment*, 250(1):71–76, 1986.

[14] R. L. Sheffield. High brightness electron sources. *Conf. Proc. C*, 950501:882–886, 1996.

[15] S. Owada, K. Togawa, T. Inagaki, T. Hara, T. Tanaka, Y. Joti, T. Koyama, K. Nakajima, H. Ohashi, Y. Senba, et al. A soft x-ray free-electron laser beamline at sacla: the light source, photon beamline and experimental station. *Synchrotron Radiation*, 25(1):282–288, 2018.

[16] Th. Tschentscher. Investigating ultrafast structural dynamics using high repetition rate x-ray fel radiation at european xfel. *The European Physical Journal Plus*, 138(3):274, 2023.

[17] F. Nolting, C. Bostedt, T. Schietinger, and H. Braun. The swiss light source and swissfel at the paul scherrer institute. *The European Physical Journal Plus*, 138(2):126, 2023.

[18] S. Di Mitri. On the importance of electron beam brightness in high gain free electron lasers. In *Photonics*, volume 2, pages 317–341. MDPI, 2015.

[19] R. Bonifacio, C. Pellegrini, and L. M. Narducci. Collective instabilities and high-gain regime in a free electron laser. *Optics Communications*, 50(6):373–378, 1984.

[20] P. Schmüser, M. Dohlus, J. Rossbach, and C. Behrens. Free-electron lasers in the ultraviolet and x-ray regime. *Springer Tracts in Modern Physics*, 258, 2014.

[21] K.-J. Kim. Brightness and coherence of synchrotron radiation and high-gain free electron lasers. *Nuclear Instruments and Methods in Physics Research Section A: Accelerators, Spectrometers, Detectors and Associated Equipment*, 261(1-2):44–53, 1987.

[22] R. L. Sheffield, M. J. Browman, B. E. Carlsten, and L. M. Young. Physics design of the high brightness linac for the advanced free-electron laser initiative at los alamos. *Nuclear Instruments and Methods in Physics Research Section A: Accelerators, Spectrometers, Detectors and Associated Equipment*, 318(1-3):282–289, 1992.

[23] P. Emma. Accelerator physics challenges of x-ray fel sase sources. Technical report, SLAC National Accelerator Lab., Menlo Park, CA (United States), 2002.

[24] G. A Krafft and G. Priebe. Compton sources of electromagnetic radiation. *Reviews of Accelerator Science and Technology*, 3(01):147–163, 2010.

[25] E. Esarey, S. K. Ride, and P. Sprangle. Nonlinear thomson scattering of intense laser pulses from beams and plasmas. *Physical Review E*, 48(4):3003, 1993.

[26] T. Skarzynski. Collecting data in the home laboratory: evolution of x-ray sources, detectors and working practices. *Biological Crystallography*, 69(7):1283–1288, 2013.

[27] X. Geng, L. Ji, and B. Shen. Quasimonochromatic bright gamma-ray generation from synchronized compton scattering via azimuthal spatial-temporal coupling. *Physical Review Applied*, 17(2):024055, 2022.

[28] C. R. Howell, M. W. Ahmed, A. Afanasev, J. R. M. Alesini, D.and Annand, A. Aprahamian, D. L. Balabanski, S. V. Benson, A. Bernstein, C. R. Brune, et al. International workshop on next generation gamma-ray source. *Journal of Physics G: Nuclear and Particle Physics*, 49(1):010502, 2021.

[29] E. Eggl, M. Dierolf, K. Achterhold, C. Jud, B. Günther, E. Braig, B. Gleich, and F. Pfeiffer. The munich compact light source: initial performance measures. *Synchrotron Radiation*, 23(5):1137–1142, 2016.

[30] S. Miyoshi, T. Akagi, S. Araki, Y. Funahashi, T. Hirose, Y. Honda, M. Kuriki, X. Li, T. Okugi, T. Omori, et al. Photon generation by laser-compton scattering

at the kek-atf. *Nuclear Instruments and Methods in Physics Research Section A: Accelerators, Spectrometers, Detectors and Associated Equipment*, 623(1):576–578, 2010.

[31] L. Faillace, R. G. Agostino, A. Bacci, R. Barberi, A. Bosotti, F. Broggi, P. Cardarelli, S. Cialdi, I. Drebot, V. Formoso, et al. Status of compact inverse compton sources in italy: Brixs and star. In *Advances in Laboratory-based X-Ray Sources, Optics, and Applications VII*, volume 11110, pages 14–21. SPIE, 2019.

[32] K. Dupraz, M. Alkadi, M. Alves, L. Amoudry, D. Auguste, J.-L. Babigeon, M. Baltazar, A. Benoit, J. Bonis, J. Bonenfant, et al. The thomx ics source. *Physics Open*, 5:100051, 2020.

[33] F. Albert, S. G. Anderson, D. J. Gibson, C. A. Hagmann, M. S. Johnson, M. Messerly, V. Semenov, M. Y. Shverdin, B. Rusnak, A. M. Tremaine, et al. Characterization and applications of a tunable, laser-based, mev-class compton-scattering γ-ray source. *Physical Review Special Topics—Accelerators and Beams*, 13(7):070704, 2010.

[34] R. Gradl, M. Dierolf, L. Hehn, B. Günther, A. Ö. Yildirim, B. Gleich, K. Achterhold, F. Pfeiffer, and K. S. Morgan. Propagation-based phase-contrast x-ray imaging at a compact light source. *Scientific reports*, 7(1):4908, 2017.

[35] S. Kulpe, M. Dierolf, E. Braig, B. Günther, K. Achterhold, B. Gleich, J. Herzen, E. Rummeny, F. Pfeiffer, and D. Pfeiffer. K-edge subtraction imaging for coronary angiography with a compact synchrotron x-ray source. *PLoS One*, 13(12):e0208446, 2018.

[36] S. Schleede, F. G. Meinel, M. Bech, J. Herzen, K. Achterhold, G. Potdevin, A. Malecki, S. Adam-Neumair, S. F. Thieme, F. Bamberg, et al. Emphysema diagnosis using x-ray dark-field imaging at a laser-driven compact synchrotron light source. *Proceedings of the National Academy of Sciences*, 109(44):17880–17885, 2012.

[37] I. V. Bazarov, B. M. Dunham, and C. K. Sinclair. Maximum achievable beam brightness from photoinjectors. *Physical review letters*, 102(10):104801, 2009.

[38] D. Filippetto, P. Musumeci, M. Zolotorev, and G. Stupakov. Maximum current density and beam brightness achievable by laser-driven electron sources. *Physical Review Special Topics-Accelerators and Beams*, 17(2):024201, 2014.

[39] L. Serafini and J. B. Rosenzweig. Envelope analysis of intense relativistic quasilaminar beams in rf photoinjectors:ma theory of emittance compensation. *Phys. Rev. E*, 55:7565–7590, Jun 1997.

[40] B. E. Carlsten. New photoelectric injector design for the los alamos national laboratory xuv fel accelerator. *Nuclear Instruments and Methods in Physics Research Section A: Accelerators, Spectrometers, Detectors and Associated Equipment*, 285(1-2):313–319, 1989.

[41] Z. Huang, J. Wu, and T. Shaftan. Microbunching instability due to bunch compression. *ICFA beam dynamics newsletter*, 38(SLAC-PUB-11597), 2005.

[42] A. D. Brynes. Characterisation of microbunching instability at the fermi free electron laser. *Proc. IPAC'23*, 2023.

[43] D. Ratner, C. Behrens, Y. Ding, Z. Huang, A. Marinelli, T. Maxwell, and F. Zhou. Time-resolved imaging of the microbunching instability and energy spread at the linac coherent light source. *Physical Review Special Topics-Accelerators and Beams*, 18(3):030704, 2015.

[44] Z. Huang and G. Stupakov. Control and application of beam microbunching in high brightness linac-driven free electron lasers. *Nuclear Instruments and Methods in Physics Research Section A: Accelerators, Spectrometers, Detectors and Associated Equipment*, 907:182–187, 2018.

[45] I. Zagorodnov and M. Dohlus. Semianalytical modeling of multistage bunch compression with collective effects. *Physical Review Special Topics—Accelerators and Beams*, 14(1):014403, 2011.

[46] C. Zhang, Y. Jiao, W. Liu, and C.-Y. Tsai. Suppression of the coherent synchrotron radiation induced emittance growth in a double-bend achromat with bunch compression. *Physical Review Accelerators and Beams*, 26(5):050701, 2023.

[47] S. Di Mitri, M. Cornacchia, and S. Spampinati. Cancellation of coherent synchrotron radiation kicks with optics balance. *Physical Review Letters*, 110(1):014801, 2013.

[48] F. Zeng, Y. Jiao, W. Liu, and C.-Y. Tsai. Cancelation of coherent synchrotron radiation kicks in chicane bunch compressors. *Physical Review Accelerators and Beams*, 28(7):070701, 2025.

[49] F. Zeng, Y. Jiao, W. Liu, and C.-Y. Tsai. Solvable model of the coherent synchrotron radiation effects in a four-bend chicane compressor. *New Journal of Physics*, 27(6):063801, 2025.

[50] A. Bazzani, P. Cardarelli, G. Paternò, M. Placidi, A. Taibi, and G. Turchetti. Bocxs: A compact multidisciplinary x-ray source. *Physics Open*, 5:100036, 2020.

[51] E. Allaria, L. Badano, S. Bassanese, F. Capotondi, D. Castronovo, P. Cinquegrana, M. B. Danailov, G. D'auria, A. Demidovich, R. De Monte, et al. The fermi free-electron lasers. *Synchrotron Radiation*, 22(3):485–491, 2015.

[52] M. Ferrario, D. Alesini, M. P. Anania, M. Artioli, A. Bacci, S. Bartocci, R. Bedogni, M. Bellaveglia, A. Biagioni, F. Bisesto, et al. Eupraxia@ sparc_lab design study towards a compact fel facility at lnf. *Nuclear Instruments and Methods in Physics Research Section A: Accelerators, Spectrometers, Detectors and Associated Equipment*, 909:134–138, 2018.

[53] S. Di Mitri, G. Campri, F. Elisii, G. Perosa, and S. Spampinati. Systematic and comprehensive comparison of two semianalytical models of microbunching instability. *Physical Review Accelerators and Beams*, 28(4):044401, 2025.

[54] L. D. Landau and E. M. Lifshitz. *Mechanics, Third Edition: Volume 1 (Course of Theoretical Physics)*. Butterworth-Heinemann, 3 edition, January 1976.

[55] S. Humphries. *Charged particle beams*. Dover, Mineola, New York, 2013.

[56] A. Mostacci, M. Bellaveglia, E. Chiadroni, A. Cianchi, M. Ferrario, D. Filippetto, G. Gatti, and C. Ronsivalle. Chromatic effects in quadrupole scan emittance measurements. *Physical Review Special Topics—Accelerators and Beams*, 15(8):082802, 2012.

[57] F. J. Sacherer. Rms envelope equations with space charge. *IEEE Transactions on Nuclear Science*, 18(3):1105–1107, 1971.

[58] J. B. Rosenzweig. *Fundamentals of beam physics*. Oxford University Press, 2003.

[59] M. Ferrario, V. Fusco, M. Migliorati, and L. Palumbo. Emittance degradation due to wake fields in a high brightness photoinjector. *International Journal of Modern Physics A*, 22(23):4214–4234, 2007.

[60] D. H. Dowell, S. Lidia, and J. F. Schmerge. Emittance compensation. USPAS Lecture 6, High Brightness Electron Injectors for Light Sources, January 2007. Available at `https://uspas.fnal.gov/materials/08UCSC/HB16_Emittance_Compensation.pdf`.

[61] C.-x. Wang. Comment on the invariant-envelope solution in rf photoinjectors. *Nuclear Instruments and Methods in Physics Research Section A: Accelerators, Spectrometers, Detectors and Associated Equipment*, 557(1):94–97, 2006.

[62] M. Ferrario. Space charge mitigation. *CERN Yellow Reports: School Proceedings*, 5:89–89, 2018.

[63] D. H. Dowell and J. F. Schmerge. Quantum efficiency and thermal emittance of metal photocathodes. *Phys. Rev. ST Accel. Beams*, 12:074201, Jul 2009.

[64] R. Xiang and J. Schaber. Review of recent progress on advanced photocathodes for superconducting rf guns. *Micromachines*, 13(8), 2022.

[65] H. Chen, L. Yan, Q. Tian, Z. Lin, D. Wang, C. Cheng, J. Shi, H. Zha, Y. Du, H. Chen, W. Huang, and C. Tang. Commissioning the photoinjector of a gamma-ray light source. *Phys. Rev. Accel. Beams*, 22:053403, May 2019.

[66] E. Panofski, R. Assmann, F. Burkart, U. Dorda, L. Genovese, F. Jafarinia, S. Jaster-Merz, M. Kellermeier, W. Kuropka, F. Lemery, B. Marchetti, D. Marx, F. Mayet, T. Vinatier, and S. Yamin. Commissioning results and electron beam characterization with the s-band photoinjector at sinbad-ares. *Instruments*, 5(3), 2021.

[67] H. Duran Yildiz, D. Porsuk, R. Cakir, and H. Tugay. Design and comparison of superconducting rf gun cavities and beam dynamics for linear electron accelerators.

Nuclear Instruments and Methods in Physics Research Section A: Accelerators, Spectrometers, Detectors and Associated Equipment, 939:74–82, 2019.

[68] D. T. Palmer, X. J. Wang, R. H. Miller, M. Babzien, I. Ben-Zvi, C. Pellegrini, J. Sheehan, J. Skaritka, H. Winick, M. Woodle, and V. Yakimenko. Initial commissioning results of the next generation photoinjector. *AIP Conference Proceedings*, 398(1):695–704, 03 1997.

[69] J.-H. Han. Design of a low emittance and high repetition rate s-band photoinjector. *Nuclear Instruments and Methods in Physics Research Section A: Accelerators, Spectrometers, Detectors and Associated Equipment*, 757:1–6, 2014.

[70] T. P. Wangler. *RF linear accelerators.* John Wiley & Sons, Ltd, 2008.

[71] K.-J. Kim. RF and Space Charge Effects in Laser Driven RF Electron Guns. *Nucl. Instrum. Meth. A*, 275:201–218, 1989.

[72] K. Floettmann. rf-induced beam dynamics in rf guns and accelerating cavities. *Phys. Rev. ST Accel. Beams*, 18:064801, Jun 2015.

[73] D. H. Dowell. Sources of emittance in rf photocathode injectors: Intrinsic emittance, space charge forces due to non-uniformities, rf and solenoid effects. *Cornell U physics ArXive, http://arxiv.org/abs/1610.01242*, arXiv:1610.01242v3 [physics.acc-ph], 10 2016.

[74] D. C. Carey, K. L. Brown, and F. Rothacker. Third-order transport with mad input: a computer program for designing charged particle beam transport systems. Technical report, SLAC National Accelerator Laboratory (SLAC), Menlo Park, CA (United States), 1998.

[75] M. Ferrario, D. Alesini, A. Bacci, M. Bellaveglia, R. Boni, M. Boscolo, M. Castellano, L. Catani, E. Chiadroni, S. Cialdi, et al. Direct measurement of the double emittance minimum in the beam dynamics of the sparc high-brightness photoinjector. *Physical review letters*, 99(23):234801, 2007.

[76] L. Serafini and M. Ferrario. Velocity bunching in photo-injectors. In *AIP conference proceedings*, volume 581, pages 87–106. American Institute of Physics, 2001.

[77] P. Piot. State-of-the-art electron bunch compression. In *Proc. LINAC*, pages 528–532, 2004.

[78] M. Ferrario, D. Alesini, A. Bacci, M. Bellaveglia, R. Boni, M. Boscolo, M. Castellano, E. Chiadroni, A. Cianchi, L. Cultrera, et al. Experimental demonstration of emittance compensation with velocity bunching. *Physical review letters*, 104(5):054801, 2010.

[79] S. G. Anderson, P. Musumeci, J. B. Rosenzweig, W. J. Brown, R. J. England, M. Ferrario, J. S. Jacob, M. C. Thompson, G. Travish, A. M. Tremaine, et al. Velocity bunching of high-brightness electron beams. *Physical Review Special Topics—Accelerators and Beams*, 8(1):014401, 2005.

[80] S. Di Mitri. Bunch length compressors. *CERN Yellow Reports: School Proceedings*, 1:363–363, 2018.

[81] P. Emma et al. X-band rf harmonic compensation for linear bunch compression in the lcls. *SLAC, Stanford, CA, USA, Rep. ILCLS-TN-01-1*, 2001.

[82] M. Dohlus and T. Limberg. Bunch compression stability dependence on rf parameters. In *Proceedings of FEL*, 2005.

[83] P. Castro. *Beam trajectory calculations in bunch compressors of TTF2*. Dt. Elektronen-Synchrotron DESY, 2003.

[84] S. Di Mitri. Coherent synchrotron radiation and microbunching instability. *CERN Yellow Reports: School Proceedings*, 1:381–381, 2018.

[85] M. Dohlus, T. Limberg, and P. Emma. Bunch compression for linac-based fel's. electron bunch length compression. *ICFA Beam Dynamics Newsletter*, 38(SLAC-REPRINT-2005-165), 2006.

[86] C. Mitchell, J. Qiang, and P. Emma. Longitudinal pulse shaping for the suppression of coherent synchrotron radiation-induced emittance growth. *Physical Review Special Topics—Accelerators and Beams*, 16(6):060703, 2013.

[87] Ya. S. Derbenev, J. Rossbach, E. L. Saldin, and V. D. Shiltsev. Tesla-fel 95-05. *DESY, Hamburg, Germany*, 1995.

[88] E. L. Saldin, E. A. Schneidmiller, and M. V. Yurkov. On the coherent radiation of an electron bunch moving in an arc of a circle. *Nuclear Instruments and Methods in Physics Research Section A: Accelerators, Spectrometers, Detectors and Associated Equipment*, 398(2-3):373–394, 1997.

[89] R. L. Warnock and P. L. Morton. Fields excited by a beam in a smooth toroidal chamber: pt. 1. longitudinal coupling impedance. *Part. Accel.*, 25(SLAC-PUB-4562):113, 1988.

[90] V. Yakimenko, M. Fedurin, V. Litvinenko, A. Fedotov, D. Kayran, and P. Muggli. Experimental observation of suppression of coherent-synchrotron-radiation–induced beam-energy spread with shielding plates. *Physical Review Letters*, 109(16):164802, 2012.

[91] Z. Huang, M. Borland, P. Emma, J. Wu, C. Limborg, G. Stupakov, and J. Welch. Suppression of microbunching instability in the linac coherent light source. *Physical Review Special Topics—Accelerators and Beams*, 7(7):074401, 2004.

[92] J. Rosenzweig, C. Pellegrini, L. Serafini, C. Ternieden, and G. Travish. Space-charge oscillations in a self-modulated electron beam in multi-undulator free-electron lasers. *Nuclear Instruments and Methods in Physics Research Section A: Accelerators, Spectrometers, Detectors and Associated Equipment*, 393(1-3):376–379, 1997.

[93] M. Venturini. An effective longitudinal space-charge impedance model for beams with non-uniform and non-axissymmetric transverse density. 2008.

[94] M. Venturini. Models of longitudinal space-charge impedance for microbunching instability. *Physical Review Special Topics—Accelerators and Beams*, 11(3):034401, 2008.

[95] J. B. Murphy, S. Krinsky, and R. L. Gluckstern. Longitudinal wakefield for synchrotron radiation. In *Proceedings Particle Accelerator Conference*, volume 5, pages 2980–2982. IEEE, 1995.

[96] S. Heifets, G. Stupakov, and S. Krinsky. Coherent synchrotron radiation instability in a bunch compressor. *Physical Review Special Topics-Accelerators and Beams*, 5(6):064401, 2002.

[97] E. L. Saldin, E. A. Schneidmiller, and M. V. Yurkov. Klystron instability of a relativistic electron beam in a bunch compressor. *Nuclear Instruments and Methods in Physics Research Section A: Accelerators, Spectrometers, Detectors and Associated Equipment*, 490(1-2):1–8, 2002.

[98] M. Venturini. Microbunching instability in single-pass systems using a direct two-dimensional vlasov solver. *Physical Review Special Topics—Accelerators and Beams*, 10(10):104401, 2007.

[99] Z. Huang, A. Brachmann, F.-J. Decker, Y. Ding, D. H. Dowell, P. Emma, J. Frisch, S. Gilevich, G. Hays, Ph. Hering, et al. Measurements of the linac coherent light source laser heater and its impact on the x-ray free-electron laser performance. *Physical Review Special Topics—Accelerators and Beams*, 13(2):020703, 2010.

[100] S. Di Mitri and S. Spampinati. Microbunching instability suppression via electron-magnetic-phase mixing. *Physical Review Letters*, 112(13):134802, 2014.

[101] M. Venturini. Csr-induced emittance growth in achromats: Linear formalism revisited. *Nuclear Instruments and Methods in Physics Research Section A: Accelerators, Spectrometers, Detectors and Associated Equipment*, 794:109–112, 2015.

[102] J. Hecht. Short history of laser development. *Optical engineering*, 49(9):091002–091002, 2010.

[103] S. Di Mitri and M. Cornacchia. Electron beam brightness in linac drivers for free-electron-lasers. *Physics Reports*, 539(1):1–48, 2014.

[104] B. Günther, R. Gradl, C. Jud, E. Eggl, J. Huang, S. Kulpe, K. Achterhold, B. Gleich, M. Dierolf, and F. Pfeiffer. The versatile x-ray beamline of the munich compact light source: design, instrumentation and applications. *Synchrotron Radiation*, 27(5):1395–1414, 2020.

[105] Y. Du, L. Yan, J. Hua, Q. Du, Z. Zhang, R. Li, H. Qian, W. Huang, H. Chen, and C. Tang. Generation of first hard x-ray pulse at tsinghua thomson scattering x-ray source. *Review of Scientific Instruments*, 84(5), 2013.

[106] W. Graves. The cxfel project at arizona state university. In *Proceedings of the 67th ICFA Adv. Beam Dyn. Workshop Future Light Sources, Luzern, Switzerland*, pages 54–57, 2023.

[107] K. Deitrick, G. H. Hoffstaetter, C. Franck, B. D. Muratori, P. H. Williams, G. A Krafft, B. Terzić, J. Crone, and H. Owen. Intense monochromatic photons above 100 kev from an inverse compton source. *Physical Review Accelerators and Beams*, 24(5):050701, 2021.

[108] T. Akagi, A. Kosuge, S. Araki, R. Hajima, Y. Honda, T. Miyajima, M. Mori, R. Nagai, N. Nakamura, M. Shimada, et al. Narrow-band photon beam via laser compton scattering in an energy recovery linac. *Physical Review Accelerators and Beams*, 19(11):114701, 2016.

[109] G. Paternò, P. Cardarelli, M. Gambaccini, L. Serafini, V. Petrillo, I. Drebot, and A. Taibi. Inverse compton radiation: a novel x-ray source for k-edge subtraction angiography? *Physics in Medicine & Biology*, 64(18):185002, 2019.

[110] `https://www.desy.de/~mpyflo/`.

[111] M. Borland. Elegant: A flexible sdds-compliant code for accelerator simulation. Technical report, Argonne National Lab., IL (US), 2000.

[112] G. Campri, S. Di Mitri, A. Giribono, D. Alesini, A. Bazzani, G. Turchetti, and M. Placidi. Electron beam source and switchyard design for two-energy operation of x-ray compton sources. *Physical Review Accelerators and Beams*, 28(5):051601, 2025.

[113] J. Rosenzweig and E. Colby. Charge and wavelength scaling of rf photoinjectors: a design tool. In *Proceedings Particle Accelerator Conference*, volume 2, pages 957–960. IEEE, 1995.

[114] G. Campri, S. Di Mitri, A. Giribono, D. Alesini, M. Placidi, A. Bazzani, G. Turchetti, et al. Characterisation and optimisation of a c-band photo-injector for compact light sources. In *(IPAC'24) Proceedings of the 15th International particle accelerator conference*, pages 1–4. JACoW Publishing, 2024.

[115] D. Alesini, F. Cardelli, G.i Castorina, M. Croia, M. Diomede, M. Ferrario, A. Gallo, A. Giribono, B. Spataro, C. Vaccarezza, et al. Design of a full c-band injector for ultra-high brightness electron beam. In *Proc. 10th International Particle Accelerator Conference (IPAC'19)*, number 10, pages 1979–1982. JACoW Publishing, 2019.

[116] A. Giribono, D. Alesini, F. Cardelli, G. Di Raddo, L. Faillace, M. Ferrario, A. Gallo, A. Gizzi, S. Lauciani, A. Liedl, et al. Dynamics studies of high brightness electron beams in a normal conducting, high repetition rate c-band injector. *Physical Review Accelerators and Beams*, 26(8):083402, 2023.

[117] L. S. Cowie, P. Williams, A. Brynes, J. K. Jones, A. Moss, A. E. Wheelhouse, W. L. Millar, G. Burt, R. Apsimon, and O. Mete. An x-band lineariser for the clara fel. *Proc. IPAC'18*, pages 3848–3851, 2018.

[118] P. Denham, A. Ody, and P. Musumeci. X-band harmonic longitudinal phase space linearization at the pegasus photoinjector. In *Proc. NAPAC'22*, pages 508–511, 2022.

[119] W. L. Millar, A. Grudiev, W. Wuensch, N. C. Lasheras, G. McMonagle, R. Zennaro, P. Craievich, M. Bopp, T. G. Lucas, M. Volpi, et al. High-power test of two prototype x-band accelerating structures based on swissfel fabrication technology. *IEEE Transactions on Nuclear Science*, 70(1):1–19, 2022.

[120] X.-C. Lin, H. Zha, J.-R. Shi, Q. Gao, J.-Y. Liu, L.-Y. Zhou, J. Gao, H.-B. Chen, and C.-X. Tang. Fabrication, tuning, and high-gradient testing of an x-band traveling-wave accelerating structure for vigas. *Nuclear Science and Techniques*, 33(8):102, 2022.

[121] M. Borland. Simple method for particle tracking with coherent synchrotron radiation. *Physical Review Special Topics-Accelerators and Beams*, 4(7):070701, 2001.

[122] G. Stupakov and P. Emma. Csr wake for a short magnet in ultrarelativistic limit. In *Proceedings of the 8th European Particle Accelerator Conference, Paris*, page 1479. Citeseer, 2002.

[123] S. Di Mitri, E. Allaria, L. Badano, C. Bontoiu, M. Cornacchia, P. Craievich, M. Danailov, G. De Ninno, B. Diviacco, O. Ferrando, et al. Design and simulation challenges for fermi@ elettra. *Nuclear Instruments and Methods in Physics Research Section A: Accelerators, Spectrometers, Detectors and Associated Equipment*, 608(1):19–27, 2009.

[124] A. D. Brynes, P. Smorenburg, I. Akkermans, E. Allaria, L. Badano, S. Brussaard, M. Danailov, A. Demidovich, G. De Ninno, D. Gauthier, et al. Beyond the limits of 1d coherent synchrotron radiation. *New Journal of Physics*, 20(7):073035, 2018.

[125] A. D. Brynes, P. Smorenburg, I. Akkermans, E. Allaria, L. Badano, S. Brussaard, M. Danailov, A. Demidovich, G. De Ninno, D. Gauthier, et al. Addendum: Be-

yond the limits of 1d coherent synchrotron radiation (2018 new j. phys. 20 073035). *New Journal of Physics*, 23(4):049401, 2021.

[126] A. Castilla, R. Apsimon, G. Burt, X. Wu, A. Latina, X. Liu, I. Syratchev, W. Wuensch, B. Spataro, and A. W. Cross. Ka-band linearizer structure studies for a compact light source. *Physical Review Accelerators and Beams*, 25(11):112001, 2022.

[127] J. Y. Jung. Private communication.

[128] M. Borland. Modeling of the microbunching instability. *Physical Review Special Topics—Accelerators and Beams*, 11(3):030701, 2008.

[129] F.-J. Decker. Timing stability at lcls. Technical report, SLAC National Accelerator Lab., Menlo Park, CA (United States), 2018.

[130] L. Piersanti, D. Alesini, M. Bellaveglia, S. Bini, B. Buonomo, F. Cardelli, C. Di Giulio, E. Di Pasquale, M. Diomede, L. Faillace, et al. Commissioning and first results of an x-band llrf system for tex test facility at lnf-infn. In *Journal of Physics: Conference Series*, volume 2420, page 012075. IOP Publishing, 2023.

[131] Z. Geng, P. Craievich, R. Kalt, J. Alex, C.H. Gough, T. Lippuner, M. Pedrozzi, F. Löhl, V.R. Arsov, S. Reiche, et al. Rf jitter and electron beam stability in the swissfel linac. In *39th Free Electron Laser Conf*, pages 400–403, 2019.

[132] L. Piersanti, M. Bellaveglia, F. Cardelli, A. Gallo, R. Magnanimi, S. Quaglia, M. Scampati, G. Scarselletta, B. Serenellini, and S. Tocci. Design and test of a klystron intra-pulse phase feedback system for electron linear accelerators. In *Photonics*, volume 11, page 413. MDPI, 2024.

[133] W. Decking and F. Obier. Layout of the beam switchyard at the european xfel. *EPAC08-WEPC073, Genoa, Italy*, 2008.

[134] F. Obier, W. Decking, M. Hüning, J. Wortmann, et al. Long pulse kicker for european xfel beam distribution. *Proc. FEL'19*, pages 357–359, 2019.

[135] A. Bacci, V. Petrillo, and M.R. Conti. Giotto: a genetic code for demanding beam-dynamics optimizations. *Proc. IPAC'16*, pages 3073–3076, 2016.

[136] C. Sun and Y. K. Wu. Theoretical and simulation studies of characteristics of a compton light source. *Physical Review Special Topics—Accelerators and Beams*, 14(4):044701, 2011.

[137] C. Sun, J. Li, G. Rusev, A. P. Tonchev, and Y. K. Wu. Energy and energy spread measurements of an electron beam by compton scattering method. *Physical Review Special Topics—Accelerators and Beams*, 12(6):062801, 2009.

[138] D. A. Kleinman. Theory of second harmonic generation of light. *Physical Review*, 128(4):1761, 1962.

[139] S. White. *Determination of the absolute luminosity at the LHC*. PhD thesis, Université Paris Sud-Paris XI, 2010.

[140] T. Suzuki. General formulae of luminosity for various types of colliding beam machines. Technical report, National Lab. for High Energy Physics, 1976.

[141] A. Courjaud and A. Golinelli. Amplitude systems, S.A, (amplitude-laser.com), Private communication.

[142] V. Mușat, A. Latina, and G. D'Auria. A high-energy and high-intensity inverse compton scattering source based on compactlight technology. In *Photonics*, volume 9, page 308. MDPI, 2022.

[143] L. Giuliano, F. Bosco, M. Carillo, L. Ficcadenti, M. Magi, A. Mostacci, L. Palumbo, M. Migliorati, L. Faillace, D. Alesini, et al. Design and test of c-band linac prototypes for electron flash radiotherapy. In *Journal of Physics: Conference Series*, volume 2687, page 092005. IOP Publishing, 2024.

[144] G. Zhang, Z. Zhang, W. Gao, and H. Quan. Treatment planning consideration for very high-energy electron flash radiotherapy. *Physica Medica*, 107:102539, 2023.

[145] L. Giuliano, F. Bosco, M. Carillo, D. De Arcangelis, L. Ficcadenti, D. Francescone, A. De Gregorio, G. Franciosini, M. Migliorati, A. Mostacci, et al. Proposal of a vhee linac for flash radiotherapy. In *Journal of Physics: Conference Series*, volume 2420, page 012087. IOP Publishing, 2023.

[146] J. Rosenzweig et al. DESY Report No. TESLA-FEL-96-15 (1996).

[147] L. Giannessi and C. Masciovecchio. Fermi: present and future challenges. *Applied Sciences*, 7(6):640, 2017.

[148] J. Qiang, Y. Ding, P. Emma, Z. Huang, D. Ratner, T. O. Raubenheimer, M. Venturini, and F. Zhou. Start-to-end simulation of the shot-noise driven microbunching instability experiment at the linac coherent light source. *Physical Review Accelerators and Beams*, 20(5):054402, 2017.

[149] M. Migliorati. A vlasov solver for collective effects in particle accerators. 2009.

[150] C.-Y. Tsai, D. Douglas, R. Li, and C. Tennant. Linear microbunching analysis for recirculation machines. *Physical Review Accelerators and Beams*, 19(11):114401, 2016.

[151] Z. Huang and K.-J. Kim. Formulas for coherent synchrotron radiation microbunching in a bunch compressor chicane. *Physical Review Special Topics-Accelerators and Beams*, 5(7):074401, 2002.

[152] R. A. Bosch, K. J. Kleman, and J. Wu. Modeling two-stage bunch compression with wakefields: Macroscopic properties and microbunching instability. *Physical Review Special Topics—Accelerators and Beams*, 11(9):090702, 2008.

[153] J. Wu, Z. Huang, and P. Emma. Analytical analysis of longitudinal space charge effects for a bunched beam with radial dependence. *Physical Review Special Topics—Accelerators and Beams*, 11(4):040701, 2008.

[154] S. Di Mitri, G. Perosa, A. Brynes, I. Setija, S. Spampinati, P. H. Williams, A. Wolski, E. Allaria, S. Brussaard, L. Giannessi, et al. Experimental evidence of intrabeam scattering in a free-electron laser driver. *New Journal of Physics*, 22(8):083053, 2020.

[155] S. Di Mitri, G. Perosa, A. Brynes, I. Setija, S. Spampinati, P.H. Williams, A. Wolski, E. Allaria, S. Brussaard, L. Giannessi, et al. Addendum: Experimental evidence of intrabeam scattering in a free-electron laser driver (2020 new j. phys. 22 083053). *New Journal of Physics*, 24(3):039401, 2022.

[156] G. Penco, G. Perosa, E. Allaria, S. Di Mitri, E. Ferrari, L. Giannessi, S. Spampinati, C. Spezzani, and M. Veronese. Enhanced seeded free electron laser per-

formance with a "cold" electron beam. *Physical review accelerators and beams*, 23(12):120704, 2020.

[157] L.-H. Yu. Generation of intense uv radiation by subharmonically seeded single-pass free-electron lasers. *Physical Review A*, 44(8):5178, 1991.

[158] L.-H. Yu, M. Babzien, I. Ben-Zvi, L. F. DiMauro, A. Doyuran, W. Graves, E. Johnson, S. Krinsky, R. Malone, I. Pogorelsky, et al. High-gain harmonic-generation free-electron laser. *Science*, 289(5481):932–934, 2000.

[159] C. J. Bocchetta and G. De Ninno. *FERMI@Elettra: conceptual design report*. Elettra Sincrotrone Trieste, 2007.

[160] A. Franciosi and M. Kiskinova. Elettra-sincrotrone trieste: present and future. *The European Physical Journal Plus*, 138(1):79, 2023.

[161] E. Allaria, B. Diviacco, C. Callegari, P. Finetti, B. Mahieu, J. Viefhaus, M. Zangrando, G. De Ninno, G. Lambert, E. Ferrari, et al. Control of the polarization of a vacuum-ultraviolet, high-gain, free-electron laser. *Physical Review X*, 4(4):041040, 2014.

[162] E. Allaria, R. Appio, L. Badano, W. A. Barletta, S. Bassanese, S. G. Biedron, A. Borga, E. Busetto, D. Castronovo, P. Cinquegrana, et al. Highly coherent and stable pulses from the fermi seeded free-electron laser in the extreme ultraviolet. *Nature Photonics*, 6(10):699–704, 2012.

[163] M. Svandrlik. Operation of fermi fels for users. In *Advances in X-ray Free-Electron Lasers Instrumentation III*, volume 9512, pages 116–121. SPIE, 2015.

[164] E. Allaria, F. Bencivenga, R. Borghes, F. Capotondi, D. Castronovo, P. Charalambous, P. Cinquegrana, M. B. Danailov, G. De Ninno, A. Demidovich, et al. Two-colour pump–probe experiments with a twin-pulse-seed extreme ultraviolet free-electron laser. *Nature Communications*, 4(1):2476, 2013.

[165] G. De Ninno, B. Mahieu, E. Allaria, L. Giannessi, and S. Spampinati. Chirped seeded free-electron lasers: Self-standing light sources for two-color pump-probe experiments. *Physical review letters*, 110(6):064801, 2013.

[166] O. Y. Gorobtsov, G. Mercurio, F. Capotondi, P. Skopintsev, S. Lazarev, I. A Zaluzhnyy, M. B. Danailov, M. Dell'Angela, M. Manfredda, E. Pedersoli, et al. Seeded x-ray free-electron laser generating radiation with laser statistical properties. *Nature communications*, 9(1):4498, 2018.

[167] E. Ferrari, C. Spezzani, F. Fortuna, R. Delaunay, F. Vidal, I. Nikolov, P. Cinquegrana, B. Diviacco, D. Gauthier, G. Penco, et al. Widely tunable two-colour seeded free-electron laser source for resonant-pump resonant-probe magnetic scattering. *Nature Communications*, 7(1):10343, 2016.

[168] L. Giannessi et al. First lasing of fermi fel-2 (1st stage) and fermi fel-1 recent results, talk at the fel 2012 conference. *Nara, Japan*, 2012.

[169] M. Svandrlik, E. Allaria, L. Badano, F. Bencivenga, C. Callegari, F. Capotondi, D. Castronovo, P. Cinquegrana, M. Coreno, R. Cucini, et al. The fermi seeded fel facility: Operational experience and future perspectives. In *6th Int. Particle Accelerator Conf.(IPAC'15), Richmond, VA, USA, May 3-8, 2015*, pages 1538–1541. JACOW, Geneva, Switzerland, 2015.

[170] P. Rebernik Ribič, E. Roussel, G. Penn, G. De Ninno, L. Giannessi, G. Penco, and E. Allaria. Echo-enabled harmonic generation studies for the fermi free-electron laser. In *Photonics*, volume 4, page 19. MDPI, 2017.

[171] C. Spezzani et al. Echo-enabled harmonic generation at fermi fel-1: commissioning and initial user experience. *Proc. IPAC'24*, pages 1889–1892, 2024.

[172] https://www.elettra.eu/images/Documents/FERMI

[173] J. B. Rosenzweig, B. Breizman, T. Katsouleas, and J. J. Su. Acceleration and focusing of electrons in two-dimensional nonlinear plasma wake fields. *Physical Review A*, 44(10):R6189, 1991.

[174] W. P. Leemans, B. Nagler, A. J. Gonsalves, Cs. Tóth, K. Nakamura, C. G. R. Geddes, E. Esarey, C. B. Schroeder, and S. M. Hooker. Gev electron beams from a centimetre-scale accelerator. *Nature physics*, 2(10):696–699, 2006.

[175] J. B. Rosenzweig, G. Andonian, M. Ferrario, P. Muggli, O. Williams, V. Yakimenko, and K. Xuan. Plasma wakefields in the quasi-nonlinear regime. In

AIP Conference Proceedings, volume 1299, pages 500–504. American Institute of Physics, 2010.

[176] S. Romeo, E. Chiadroni, M. Croia, M. Ferrario, A. Giribono, A. Marocchino, F. Mira, R. Pompili, A. R. Rossi, and C. Vaccarezza. Simulation design for forthcoming high quality plasma wakefield acceleration experiment in linear regime at sparc_lab. *Nuclear Instruments and Methods in Physics Research Section A: Accelerators, Spectrometers, Detectors and Associated Equipment*, 909:71–75, 2018.

[177] E. Esarey, C. B. Schroeder, and W. P. Leemans. Physics of laser-driven plasma-based electron accelerators. *Reviews of modern physics*, 81(3):1229–1285, 2009.

[178] R. Pompili, E. Chiadroni, A. Cianchi, M. Ferrario, A. Gallo, V. Shpakov, and F. Villa. From sparc_lab to eupraxia@ sparc_lab. *Instruments*, 3(3):45, 2019.

[179] F. Villa, D. Alesini, M. P. Anania, M. Angelucci, A. Bacci, A. Balerna, M. Bellaveglia, A. Biagioni, B. Buonuomo, S. Cantarella, et al. Eupraxia@ sparc_lab status update. In *X-Ray Free-Electron Lasers: Advances in Source Development and Instrumentation VI*, volume 12581, pages 92–101. SPIE, 2023.

[180] INFN-LNF. Private communication.

[181] E. L. Saldin, E. A. Schneidmiller, and M. V. Yurkov. Longitudinal space charge-driven microbunching instability in the tesla test facility linac. *Nuclear Instruments and Methods in Physics Research Section A: Accelerators, Spectrometers, Detectors and Associated Equipment*, 528(1-2):355–359, 2004.

[182] S. Spampinati, E. Allaria, L. Badano, S. Bassanese, S. Biedron, D. Castronovo, P. Craievich, M. B. Danailov, A. Demidovich, G. De Ninno, et al. Laser heater commissioning at an externally seeded free-electron laser. *Physical Review Special Topics-Accelerators and Beams*, 17(12):120705, 2014.

[183] W. Colson. The nonlinear wave equation for higher harmonics in free-electron lasers. *IEEE Journal of Quantum Electronics*, 17(8):1417–1427, 2003.

[184] V. B. Berestetskii, L. P. Pitaevskii, and E. M. Lifshitz. *Quantum Electrodynamics: Volume 4*, volume 4. Elsevier, 2012.

[185] C. Curatolo, I. Drebot, V. Petrillo, and L. Serafini. Analytical description of photon beam phase spaces in inverse compton scattering sources. *Physical Review Accelerators and Beams*, 20(8):080701, 2017.

[186] K. E. Deitrick, G. A. Krafft, B. Terzić, and J. R. Delayen. High-brilliance, high-flux compact inverse compton light source. *Physical Review Accelerators and Beams*, 21(8):080703, 2018.

Acknowledgements

I would like to express my sincere gratitude to Massimo Placidi, the original initiator of the BoCXS project, whose vision and ideas laid the foundation for much of the work presented in this thesis. I am also deeply thankful to Marcello Rossetti Conti and Alberto Bacci for the many insightful discussions and valuable suggestions on the optics optimization of the BoCXS beamline. My sincere thanks go to Gilles Silvi for his important contribution to the use of the GIOTTO framework for the BoCXS' jitter studies, and to Francesco Demurtas for his help and availability to friendly discussions throughout these years.

Finally, I would like to thank my supervisors, Anna Giribono and Simone Di Mitri, for their constant guidance, contribution, and support throughout the development of this thesis.

Giovanni Campri, Trieste, October 2025